Spectral properties of planar helium under periodic driving

Guillermo Javier Madroñero Pabón

Spectral properties of planar helium under periodic driving

Dissertation der Fakultät für Physik
der Ludwig-Maximilians-Universität München

vorgelegt von Guillermo Javier Madroñero Pabón
aus Pasto

München, den 6. April 2004

1. Gutachter: Priv. Doz. Dr. Andreas Buchleitner
2. Gutachter: Prof. Dr. Harald Friedrich
Tag der mündlichen Prüfung: 24 Mai 2004

a Diana, Cecilia y Guillermo

Zusammenfassung

Wir stellen eine originelle Methode zur akkuraten quantenmechanischen Behandlung des planaren Drei-Körper-Coulombproblems in Gegenwart eines elektromagnetischen Feldes vor. Unser *ab initio* Zugang vereint Floquet-Theorie, komplexe Dilatation und die Darstellung des Hamilton-Operators in geeignet gewählten Koordinaten – ohne freie Parameter. Das resultierende, durch eine komplex-symmetrische, dünn besetzte Bandmatrix dargestellte verallgemeinerte Eigenwertproblem vergleichsweise großer Dimension wird mittels fortgeschrittener Methoden paralleler Programmierung gelöst.
In der vorliegenden Dissertation wird dieser theoretisch/numerische Apparat zur vollständigen Charakterisierung des gebundenen sowie des doppelt angeregten Spektrums des feldfreien zweidimensionalen Heliumatoms genutzt. Insbesondere untersuchen wir die *frozen planet*-Konfiguration in planarem Helium. Bei dem durch ein äußeres Feld gestörten Atom konzentrieren wir uns auf die nahresonant getriebene frozen planet-Konfiguration und stellen erste Ergebnisse vor, welche die Existenz nichtdispergierender Wellenpakete nahelegen, die entlang des korrespondierenden klassischen Orbits propagieren. Hierbei handelt es sich um eine hoch nichttriviale Bestätigung früherer Ergebnisse für ein eindimensionales Modellatom, bei freilich merklicher Überhöhung der Zerfallsrate der atomaren Eigenzustände im Feld – aufgrund des zusätzlich verfügbaren, transversalen Zerfallskanals. Letzterer macht sich bereits durch eine Überhöhung der Zerfallsraten des ungestörten frozen planet im Vergleich zum eindimensionalen Modell bemerkbar, in überraschend quantitativer Übereinstimmung mit den Ergebnissen dreidimensionaler Rechnungen.

Abstract

We present an original method for the accurate quantum treatment of the planar three body Coulomb problem under electromagnetic driving. Our *ab initio* approach combines Floquet theory, complex dilation, and the representation of the Hamiltonian in suitably chosen coordinates without adjustable parameters. The resulting complex-symmetric, sparse banded generalized eigenvalue problem of rather high dimension is solved using advanced techniques of parallel programming.

In the present thesis, this theoretical/numerical machinery is employed to provide a complete description of the bound and of the doubly excited spectrum of the field-free 2D helium atom. In particular, we report on frozen planet quantum states in planar helium. For the driven atom, we focus on the near resonantly driven frozen planet configuration, and give evidence for the existence of nondispersive two-electron wave packets which propagate along the associated periodic orbit. This represents a highly nontrivial qualitative confirmation of earlier calculations on a 1D model atom, though with important enhancements of the decay rate of these atomic eigenstates in the field, due to the transverse decay channel. The latter is already found to enhance the decay rates of the unperturbed frozen planet as compared to the 1D model, in surprisingly good quantitative agreement with 3D results.

Resumen

Presentamos un método original para el tratamiento cuántico preciso del problema planar Coulombiano de tres cuerpos bajo la accion de un campo electromagnético. Nuestro acercamiento *ab initio*, sin parámetros ajustables, combina la teoría de Floquet, el método de dilatación compleja y la representación del Hamiltoniano en coordenadas escogidas adecuadamente. El problema generalizado de valores propios resultante en mátrices complejas simétricas con estructura de bandas de grandes dimensiones es resuelto utilizando técnicas avanzadas de programación paralela.

En la presente tesis, esta maquinaria teorética/numérica es utilizada para la descripción completa de los estados acotados y doblemente excitados del átomo bidimensional no perturbado de helio. En particular, reportamos acerca de estados del helio bidimensional denominados *frozen planet states*.

Para el átomo en campos electromagnéticos, nos enfocamos en el caso de frecuencias cuasiresonantes de la configuración del "frozen planet", y encontramos evidencia para la existencia de paquetes de onda no dispersivas de dos electrones que se propagan a lo largo de la órbita periódica asociada. Esto representa una confirmación altamente no trivial de cálculos anteriores en modelos unidimensionales, aunque con aumentos importantes de las ratas de decaimiento de estos estados atómicos propios en el campo, debido a los canales de decaimiento transversales. Lo anterior también explica el aumento de las ratas de decaimiento del "frozen planet" no perturbado comparado con el modelo unidimensional, y está en sorprendentemente buena correspondencia cuantitativa con resultados tridimensionales.

This thesis is not only the product of my own effort, on the contrary many people have contributed directly or indirectly to it. Unfortunately this page is too small to mention everybody and I hope the understanding of those who do not appear here.

I am very grateful to Andreas Buchleitner, who more than the supervisor of this thesis, has been a friend, who encouraged and supported me during the last three years and also enriched my limited knowledge (not only of german) with stimulating discussions.

I thank Dominique Delande, Benoît Grémaud and Laurent Hilico for the possibility to stay some weeks in Paris and for illuminating discussions about many aspects of this thesis.

Also I want to thank Peter Schlagheck, with whom I enjoyed long discussions about the frozen planet, and Andreas Krug, who introduced me in the world of parallel programming.

I gratefully acknowledge the Max-Planck Gesellschaf and the Bayerische Akademie der Wissenschaften for computing time in the supercomputers HITACHI SR8000-F1 and IBM p690.

This work has been done at the Max-Planck-Institute for Physics of Complex Systems in Dresden. I thank all the scientific and non-scientific staff of the institute for creating the perfect environment to work.

I am also grateful to my friends and colleagues that I met in Dresden: Nilüfer Baba, Sandro Wimberger, Thomas Wellens, Florian Mintert, Klaus Hornberger, Cord Müller, Vyacheslav Shatokhin, Nils Hasselmann, Andrey Kolovsky, Alexey Ponomariev, Adriana Sánchez, Anatole Kenfack, Uwe Börner, Andre Ribeiro de Carvalho, Diego Cárdenas, Andzelika Kassan, Bruno Kozinski, and many others. For they created an agreeable atmosphere which made much easier to work and to enjoy life in that beautiful city.

I want to thank two special friends, Carlos Viviescas and Juan Diego Urbina, for their support before and after coming to Germany. Besides, it is always a pleasure to exchange some ideas with them.

Finally, I want to thank my parents Cecilia and Guillermo, and specially Diana for her love and understanding.

Contents

1 Introduction **1**

1.1 Framework and formulation of the problem 1

1.2 Structure of the thesis 3

2 Description of the system **5**

2.1 Hamiltonian 5

2.2 Parabolic coordinate transformations 7

2.3 Unperturbed 2D helium in parabolic coordinates 9

2.3.1 Stationary Schrödinger equation 10

2.3.2 Harmonic oscillators representation 11

2.3.3 Matrix elements and selection rules 13

2.3.4 Symmetries of the 2D helium atom 14

2.3.5 Basis set adapted to P_{12} and L_z 16

2.4 Driven 2D helium atom 18

2.4.1 Floquet theorem 18

2.4.2 Complex rotation method 19

2.4.3 Rotated Floquet operator in parabolic coordinates . . . 24

2.4.4 Basis adapted to P_{12} and Π_x 25

2.4.5 Matrix structure of the generalized Floquet eigenvalue problem 26

2.5 Visualization of the wave functions 28

2.5.1 Wave functions in the field free case 28
2.5.2 Time evolution of the wave functions 31

3 Numerical treatment of the problem 33
3.1 Symbolic calculus 33
3.2 Construction of the basis set 35
3.3 Lanczos algorithm 41
3.4 Numerical implementation 43
3.4.1 Basic notions of parallel programming 44
3.4.2 Storage of the matrices 45
3.4.3 Implementation of the Lanczos algorithm 47
3.4.4 Performance of the code 47
3.5 Applications 49
3.5.1 Ground state of the 2D helium atom 49
3.5.2 Resonant coupling between $|1s1s\rangle$ and $|1s2p\rangle$ 50

4 Spectrum of 2D helium 57

5 The frozen planet configuration 73
5.1 Introduction 73
5.2 Identification of frozen planet states in 2D He 76
5.2.1 Expectation value of $\cos\theta_{12}$ 77
5.2.2 Husimi distributions 78
5.3 Frozen planet states of 2D He 80
5.3.1 Energies and decay rates 80
5.3.2 Wave functions 84

6 Nondispersive wave packets in 2D Helium 95
6.1 The classical helium atom under periodic driving 96
6.2 Husimi distributions 98
6.3 Driven 2D frozen planet states 98

7 Summary and perspectives **107**

7.1 Summary 107

7.2 Outlook 108

A Numerics **111**

A.1 Parabolic transformations 111

A.1.1 Kinetic operator $T = 16 r_1 r_2 r_{12} (\nabla_1^2 + \nabla_2^2)$ 112

A.1.2 The field term in the velocity gauge 113

A.2 Hamiltonian and selection rules 114

B Some simple integrable 2D systems **119**

B.1 Eigenfunctions of the 2D harmonic oscillator 119

B.2 2D hydrogen atom 120

B.2.1 Coordinate representation of tensorial products of Fock states 123

B.2.2 Eigenfunctions of the 2D hydrogen atom 124

B.3 2D helium atom without electron-electron interaction 125

C On some useful identities in Floquet theory **129**

Chapter 1

Introduction

1.1 Framework and formulation of the problem

After hydrogen, helium is the simplest naturally available atomic species. But at the same time, helium is one of the simplest systems where neither the classical nor the quantum dynamics are integrable. Indeed, for this microscopic realization of the three body problem of celestial mechanics (with gravitational forces replaced by attractive/repulsive Coulomb interactions), the two-electron dynamics is in general irregular or chaotic, with only rather small domains of classical phase space occupied by regular, i.e., integrable motion. This loss of integrability, due to the electron-electron interaction, caused the failure of first quantization attempts on the basis of Bohr's quantum postulates [1]. Only with the development of the modern semiclassical theory [2,3] and the subsequent semiclassical quantization of helium [4,5] was the nonintegrability of the quantum system understood as the direct counterpart of the corresponding classical mixed regular-chaotic dynamics [6].

Under the action of an additional electromagnetic field, the complexity of both, the classical and the quantum dynamics, increases dramatically. However, as compared to one electron atoms, helium adds the additional electro-electron interaction term, which also is a source of electronic correlations. Manifestations of interelectronic repulsion in driven helium have been observed in the double ionization of helium from the ground state, by strong laser fields [7,8]: Strong enhancement (by several orders of magnitude) of the doubly charged ion production as compared to the yield expected on the basis of a single active electron approximation [9, 10] – where the electron-electron

interaction is neglected – was observed and interpreted as a fingerprint of correlated electronic ionization processes (manifesting in *non-sequential* ionization, as opposed to *sequential* ionization in the independent electrons picture) where one electron is "knocked out" by the other in a laser-induced recollision process. On the theoretical side, a number of very restrictive nonsequential models [7, 11, 12] can fit many coarse-grained features of the experiment, however none of these models can fully describe the geometry of the fragmentation process observed in more refined experiments [13, 14] – which also suggest a strong dependence of the excitation and ionization process on the electronic structure [15] of He-like atoms.

Whilst electronic correlations are essentially brought about by the kinematics of the double ionization process sketched above, it is also feasible to prepare the atom in a highly correlated initial state. Strong electronic correlations can be found in highly doubly excited states of unperturbed helium. These highly asymmetric though very stable doubly excited states are well localized along the frozen planet configuration [6, 16, 17], characterized by the highly correlated classical dynamics of the electrons. Under near-resonantly periodic driving these states transform into nondispersive wave packets [18] in 1D quantum calculations [19]. However, until now, no evidence of the existence of these objects has been found in realistic quantum calculations in more than one dimension. This is a crucial issue, since on the one hand, classical calculations suggest a nontrivial role of the dimension of the accessible configuration space, and, on the other, nondispersive wave packets of one electron systems appear to open new perspectives of quantum control [20].

In the present thesis we are going to explore the electronic correlations of the field-free atom, as well as of driven helium, and, for the first time, evidence for the existence of two-electron nondipersive wave packets in more than one dimension is given.

A clear understanding of these issues requires an accurate theoretical treatment of driven helium. The latter defines a formidable theoretical and numerical challenge: Even in the simplest case of the field-free 3D helium atom, the rapid increase of the basis size and of the number of nonzero matrix elements as the angular momentum is increased saturates the currently available computing facilities, already at low values of the angular momentum [21–25]. An additional, linearly polarized electromagnetic field will mix almost all good quantum numbers of the field-free case, and only the projection of the total angular momentum onto the polarization axis of the field and a generalized parity which encompasses the phase of the driving field remain conserved. Consequently, the density of states dramatically increases with the excita-

tion of the electrons as well as with the order of the multiphoton excitation process induced by the external field. Therefore, a fully three dimensional treatment of the driven helium problem for arbitrary driving frequencies and electronic excitations still remains beyond reach even of the largest supercomputers currently available, simply due to the rapidly increasing size of Hilbert space as more and more angular momenta are coupled by the field. Note, however, that three dimensional ab initio treatments [26–29] of the ionization of helium from the atomic ground state are available, though cannot resolve the transient population of highly excited states in the course of the ionization process. Neither has it been demonstrated so far that they bear the potential to describe the dynamics of highly excited initial states under electromagnetic driving.

Here we present a novel approach to the driven three body Coulomb problem, restricted to planar configuration with the field polarization axis within the plane. Whilst such confinement certainly restricts the generality of our model, semiclassical scaling arguments suggest that the unperturbed three body dynamics is essentially planar at high electronic excitations and small to moderate total angular momenta (see section 2.1). Equally so, highly correlated fragmentation processes starting from the atomic ground state appear to be mediated by essentially two-dimensional configurations [15, 30]. Beyond the atomic problem to which we will apply our machinery in this thesis, the planar three body Coulomb problem also has realizations in quasi two dimensional semiconductor structures [31–36], as well as in 2D quantum dots [37].

1.2 Structure of the thesis

In **chapter 2**, we provide the theoretical tools to describe our system. For a rigorous regularization of the Coulomb singularities in the 2D three body Coulomb problem we introduce a representation of the Hamiltonian in parabolic coordinates, which leads to a representation in creation and annihilation operators. Analytic expressions for the matrix elements are then easily obtained in an appropriate basis set. To account for the temporal periodicity of the perturbation, we employ Floquet theory. Complex rotation of the Hamiltonian allows to extract energies and decay rates of the resonance poles of the Floquet resolvent. We also describe the visualization of the real energy wave functions, given the eigenvalues and eigenvectors of the rotated Hamiltonian.

In **chapter 3** an outline of the numerical treatment of the system is given: we describe how to obtain the algebraic expressions of the Hamiltonian in creation and annihilation operators, as well as the matrix elements of the Hamiltonian, by symbolic calculus. To minimize the band width of the matrices, the basis set is ordered by a special algorithm also discussed here. We furthermore briefly sketch the diagonalization routine we use, and its implementation on a parallel computer. Finally, we consider two simple examples to illustrate our method.

A complete description of the bound spectrum of 2D helium can be found in **chapter 4**, as well as a description of zero-angular-momentum doubly excited states of the 2D three body Coulomb problem.

In **chapter 5** we study Rydberg series of doubly excited states of 2D helium, which are localized along the frozen planet trajectories.

Chapter 6 discusses first results on nondispersive wave packets which emerge from frozen planet states under periodic, near-resonant driving.

We conclude our work with a short summary, and give a brief outlook of future applications of our approach on the driven three body Coulomb problem. In addition, we include three appendices: in **appendix A**, we outline the technical details of the parabolic transformations employed in chapter 2 and provide the explicit expression of the field-free Hamiltonian in creation and annihilation operators; **appendix B** is devoted to illustrate the most relevant features of simple integrable systems for our present work; in **appendix C**, we prove an important identity of Floquet theory.

Chapter 2

Description of the system

We describe our ab-initio quantum treatment of the two-dimensional helium atom under periodic driving, starting out with the general, field free three body problem with Coulomb interaction. After describing the Hamiltonian of our system, we introduce a new set of parabolic coordinates [38], which induces a representation in terms of the creation and annihilation operators of four harmonic oscillators. The representation is separately considered for the field-free atom case and for the driven atom. In both cases a complete description of the symmetries of the system is given.

2.1 Hamiltonian

Let us consider the three body Coulomb problem. Here, as depicted in figure 2.1, $\boldsymbol{r}_1$ and $\boldsymbol{r}_2$ denote the positions of particles 1 and 2 with respect to particle 3, and $\boldsymbol{p}_1$ and $\boldsymbol{p}_2$ the conjugate momenta. If q_1, q_2 and q_3 are the charges of the particles 1, 2 and 3, respectively, then the Hamiltonian in atomic units (i.e., $\hbar$, $4\pi\varepsilon_0$ and the mass m of the electron are set equal to unity) of the three body Coulomb problem in the center of mass frame reads

$$H_{3\text{ body}} = \frac{\boldsymbol{p}_1^2}{2\mu_{13}} + \frac{\boldsymbol{p}_2^2}{2\mu_{23}} + \frac{\boldsymbol{p}_1 \cdot \boldsymbol{p}_2}{m_3} + \frac{q_1 q_3}{r_1} + \frac{q_2 q_3}{r_2} + \frac{q_1 q_2}{r_{12}}, \tag{2.1}$$

where μ_{13} (resp. μ_{12}) is the reduced mass of particles 1 (resp. 2) and 3, and m_3 is the mass of particle 3. Thus the Hamiltonian of the helium atom in the center of mass frame with a fixed nucleus corresponds to the case where m_3 is infinite, $\mu_{13} = \mu_{23} = 1$, and $q_1 = q_2 = -1$, $q_3 = Z = 2$:

$$H_0 = \frac{\boldsymbol{p}_1^2 + \boldsymbol{p}_2^2}{2} - \frac{Z}{r_1} - \frac{Z}{r_2} + \frac{\gamma}{r_{12}}, \tag{2.2}$$

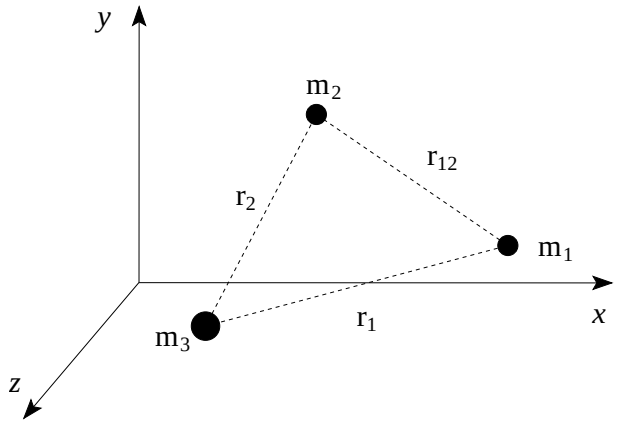

Figure 2.1: The three body Coulomb problem: three charged particles of masses m_1, m_2 and m_3 in three dimensional space interact through Coulomb forces.

with $\gamma = 1$.

In the presence of an external electromagnetic field, the non-relativistic Hamiltonian of the driven atom reads

$$H = \frac{1}{2}(\boldsymbol{p}_1 - \boldsymbol{A}(\boldsymbol{r}_1,t))^2 + \frac{1}{2}(\boldsymbol{p}_2 - \boldsymbol{A}(\boldsymbol{r}_2,t))^2 - \frac{Z}{r_1} - \frac{Z}{r_2} + \frac{\gamma}{r_{12}} + \Phi(\boldsymbol{r}_1,t) + \Phi(\boldsymbol{r}_2,t), \tag{2.3}$$

where $\boldsymbol{A}(\boldsymbol{r},t)$ and $\Phi(\boldsymbol{r},t)$ denote the vector and the scalar potential of the external electromagnetic field, respectively. In the dipole approximation [39] and for a linearly polarized field along the x direction with driving amplitude F and frequency ω the Hamiltonian takes the form

$$\begin{aligned} H &= H_0 + F(x_1 + x_2)\cos(\omega t), \\ H &= H_0 - \frac{F}{i\omega}\left(\frac{\partial}{\partial x_1} + \frac{\partial}{\partial x_2}\right)\sin(\omega t), \end{aligned} \tag{2.4}$$

in position and velocity gauge, respectively.

Both, the classical and the quantum dynamics of driven or unperturbed helium are governed by the Hamiltonian (2.2) and (2.4), respectively. In the classical case, in analogy to the unperturbed hydrogen atom [40] the Hamiltonian (2.2) exhibits general scaling rules [41]: the classical dynamics

generated by (2.2) is invariant under the scaling transformations

$$\begin{array}{lcll} H_0 & \mapsto & |E|^{-1} H_0, & \\ \boldsymbol{r}_i & \mapsto & |E| \boldsymbol{r}_i, & (i=1,2), \\ \boldsymbol{p}_i & \mapsto & |E|^{-1/2} \boldsymbol{p}_i, & (i=1,2), \\ t & \mapsto & |E|^{3/2} t, & \end{array} \tag{2.5}$$

where E is the energy of system. This scale invariance also holds for driven helium, where, additionally, the scaled field amplitude and the scaled frequency are obtained by the transformations

$$\begin{array}{lcl} F & \mapsto & |E|^{-2} F, \\ \omega & \mapsto & |E|^{-3/2} \omega. \end{array} \tag{2.6}$$

From (2.5), the angular momentum scales as $L^{sc} = |E|^{\frac{1}{2}} L$. Therefore, for moderate values of L and highly doubly excited states of helium ($E \simeq 0$), the scaled angular momentum is close to zero, and thus the classical dynamics of the helium atom is almost planar. Precisely this is the semiclassical energy regime where one expects that the classical and quantum dynamics are similar.

From now on, we are going to restrict the problem to two dimensions. Then, the positions of the electrons, in Cartesian coordinates, are (x_1, y_1) and (x_2, y_2), respectively. Thus the field-free helium atom has 4 degrees of freedom, while in the driven case we have the additional time dependent term. The quantum dynamics is governed by the Schrödinger equation of the Hamiltonian (2.2) in one case, and by the Schrödinger equation of (2.4) in the other.

However, one of the main difficulties in solving the Schrödinger equation for the helium atom are the Coulomb singularities in the Hamiltonian (2.2). Nevertheless, choosing an appropriate representation in parabolic coordinates [38], the singularities are rigorously regularized. As we will see in the next section, in these coordinates the interelectronic distance and the distances from the nucleus to the electrons have polynomial expressions in terms of the coordinates, what later allows to express all matrix elements analytically and to define strong selection rules, leading to a banded sparse matrix representation of the corresponding eigenvalue problem.

2.2 Parabolic coordinate transformations

The appropriate set of parabolic coordinates is obtained after three coordinate transformations. We start with the Cartesian coordinates of both

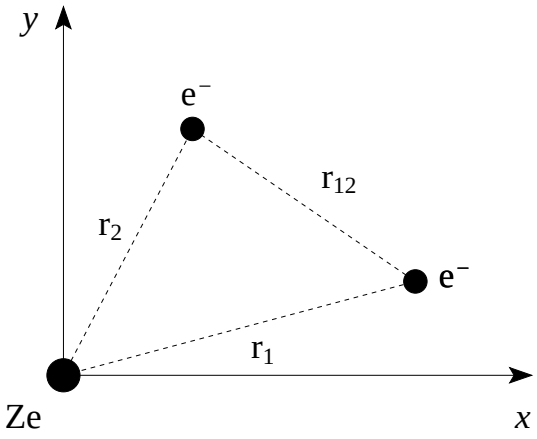

Figure 2.2: Two dimensional helium atom: the nucleus with infinite mass lies in the origin, while both electrons are confined to the xy-plane, at distances r_1 and r_2.

electrons, (x_1, y_1) and (x_2, y_2), respectively. After the first transformation, only r_1 and r_2 are polynomial functions of the new coordinates $\mu_i\,\nu_i$, $i = 1, 2$,

$$\begin{aligned} x_i &= \tfrac{1}{2}(\mu_i^2 - \nu_i^2), & \mu_i &= \sqrt{r_i + x_i}, \\ y_i &= \mu_i \nu_i, & \nu_i &= \sqrt{r_i - x_i}, \\ r_i &= \sqrt{x_i^2 + y_i^2} = \tfrac{1}{2}(\mu_i^2 + \nu_i^2), & &\text{for } i = 1, 2, \end{aligned} \tag{2.7}$$

while r_{12} still involves square root functions of the coordinates (we do not present this latter expression here).

The second transformation consists just in a rotation by 45° of each pair of the new coordinates (μ_1, μ_2) and (ν_1, ν_2):

$$\begin{aligned} \mu_p &= (\mu_1 + \mu_2)/\sqrt{2}, & \mu_1 &= (\mu_p + \mu_m)/\sqrt{2}, \\ \mu_m &= (\mu_1 - \mu_2)/\sqrt{2}, & \mu_2 &= (\mu_p - \mu_m)/\sqrt{2}, \\ \nu_p &= (\nu_1 + \nu_2)/\sqrt{2}, & \nu_1 &= (\nu_p + \nu_m)/\sqrt{2}, \\ \nu_m &= (\nu_1 - \nu_2)/\sqrt{2}, & \nu_2 &= (\nu_p - \nu_m)/\sqrt{2}. \end{aligned} \tag{2.8}$$

Hereafter we have, $r_{12} = \sqrt{(\mu_p^2 + \nu_p^2)(\mu_m^2 + \nu_m^2)}$. Hence, after another parabolic transformation, also r_{12} will be a polynomial function of the coordi-

nates. Our final coordinate set is thus defined as

$$\begin{aligned}
\mu_p &= (x_p^2 - y_p^2)/2, & x_p &= \sqrt{r_p + \mu_p}, \\
\nu_p &= x_p y_p, & y_p &= \sqrt{r_p - \mu_p}, \\
\mu_m &= (x_m^2 - y_m^2)/2, & x_m &= \sqrt{r_m + \mu_m}, \\
\nu_m &= x_m y_m, & y_m &= \sqrt{r_m - \mu_m}, \\
r_p &= \sqrt{\mu_p^2 + \nu_p^2} = x_p^2 + y_p^2, \\
r_m &= \sqrt{\mu_m^2 + \nu_m^2} = x_m^2 + y_m^2,
\end{aligned} \tag{2.9}$$

leading to the following representation of r_1, r_2 and r_{12} in terms of x_p, y_p, x_m and y_m:

$$\begin{aligned}
16r_1 &= ((x_p - y_m)^2 + (x_m + y_p)^2)((x_p + y_m)^2 + (x_m - y_p)^2) \\
16r_2 &= ((x_p - x_m)^2 + (y_p - y_m)^2)((x_p + x_m)^2 + (y_p + y_m)^2) \\
4r_{12} &= (x_p^2 + y_p^2)(x_m^2 + y_m^2).
\end{aligned} \tag{2.10}$$

The Jacobian (i.e., the determinant of the partial derivatives) of each parabolic transformation in eq. (2.7) is $\mu_i^2 + \nu_i^2 = 2r_i$, so the Jacobian of the first transformation is $J_1 = 4r_1 r_2$. The second transformation corresponds to two rotations, hence $J_2 = 1$. The third transformation is again composed of two parabolic transformations, therefore $J_3 = (x_p^2 + y_p^2)(x_m^2 + y_m^2) = 4r_{12}$. It follows for the Jacobian of the complete transformation:

$$B = J_1 J_2 J_3 = 16 r_1 r_2 r_{12}. \tag{2.11}$$

2.3 Unperturbed 2D helium in parabolic coordinates

We now give a complete description of the representation of 2D He in the parabolic representation introduced in section 2.2. We start out with the regularized eigenvalue equation generated by the Hamiltonian (2.2) followed by its polynomial representation in the algebra of the creation and annihilation operators of four harmonic oscillators. In the basis defined by the tensor product of the Fock states of these harmonic oscillators all matrix elements have analytical expressions. Though, due to the arbitrary choice of the sign of the square root in (2.7) and in (2.9), this basis produces both physical and non-physical solutions. A study of the symmetries of 2D He allows to define a symmetrized basis set which extracts precisely the physical solutions.

2.3.1 Stationary Schrödinger equation

The stationary Schrödinger equation $H_0|\psi\rangle = E|\psi\rangle$ of the 2D helium atom is regularized by multiplication with the Jacobian (2.11). The eigenvalue equation then takes the form of a generalized eigenvalue problem (GEVP):

$$\left(-\frac{1}{2}T + V\right)|\psi\rangle = EB|\psi\rangle, \tag{2.12}$$

where the kinetic and potential operators, T and V, are given by

$$\begin{aligned} T &= 16r_1r_2r_{12}(\nabla_1^2 + \nabla_2^2), \\ V &= -16Zr_2r_{12} - 16Zr_1r_{12} + 16\gamma r_1r_2. \end{aligned} \tag{2.13}$$

The explicit expression for the potential term V in terms of parabolic coordinates follows upon substituting of (2.10). The expression for the kinetic term T is a bit more complicated, and is explicitly derivate in appendix A.1. There we obtain

$$\begin{aligned} T &= (r_1 + r_2)\left\{(x_p^2 + y_p^2)\left(\frac{\partial^2}{\partial x_m^2} + \frac{\partial^2}{\partial y_m^2}\right) + (x_m^2 + y_m^2)\left(\frac{\partial^2}{\partial x_p^2} + \frac{\partial^2}{\partial y_p^2}\right)\right\} + \\ &\quad 2(r_2 - r_1)\left\{(x_mx_p + y_my_p)\left(\frac{\partial^2}{\partial x_m\partial x_p} + \frac{\partial^2}{\partial y_m\partial y_p}\right) + \right. \\ &\quad \left.(y_mx_p - x_my_p)\left(\frac{\partial^2}{\partial x_m\partial y_p} - \frac{\partial^2}{\partial y_m\partial x_p}\right)\right\}. \end{aligned} \tag{2.14}$$

Thus, T and V are polynomial functions of 8th degree in the parabolic coordinates $x_p,\ y_p,\ x_m,\ y_m$ and in their partial derivatives ∂_{x_p}, ∂_{y_p}, ∂_{x_m}, ∂_{y_m}. The Jacobian B given in (2.11) has a polynomial expression of degree 12.

Angular momentum

The angular momentum L_z – a particularly important quantity in our further treatment – has a particularly simple polynomial expression in terms of our new parabolic coordinates. Also note that it preserves its original differential form but for a prefactor:

$$\begin{aligned} L_z &= -i\left(x_1\frac{\partial}{\partial y_1} - y_1\frac{\partial}{\partial x_1} + x_2\frac{\partial}{\partial y_2} - y_2\frac{\partial}{\partial x_2}\right) \\ &= -\frac{i}{4}\left(x_p\frac{\partial}{\partial y_p} - y_p\frac{\partial}{\partial x_p} + x_m\frac{\partial}{\partial y_m} - y_m\frac{\partial}{\partial x_m}\right). \end{aligned} \tag{2.15}$$

2.3.2 Harmonic oscillators representation

Given that all terms in (2.13–2.15) are of second order in the coordinates and/or partial derivatives, it is suggestive to introduce creation and annihilation operators defined by the different possible combinations of x_i and p_i, according to

$$\begin{array}{rclcrcl} a_{x_p} &=& (x_p + ip_{x_p})/\sqrt{2}, & & a^\dagger_{x_p} &=& (x_p - ip_{x_p})/\sqrt{2}, \\ a_{x_m} &=& (x_m + ip_{x_m})/\sqrt{2}, & & a^\dagger_{x_m} &=& (x_m - ip_{x_m})/\sqrt{2}, \\ a_{y_p} &=& (y_p + ip_{y_p})/\sqrt{2}, & & a^\dagger_{y_p} &=& (y_p - ip_{y_p})/\sqrt{2}, \\ a_{y_m} &=& (y_m + ip_{y_m})/\sqrt{2}, & & a^\dagger_{y_m} &=& (y_m - ip_{y_m})/\sqrt{2}. \end{array} \tag{2.16}$$

In particular, the expression of the angular momentum in terms of these operators follows from (2.15):

$$L_z = \frac{i}{4}(a_{x_p}a^\dagger_{y_p} - a^\dagger_{x_p}a_{y_p} + a_{x_m}a^\dagger_{y_m} - a^\dagger_{x_m}a_{y_m}). \tag{2.17}$$

This expression can be simplified if we introduce the right and left circular operators in the planes (x_p, y_p) and (x_m, y_m), defined by

$$\begin{aligned} a_1 &= (a_{x_p} - ia_{y_p})/\sqrt{2}, \\ a_2 &= (a_{x_p} + ia_{y_p})/\sqrt{2}, \\ a_3 &= (a_{x_m} - ia_{y_m})/\sqrt{2}, \\ a_4 &= (a_{x_m} + ia_{y_m})/\sqrt{2}. \end{aligned} \tag{2.18}$$

In that case, the angular momentum reads

$$L_z = \frac{1}{4}(a^\dagger_1 a_1 - a^\dagger_2 a_2 + a^\dagger_3 a_3 - a^\dagger_4 a_4) = \frac{1}{4}(N_1 - N_2 + N_3 - N_4), \tag{2.19}$$

where $N_i = a^\dagger_i a_i$. Furthermore, we have checked that also the expression of the GEVP (2.12) in terms of circular operators is dramatically simplified as compared to the corresponding expressions in terms of the operators defined by (2.16).

The circular operators satisfy the usual commutation relations:

$$[a_i, a_j] = 0, \qquad [a^\dagger_i, a^\dagger_j] = 0, \qquad [a_i, a^\dagger_j] = \delta_{ij}, \tag{2.20}$$

for $i, j = 1, 2, 3, 4$. Thus, we can associate a harmonic oscillator with each pair of circular operators $a^\dagger_i$ and a_i, what induces a natural basis set of tensorial products of harmonic oscillator Fock states:

$$|n_1 n_2 n_3 n_4\rangle = |n_1\rangle \otimes |n_2\rangle \otimes |n_3\rangle \otimes |n_4\rangle. \tag{2.21}$$

Therefore the action of the circular operators on a single Fock state is given by

$$\begin{aligned} a_i^\dagger|n_i\rangle &= \sqrt{n_i+1}|n_i+1\rangle, \\ a_i|n_i\rangle &= \sqrt{n_i}|n_i-1\rangle. \end{aligned} \tag{2.22}$$

The corresponding number operators $N_i = a_i^\dagger a_i$, with $N_i|n_i\rangle = n_i|n_i\rangle$, $n_i = 0, 1, 2, \ldots$, are related to the number operators of the creation and annihilation operators (2.16) by (s. appendix B.2, eq. (B.19))

$$N_1 + N_2 = N_{x_p} + N_{y_p}, \quad \text{and} \quad N_3 + N_4 = N_{x_m} + N_{y_m}. \tag{2.23}$$

In order to express our original Hamiltonian H_0 in terms of the creation and annihilation operators we still need expressions for x_p , y_p, x_m, y_m and the associated derivatives in terms of a_i, $a_i^\dagger$. From (2.16) and (2.18) it follows that:

$$\begin{aligned} x_p &= \frac{1}{2}(a_1 + a_2 + a_1^\dagger + a_2^\dagger), & \frac{\partial}{\partial x_p} &= \frac{1}{2}(a_1 + a_2 - a_1^\dagger - a_2^\dagger), \\ y_p &= \frac{i}{2}(a_1 - a_2 - a_1^\dagger + a_2^\dagger), & \frac{\partial}{\partial y_p} &= \frac{i}{2}(a_1 - a_2 + a_1^\dagger - a_2^\dagger), \\ x_m &= \frac{1}{2}(a_3 + a_4 + a_3^\dagger + a_4^\dagger), & \frac{\partial}{\partial x_m} &= \frac{1}{2}(a_3 + a_4 - a_3^\dagger - a_4^\dagger), \\ y_m &= \frac{i}{2}(a_3 - a_4 - a_3^\dagger + a_4^\dagger), & \frac{\partial}{\partial y_m} &= \frac{i}{2}(a_3 - a_4 + a_3^\dagger - a_4^\dagger). \end{aligned} \tag{2.24}$$

Since all terms in the GEVP (2.12) are polynomial functions of the parabolic coordinates and of their derivatives, the same remains true for the expressions of T, V and B in terms of the circular operators a_i, $a_i^\dagger$. Thus, H_0 becomes a purely polynomial expression of finite degree of the creation and annihilation operators of four harmonic oscillators, and (2.12) has an efficient analytical representation in the basis set (2.21).

However, as we have seen in section 2.3.1, the GEVP (2.12) is polynomial of 12th degree in x_p , y_p, x_m, y_m, and in their derivatives, and equally so in a_i, $a_i^\dagger$, because of (2.24). Therefore, to derive the analytic expression of the GEVP in terms of creation and annihilation operators, it was necessary to use symbolic calculus. We wrote a Mathematica program (see section 3.1) which is able to calculate operator products in normal order (creation operators on the left [42]). The normally ordered expressions for T, V and B have 335, 357 and 1463 monomial terms of the form

$$M = a_1^{\dagger\alpha_1} a_2^{\dagger\alpha_2} a_3^{\dagger\alpha_3} a_4^{\dagger\alpha_4} a_1^{\beta_1} a_2^{\beta_2} a_3^{\beta_3} a_4^{\beta_4}, \tag{2.25}$$

respectively, where α_i and β_i are integer numbers.

For example, the first couple of terms of the kinetic and potential operators $-T/2+V$, for $Z=\gamma=1$ a.u., read

$$-\frac{1}{2}T+V=-2-5a_1a_2+\frac{3}{8}a_1^2a_2^2-4a_1^\dagger a_1+\frac{1}{16}a_1^4a_2^4-5a_3a_4-\frac{39}{2}a_1a_2a_3a_4+\frac{1}{8}a_1^2a_2^2a_3^2a_4^2+\frac{1}{2}a_3^3a_4^3-\frac{5}{8}a_1a_2a_3^3a_4^3+\frac{1}{16}a_3^4a_4^4+\frac{1}{2}a_1^3a_2^3+\frac{5}{4}a_1^\dagger a_1^2a_2-\frac{35}{2}a_1^\dagger a_1a_3a_4-\frac{39}{4}a_1^\dagger a_1^2a_2a_3a_4-\frac{7}{4}a_1^\dagger a_1^3a_2^2a_3a_4-\frac{33}{8}a_1^\dagger a_1a_3^2a_4^2+\cdots \tag{2.26}$$

The full expressions are listed in appendix A.2.

2.3.3 Matrix elements and selection rules

From (2.22) we note that

$$a_i^{\dagger p}a_i^q|n\rangle=\sqrt{n(n-1)\dots(n-q+1)}\times\times\sqrt{(n-q+1)(n-q+2)\dots(n-q+p)}|n-q+p\rangle. \tag{2.27}$$

Hence, the matrix elements $\langle n_1n_2n_3n_4|M|n_1'n_2'n_3'n_4'\rangle\neq 0$ of a single monomial term (2.25) have analytic expressions that only involve square roots of integer numbers. Therefore, the matrix elements of the GEVP (2.12) are sums of such expressions. Since the number of monomials in the GEVP is finite, each basis state is coupled to a finite number of states of the basis. Whether two states are coupled or not is determined by a *selection rule* defined by each monomial term in the following way: Two elements $|n_1n_2n_3n_4\rangle$ and $|n_1'n_2'n_3'n_4'\rangle$ of the basis set (2.21) are coupled or satisfy the selection rule $\{\Delta n_1,\Delta n_2,\Delta n_3,\Delta n_4\}$, with $\Delta n_i=n_i-n_i'$, if $\langle n_1n_2n_3n_4|M|n_1'n_2'n_3'n_4'\rangle\neq 0$. For example, the selection rules defined by the first, second and third terms of (2.26) are $\{0,0,0,0\}$, $\{-1,-1,0,0\}$, and $\{-2,-2,0,0\}$, respectively. Two different monomial terms can define the same selection rule (e.g., the selection rule of the fourth term of (2.26) is also $\{0,0,0,0\}$), thus the number of selection rules is smaller than the number of terms in the GEVP. Indeed, the Jacobian B has 155 selection rules, while the kinetic and potential operators $-\frac{1}{2}T+V$ have 91, and in total there are 159 different selection rules (see appendix A.2). All selection rules for (2.12) satisfy $-4\leq\Delta n_i\leq 4$ ($i=1,2,3,4$) and $\Delta n_1-\Delta n_2+\Delta n_3-\Delta n_4=0$. The last property is just the selection rule for the angular momentum $\Delta L_z=0$, since L_z commutes with the Hamiltonian and $4L_z=N_1-N_2+N_3-N_4$ (eq. (2.19)).

Now, for a given selection rule $\Delta\alpha = \{\Delta n_1, \Delta n_2, \Delta n_3, \Delta n_4\}$, the matrix elements $\langle\alpha + \Delta\alpha| - \frac{1}{2}T + V|\alpha\rangle$ and $\langle\alpha + \Delta\alpha|B|\alpha\rangle$, with $|\alpha\rangle = |n_1 n_2 n_3 n_4\rangle$ and $|\alpha + \Delta\alpha\rangle = |n_1 + \Delta n_1\ n_2 + \Delta n_2\ n_3 + \Delta n_3\ n_4 + \Delta n_4\ \rangle$, depend only on $n_1,\ n_2,\ n_3$ and n_4. Here we show only one matrix element of the operator $-\frac{1}{2}T + V$ for the selection rule $\Delta\alpha = \{-2, -2, 0, 0\}$:

$$\begin{aligned}\langle\alpha + \Delta\alpha| - \frac{1}{2}T + V|\alpha\rangle \;&=\; \frac{1}{8}\sqrt{n_1(n_1-1)n_2(n_2-1)}\,\times \\ &\quad\times\Big(\gamma(8 + 3n_1^2 - 7n_2 + 3n_2^2 + n_1(8n_2 - 7)) \\ &\quad -(n_1 + n_2 - 1)(n_3 + n_4 + 1)(12Z - 1)\Big).\end{aligned} \tag{2.28}$$

This and all matrix elements of the GEVP (2.12) have been calculated with the help of symbolic calculus, as well as the respective Fortran 90 subroutines for the posterior diagonalization (see section 3.1).

2.3.4 Symmetries of the 2D helium atom

The symmetries of the 2D helium atom are the rotational invariance around an axis perpendicular to the plane, the exchange symmetry P_{12} between both electrons, and the parity Π. In 2 dimensions, the latter coincides with a rotation of 180° around z, thus it is related to the angular momentum L_z by $\Pi = e^{-i\pi L_z} = (-1)^{L_z}$. Additionally, the 2D helium atom is also invariant under reflections with respect to the x and y axes, which we denote Π_x and Π_y, respectively. These two commuting symmetries satisfy $\Pi_x\Pi_y = \Pi_y\Pi_x = \Pi$ and commute with parity. However, they do not commute with angular momentum, since

$$\Pi_x L_z = -L_z\Pi_x, \tag{2.29}$$

but they do commute with L_z^2. The group generated by Π_x, Π_y and P_{12} is the so called D_{2h} point group [43, 44]. It is an invariant group of the Hamiltonian (2.2). Hence, we have two alternatives to label the eigenstates of the 2D helium atom. We can use the eigenvalues $l = 0, \pm1, \pm2, \ldots$ of angular momentum L_z and the exchange symmetry $P_{12} = \textit{odd}$ or $\textit{even}$, in which case the spectra corresponding to l and $-l$ are identical, as a consequence of the time reversal invariance of the problem [45]. Or the eigenstates can be labeled by the absolute value $|l|$ of the angular momentum, the exchange symmetry P_{12}, and the symmetry $\Pi_x = \pm1$. This second possibility is more convenient for the case when the atom is exposed to an electromagnetic field polarized along the x direction (s. section 2.4.4).

The action of Π_x and P_{12} on a vector (x_p, y_p, x_m, y_m) in parabolic coordinates is calculated straightforwardly from the transformations (2.7), (2.8) and (2.9):

$$\begin{aligned} \Pi_x : (x_p, y_p, x_m, y_m) &\longmapsto (x_p, -y_p, x_m, -y_m), \\ P_{12} : (x_p, y_p, x_m, y_m) &\longmapsto (x_p, y_p, y_m, -x_m). \end{aligned} \tag{2.30}$$

Hence, for example, the action of Π_x on a_1 (s. eq. (2.18)) is $\Pi_x : a_1 = (a_{x_p} - ia_{y_p})/\sqrt{2} \mapsto (a_{x_p} + ia_{y_p})/\sqrt{2} = a_2$. In the same way, we find that

$$\begin{aligned} \Pi_x : (a_1, a_2, a_3, a_4) &\longmapsto (a_2, a_1, a_4, a_3), \\ P_{12} : (a_1, a_2, a_3, a_4) &\longmapsto (a_1, a_2, ia_3, -ia_4), \end{aligned} \tag{2.31}$$

or, equivalently, the action on number operators,

$$\begin{aligned} \Pi_x : (N_1, N_2, N_3, N_4) &\longmapsto (N_2, N_1, N_4, N_3), \\ P_{12} : (N_1, N_2, N_3, N_4) &\longmapsto (N_1, N_2, N_3, N_4). \end{aligned} \tag{2.32}$$

Therefore $\Pi_x^2 = P_{12}^2 = 1$, and thus

$$\begin{aligned} \Pi_x |n_1 n_2 n_3 n_4\rangle &= \pm |n_2 n_1 n_4 n_3\rangle, \\ P_{12} |n_1 n_2 n_3 n_4\rangle &= \pm |n_1 n_2 n_3 n_4\rangle. \end{aligned} \tag{2.33}$$

Unphysical symmetries

The parabolic transformation induces nonphysical symmetries due to the fact that a single parabolic transformation $(x, y) \to (\mu, \nu)$ is a double mapping of the Cartesian plane into the plane of parabolic coordinates as illustrated in figure 2.3. As described in the appendix B.2, for a single parabolic transformation the Hamiltonian of the 2D hydrogen atom is invariant under the transformation $(\mu, \nu) \mapsto (-\mu, -\nu)$. Therefore, parity with respect to (μ, ν) is a new discrete symmetry introduced by the coordinate transformation, and the physical wave function must satisfy $\psi(\mu, \nu) = \psi(-\mu, -\nu)$.

In our case we have two parabolic transformations in (2.7), and two more in (2.9), and each of them induces an unphysical symmetry which leaves the Hamiltonian invariant. These symmetries are

$$\begin{aligned} \Pi_1 : (\mu_1, \nu_1) &\longmapsto (-\mu_1, -\nu_1), \\ \Pi_2 : (\mu_2, \nu_2) &\longmapsto (-\mu_2, -\nu_2), \\ \Pi_p : (x_p, y_p) &\longmapsto (-x_p, -y_p), \\ \Pi_m : (x_m, y_m) &\longmapsto (-x_m, -y_m). \end{aligned} \tag{2.34}$$

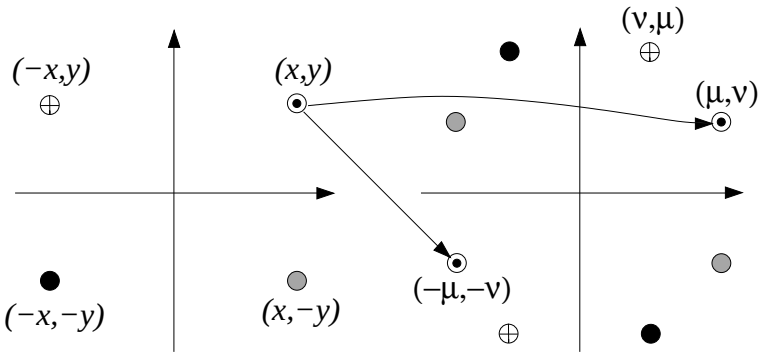

Figure 2.3: Double mapping under a single parabolic transformation.

The effects of them on the vector (x_p, y_p, x_m, y_m) are

$$\begin{aligned}
\Pi_1 : (x_p, y_p, x_m, y_m) &\longmapsto (-y_m, x_m, -y_p, x_p), \\
\Pi_2 : (x_p, y_p, x_m, y_m) &\longmapsto (x_m, y_m, x_p, y_p), \\
\Pi_p : (x_p, y_p, x_m, y_m) &\longmapsto (-x_p, -y_p, x_m, y_m), \\
\Pi_m : (x_p, y_p, x_m, y_m) &\longmapsto (x_p, y_p, -x_m, -y_m).
\end{aligned} \tag{2.35}$$

The wave function $\psi(x_p, y_p, x_m, y_m)$ must be singlevalued in the space of Cartesian coordinates (x_1, y_1, x_2, y_2), hence it must be invariant under any of the transformations Π_1, Π_2, Π_p and Π_m. Therefore the wave function must belong to an irreducible representation of the invariance group G of the GEVP (2.12), generated by Π_x, Π_y, P_{12}, Π_1, Π_2, Π_p and Π_m, for which the characters of the unphysical symmetries are equal to the dimension of the representation [46, 47]. As shown by Hilico et al. [38], such representations are one dimensional and the characters of the classes generated by Π_x, Π_y and P_{12} precisely coincide with the character table of the group D_{2h} [43, 44]. Hence the physical eigenfunctions $\psi(x_p, y_p, x_m, y_m)$ can be distinguished by their symmetry properties with respect to Π_x, Π_y and P_{12} alone.

2.3.5 Basis set adapted to P_{12} and L_z

Let us assume that the eigenfunctions expanded in the basis (2.21), i.e.,

$$|\psi\rangle = \sum_{n_1,n_2,n_3,n_4} c_{n_1,n_2,n_3,n_4} |n_1 n_2 n_3 n_4\rangle, \tag{2.36}$$

are also eigenfunctions of P_{12} and L_z^2. Since $|\psi\rangle$ must be invariant under the parity transformations Π_p and Π_m acting individually on the parabolic

coordinates (x_p, y_p) and (x_m, y_m), respectively, then from (2.23) and, as explained in the appendix B.2, from the even character of the eigenfunctions of the harmonic oscillator, both $n_1 + n_2$ and $n_3 + n_4$ must be even. In addition, since the eigenvalues l of the angular momentum and the quantum numbers n_i are related by $4l = n_1 - n_2 + n_3 - n_4$, $n_1 - n_2 \equiv n_3 - n_4 \equiv c \bmod 4$, with $c = 0$ or 2.

As we can see from (2.30), the parity P_{12} corresponds to a rotation of $\pi/2$ in the plane (x_m, y_m), thus $P_{12} = \exp(-i\pi L_{z_m}/2)$, where $L_{z_m} = x_m p_{y_m} - y_m p_{x_m} = N_3 - N_4$ (see eq. (B.21) in appendix B.2). Hence, $P_{12}|n_1n_2n_3n_4\rangle = \exp(-i\pi(n_3 - n_4)/2)|n_1n_2n_3n_4\rangle$. Since $n_3 - n_4 \equiv c \bmod 4$, with $c = 0$ or 2, the states $|n_1n_2n_3n_4\rangle$ with $c = 0$ ($c = 2$) are symmetric (antisymmetric) with respect to the exchange operator, i.e., singlet (triplet) states.

From (2.33) we see that the permutation S_{2143} (i.e. the permutation of the indices of the circular operators such that $(1, 2, 3, 4) \mapsto (2, 1, 4, 3)$) corresponds to the symmetry Π_x, and the identity permutation S_{1234} corresponds to the exchange symmetry, and therefore both of them commute with the Hamiltonian of the 2D helium atom. Furthermore, there are two more permutations, namely S_{3412} and S_{4321}, which leave the representation of (2.12) in circular operators invariant, as can be checked using symbolic calculus. The permutation S_{3412} corresponds to the transformation $(x_p, y_p, x_m, y_m) \mapsto (x_m, y_m, x_p, y_p)$. However, due to the double representation in parabolic coordinates, the last transformation leaves the Cartesian coordinates (x_1, y_1, x_2, y_2) invariant. Hence, S_{3412} is the identity in the space of Cartesian coordinates. Therefore, the second permutation S_{4321} is also equivalent to Π_x, due to the fact that $S_{4321} = S_{3412}S_{2143}$. Since $S_{3412}|n_1n_2n_3n_4\rangle = |n_3n_4n_1n_2\rangle$ (i.e., the action of S_{3412} on the basis $|n_1n_2n_3n_4\rangle$ is not the identity), the basis (2.21) does not only extract the physical solutions of the GEVP. Therefore, the elements of the basis must be symmetrized according to

$$|n_1n_2n_3n_4\rangle^+ = |n_1n_2n_3n_4\rangle + |n_3n_4n_1n_2\rangle. \tag{2.37}$$

In that case, $S_{3412}|n_1n_2n_3n_4\rangle^+ = |n_1n_2n_3n_4\rangle^+$.

Finally, since $|n_1n_2n_3n_4\rangle^+$ is also an eigenstate of the angular momentum L_z with eigenvalue $l = (n_1 - n_2 + n_3 - n_4)/4$, where $n_1 - n_2 + n_3 - n_4 = 4l$, and $n_1 - n_2 \equiv n_3 - n_4 \equiv c \bmod 4$, this basis set extracts only physical solutions of the GEVP with angular momentum l, corresponding to singlet ($c = 0$) or triplet ($c = 2$) states.

2.4 Driven 2D helium atom

2.4.1 Floquet theorem

The Hamiltonian of the driven 2D helium atom (2.4) has a periodic time dependence, with period $T = 2\pi/\omega$. Therefore, the Floquet theorem [48] guarantees that the solutions $|\psi(t)\rangle = |\psi(\boldsymbol{r}_1, \boldsymbol{r}_2, t)\rangle$ of the Schrödinger equation

$$H(\boldsymbol{r}_1, \boldsymbol{r}_2, t)|\psi(t)\rangle = i\frac{\partial}{\partial t}|\psi(\boldsymbol{r}_1, \boldsymbol{r}_2, t)\rangle, \quad \text{with } H(t+T) = H(t), \tag{2.38}$$

can be expressed as superpositions of time periodic wave functions $|\phi_{\varepsilon_i}(t)\rangle = |\phi_{\varepsilon_i}(\boldsymbol{r}_1, \boldsymbol{r}_2, t)\rangle$ [49],

$$|\psi(t)\rangle = \sum_i c_i \exp\left(-i\varepsilon_i t\right)|\phi_{\varepsilon_i}(t)\rangle, \tag{2.39}$$

with $|\phi_{\varepsilon_i}(t+T)\rangle = |\phi_{\varepsilon_i}(t)\rangle$. Here, the ε_i and $|\phi_i(t)\rangle$ are called *quasienergies* and *Floquet states*, and are the eigenvalues and eigenvectors of the Floquet Operator $\mathcal{H}_F = H(t) - i\hbar\partial/\partial t$ [49, 50], i.e.

$$\mathcal{H}_F|\phi_{\varepsilon_i}(t)\rangle = \varepsilon_i|\phi_{\varepsilon_i}(t)\rangle. \tag{2.40}$$

This operator is a hermitian operator that acts on the extended Hilbert space of square integrable, time periodic functions, $\mathcal{L}^2(\mathbb{R}^4) \otimes \mathcal{L}^2(T)$. In this space, the Floquet states form a complete orthogonal basis.

For a given $k \in \mathbb{Z}$, and for any Floquet state $|\phi_{\varepsilon_i}(t)\rangle$, the state $e^{ik\omega t}|\phi_{\varepsilon_i}(t)\rangle$ is also a Floquet state with quasienergy $\varepsilon_i + k\omega$. Then the states $|\psi_{\varepsilon_i}(t)\rangle = e^{-i\varepsilon_i t}|\phi_{\varepsilon_i}(t)\rangle$ and $|\psi_{\varepsilon_i+k\omega}(t)\rangle = e^{-i(\varepsilon_i+k\omega)t}|\phi_{\varepsilon_i+k\omega}(t)\rangle$ represent the same physical eigenstate of (2.38) [51, 52]. Therefore, the spectrum of the Floquet operator is invariant under translations by ω, i.e., periodic on the energy axis, and we can restrict our spectral analysis to the quasienergies within an interval of length ω, called a *Floquet zone* – in analogy to the Brillouin zone familiar from the theory of solids with spatially periodic potentials [53]. Accordingly, the Floquet states of our present example play the role of Bloch waves in the solid state.

Since the Floquet states are periodically time-dependent, they can be expanded in a Fourier series:

$$|\phi_{\varepsilon_i}(t)\rangle = \sum_{k=-\infty}^{\infty} e^{-ik\omega t}|\phi_{\varepsilon_i}^k\rangle. \tag{2.41}$$

The Fourier components $|\phi^k_{\varepsilon_i}\rangle$ of the Floquet states are not orthogonal in $\mathcal{L}^2(\mathbb{R}^4)$. However, as shown in appendix C, within a given Floquet zone they satisfy the identity

$$\sum_k \langle \phi^{k+\Delta k}_{\varepsilon_i} | \phi^k_{\varepsilon_j} \rangle = \delta_{ij}\delta_{\Delta k,0}. \tag{2.42}$$

From here stronger completeness and orthogonality conditions for the Floquet states are found: for any time t, the Floquet states form a complete basis set of orthogonal states (see appendix C):

$$\begin{aligned} \langle \phi_{\varepsilon_i}(t) | \phi_{\varepsilon_j}(t) \rangle &= \delta_{ij}, \\ \sum_i |\phi_{\varepsilon_i}(t)\rangle\langle\phi_{\varepsilon_i}(t)| &= 1, \quad \forall t. \end{aligned} \tag{2.43}$$

When substituted in the Floquet eigenvalue problem (2.40), the Fourier expansion (2.41) leads to the eigenvalue problem

$$(\varepsilon_i - H_0 + k\omega)\,|\phi^k_{\varepsilon_i}\rangle = \frac{F}{2}(x_1+x_2)\left(|\phi^{k+1}_{\varepsilon_i}\rangle + |\phi^{k-1}_{\varepsilon_i}\rangle\right), \quad k \in \mathbb{Z}, \tag{2.44}$$

$$(\varepsilon_i - H_0 + k\omega)\,|\phi^k_{\varepsilon_i}\rangle = \frac{F}{2\omega}\left(\frac{\partial}{\partial x_1} + \frac{\partial}{\partial x_2}\right)\left(|\phi^{k+1}_{\varepsilon_i}\rangle - |\phi^{k-1}_{\varepsilon_i}\rangle\right), \quad k \in \mathbb{Z}, \tag{2.45}$$

in the position and in velocity gauge, respectively.

Whilst time dependence has been eliminated in (2.44) and (2.45), there appears a new quantum number k. It can be shown [49,54] that, in the limit of large average photon number, there is a one-to-one correspondence between the quasienergy spectrum of the Floquet Hamiltonian and the spectrum of an atom dressed by a monochromatic coherent state of the quantized radiation field. In this semiclassical limit (referring to the mean energy of the driving field coherent state), the quantum number k counts the number of photons exchanged between the atom and the field, with respect to the expectation value of the photon number operator for the driving field coherent state.

2.4.2 Complex rotation method

In analogy to the spectrum of 3D helium [6], the spectrum of 2D helium consists of Rydberg series of states converging to single ionization thresholds (s. chapter 4). Therefore, even in the simplest case of the unperturbed atom, there are resonant or autoionizing states with finite life time embedded in the continuum of lower series. Now, an additional electromagnetic field

will couple these autoionizing states of the field-free atom and thus strongly modify the resonance structure of the system. This strongly enhances the effective density of states, due to the periodicity of the Floquet spectrum. Indeed, in this case, as can be seen from eq. (2.44) or (2.45), the external field induces a coupling of all states dressed with k photons to states dressed with $k-1$ and $k+1$ photons. Consequently, also all bound states are coupled with the continuum of the atom.

To extract the resonance states and their decay rates we use complex rotation. This method is based on the analytic continuation of the resolvent operator or Green's function into the complex plane. The applicability of the complex rotation method for the Coulomb potential is proven in [55], and for the Floquet operator in [56], while its mathematical foundations are outlined in [57–59]. These are far from being trivial and it is not the purpose of the present manuscript to reproduce them here – we only summarize the central results.

For a time-independent Hamiltonian H (alike H_0 in eq. (2.2), or the Floquet operator $\mathcal{H}_F$, eq. (2.40)), the Green's function is defined by

$$G(E) = \frac{1}{E - H}, \tag{2.46}$$

for $E \in \mathbb{C}$ [60]. Hence, each discrete state of H corresponds to a pole of the Green's function, while the continuum states induce a branch cut along the real axis. Therefore, there are two analytic continuations of the Green's function in the complex plane, approaching the real axis from the upper or from the lower half plane, respectively:

$$G^{\pm}(E) = \frac{1}{E \pm i\epsilon - H}, \quad \text{with } \epsilon \to 0^{+}. \tag{2.47}$$

The energies of the resonant states and their decay rates are given in terms of the complex poles E_i of $G^{+}(E)$, by $\mathrm{Re}(E_i)$ and $-2\mathrm{Im}(E_i)$, respectively. To separate them from the continuum, we do not use explicitly the Green's function. According to the complex rotation method, the poles of the resolvent are isolated eigenvalues of a complex Hamiltonian, called *rotated Hamiltonian*, which is derived from the original Hamiltonian H by

$$H(\theta) = R(\theta) H R(-\theta), \tag{2.48}$$

where θ is a positive real number, no greater than $\pi/4$, and

$$R(\theta) = \exp\left(-\theta \frac{\boldsymbol{r}\cdot\boldsymbol{p} + \boldsymbol{p}\cdot\boldsymbol{r}}{2}\right) \tag{2.49}$$

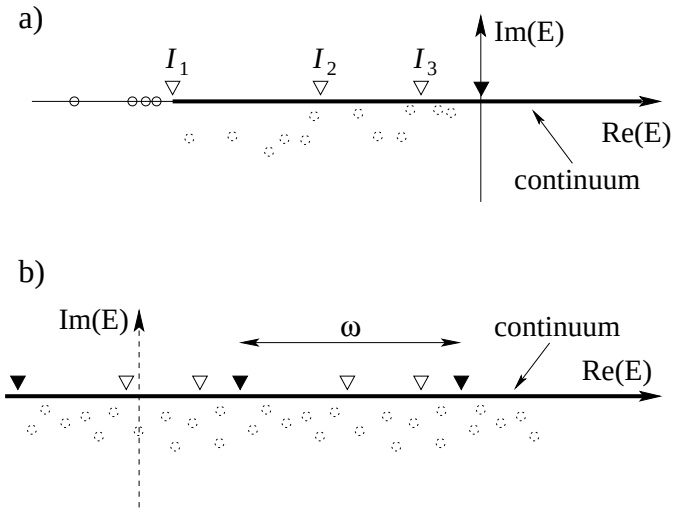

Figure 2.4: Poles of the resolvent operator of the unperturbed Hamiltonian of 2D helium (a) and of the Floquet operator (b). The bound states in (a) are located on the real axis, while the resonance energies on the second Riemann sheet (dotted circles in (a) and (b)) have negative imaginary parts and need to be uncovered by analytic continuation of the corresponding resolvent operator. The triangles indicate the single ($\triangledown$) and double ($\blacktriangledown$) ionization thresholds of the 2D helium atom, in (a), and the multiphoton ionization thresholds $I_N + k\omega$, $k \in \mathbb{Z}$ ($\triangledown$) and $k\omega$ ($\blacktriangledown$) of the Floquet operator, in (b), connected to a branch cut along the real energy axis (bold black lines), which is due to the continuum states.

is the complex rotation operator. It is a hermitian operator with inverse $R(-\theta)$.

Under the action of $R(\theta)$, coordinates and momenta transform like

$$\begin{aligned} R(\theta)\boldsymbol{r}R(-\theta) &= \boldsymbol{r}e^{i\theta}, \\ R(\theta)\boldsymbol{p}R(-\theta) &= \boldsymbol{p}e^{-i\theta}. \end{aligned} \tag{2.50}$$

Hence, the rotated Hamiltonian is obtained after substituting $\boldsymbol{r} \to \boldsymbol{r}e^{i\theta}$ and $\boldsymbol{p} \to \boldsymbol{p}e^{i\theta}$. $H(\theta)$ is no more hermitian, but complex symmetric, and its spectrum is complex and depends on θ. However, the spectrum of $H(\theta)$ has the following important properties:

(i) The bound spectrum of H is invariant under the complex rotation.

(ii) The continuum states are located on half lines, rotated by an angle -2θ around the ionization thresholds of H into the lower half of the complex plane. In the specific case of the unperturbed 2D helium Hamiltonian (2.2), in analogy to the 3D case [61], the continuum states are rotated around the single ionization thresholds I_N given by eq. (4.1). In the case of the Floquet operator, they are rotated around the multiphoton ionization thresholds $I_N + k\omega$ (k integer).

(iii) The resonance poles of $G^+(E)$ correspond to θ-*independent* complex eigenvalues of $H(\theta)$ provided θ has been chosen large enough to uncover their position on the second Riemann sheet. The associated resonance eigenfunctions are square integrable [59], in contrast to the resonance eigenfunctions of the unrotated Hamiltonian. The latter are asymptotically diverging outgoing waves [45, 62].

The set of eigenvectors $|E_{i\theta}\rangle$ of $H(\theta)$ forms a complete basis of Hilbert space, but it is not orthogonal with respect to the usual hermitian scalar product, due to the non-hermiticity of $H(\theta)$. One rather has [63]

$$\begin{aligned} \langle\overline{E_{i\theta}}|E_{j\theta}\rangle &= \delta_{ij} \\ \sum_i |E_{i\theta}\rangle\langle\overline{E_{i\theta}}| &= 1, \end{aligned} \tag{2.51}$$

where $\langle\overline{E_{i\theta}}|$ denotes the complex conjugate of $\langle E_{i\theta}|$ (i.e., $\langle\overline{E_{i\theta}}|$ is the transpose of $\langle E_{i\theta}|$ rather than its adjoint) and the sum is taken over all states including the continua (which, in any numerical diagonalization on a finite basis set, are composed of discrete continuum states).

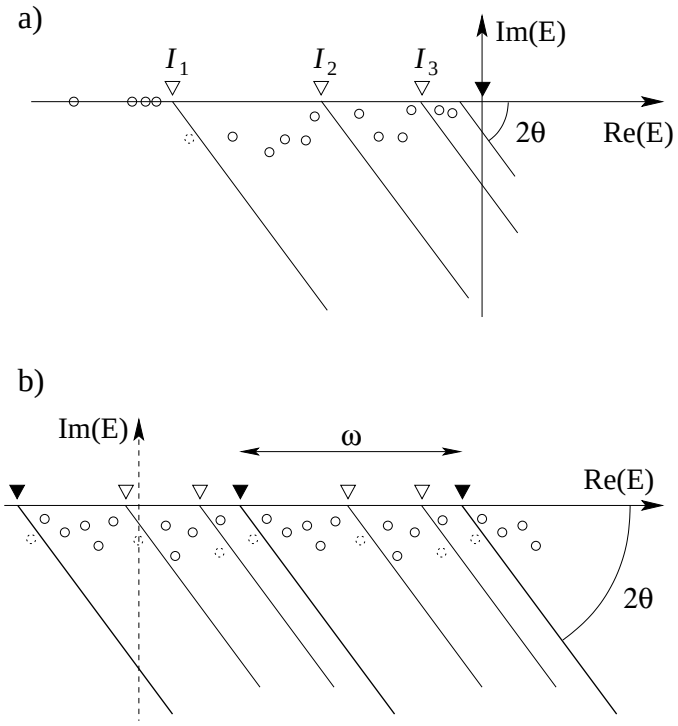

Figure 2.5: Spectrum of (a) the complex rotated Hamiltonian of the unperturbed 2D helium atom, and of (b) the complex rotated Floquet operator. The continua in both cases are rotated by an angle 2θ, around the ionization thresholds I_N in (a), and around the multiphoton ionization thresholds $I_N + k\omega$ ($k \in \mathbb{Z}$) in (b). The continuous circles denote the exposed resonances. The dotted circles indicate the resonances that do not appear, but can be uncovered by further increasing the value of θ.

In the sequel of this thesis, we will be interested in the probability density of states of both the unperturbed 2D helium atom and of the Floquet operator of the corresponding driven system. For the unperturbed case, we need the projection operator $|E\rangle\langle E|$ on a real energy state $|E\rangle$ in terms of the eigenstates of the rotated Hamiltonian, given by [64–66]

$$|E\rangle\langle E| = \frac{1}{2\pi i}\sum_i \left\{ \frac{R(-\theta)|E_{i\theta}\rangle\langle\overline{E_{i\theta}}|R(\theta)}{E_{i\theta} - E} - \frac{R(-\theta)|\overline{E_{i\theta}}\rangle\langle E_{i\theta}|R(\theta)}{\overline{E_{i\theta}} - E} \right\}. \quad (2.52)$$

In the case of the Floquet operator, we use the time evolution operator $U(t_1, t_2)$, expressed as a function of the Fourier coefficients $|\phi^{k_2}_{\varepsilon_j,\theta}\rangle$ of the

rotated Floquet states and of the quasienergies ε_j [65, 66],

$$U(t_2,t_1)=\sum_{j,k_1,k_2} e^{-i\varepsilon_j(t_2-t_1)}e^{ik_1\omega t_1}e^{-ik_2\omega t_2}R(-\theta)|\phi^{k_2}_{\varepsilon_j,\theta}\rangle\overline{\langle\phi^{k_1}_{\varepsilon_j,\theta}|}R(\theta). \tag{2.53}$$

2.4.3 Rotated Floquet operator in parabolic coordinates

Together with the rotation of the configuration space by an angle θ we also introduce a dilation by a positive real number α_c, such that the (Cartesian) coordinates and the momenta transform according to $\boldsymbol{r}\to\alpha_c\boldsymbol{r}e^{i\theta}$ and $\boldsymbol{p}\to\boldsymbol{p}e^{-i\theta}/\alpha_c$. Since the dilation by a factor α_c is a unitary transformation described by the unitary operator [67]

$$D_{\alpha_c}=\exp\left(i(\log\alpha_c)\frac{\boldsymbol{r}\cdot\boldsymbol{p}+\boldsymbol{p}\cdot\boldsymbol{r}}{2}\right), \tag{2.54}$$

the spectra of a Hamiltonian H and of the dilated Hamiltonian $H_{\alpha_c}=D_{\alpha_c}HD^\dagger_{\alpha_c}$ are the same. However, when the basis is truncated, the spectrum depends on the parameter α_c if the basis set is not large enough. Therefore α_c can be used as a variational parameter that has to be optimized. Additionally, we note that a dilation by α_c in Cartesian coordinates is equivalent to a dilation by α_c^4 in parabolic coordinates, since the Cartesian coordinates are homogeneous polynomials of 4th degree in the parabolic coordinates (s. eq. (A.6)). In the sequel of the present thesis we always refer to the dilation parameter of the parabolic coordinates $\alpha=\alpha_c^4$.

In parabolic coordinates, the eigenvalue problems (2.44) or (2.45) is regularized by multiplication with the Jacobian (2.11). Thus, the regularized rotated Floquet eigenvalue problem reads

$$\left(\varepsilon_i B+\frac{e^{-2i\theta}}{2\alpha^8}T-\frac{e^{-i\theta}}{\alpha^4}V+k\omega B\right)|\phi^k_{\varepsilon_i}\rangle=\mathcal{F}_\alpha(\theta)\left(|\phi^{k+1}_{\varepsilon_i}\rangle+\eta|\phi^{k-1}_{\varepsilon_i}\rangle\right), \tag{2.55}$$

where B, T and V are given by (2.11) and (2.13), $\eta=\pm1$ in the position and velocity gauge, respectively, and

$$\mathcal{F}_\alpha(\theta)=\begin{cases}\dfrac{1}{2}F\alpha^4e^{i\theta}(x_1+x_2)B, & \text{in the position gauge,}\\[2ex] \dfrac{Fe^{-i\theta}}{2\omega\alpha^4}B\left(\dfrac{\partial}{\partial x_1}+\dfrac{\partial}{\partial x_2}\right), & \text{in the velocity gauge.}\end{cases} \tag{2.56}$$

	$-\frac{1}{2}T+V$	B	GEVP	$\mathcal{F}_\alpha(\theta)$		$\mathcal{H}_F$	
				pos. gauge	vel. gauge	pos. gauge	vel. gauge
SR	91	155	159	488	164	647	323
NT	423	1463	1511	5472	1056	6983	2567

Table 2.1: Number of selection rules (SR) and of normally ordered monomial terms (NT) for the operators that define the GEVPs (2.12) and (2.55) for the unperturbed 2D helium atom (2.2) and for the Floquet problem (2.40).

As shown in appendix A.1, in parabolic coordinates both $(x_1 + x_2)B$ and $B(\partial_{x_1} + \partial_{x_2})$ are polynomial functions of the coordinates and of their derivatives. Therefore, following the reasoning of section 2.3.2, the field operator $\mathcal{F}_\alpha(\theta)$ in position or in velocity gauge can be expressed as a polynomial of the circular operators (2.18). Indeed, the polynomial expression for $(x_1 + x_2)B$, obtained with symbolic calculus, has degree 16 and 5472 normally ordered monomial terms. Additionally, it defines 488 selection rules $\{\Delta n_1, \Delta n_2, \Delta n_3, \Delta n_4\}$. In the velocity gauge, the corresponding expression has 10th degree and 1056 normally ordered monomials, and defines 164 selection rules. Consequently, there are 647 and 323 selection rules $\{\Delta n_1, \Delta n_2, \Delta n_3, \Delta n_4\}$ for the Floquet operator in the position and in the velocity gauge, respectively (s. table 2.4.3).

In addition to the selection rules for the atomic quantum numbers n_i, there are also selection rules for the angular momentum and for the photon quantum number k. For unperturbed 2D helium, angular momentum is a conserved quantity, $\Delta l = 0$, though under the action of an electromagnetic field a state of angular momentum l is coupled to states of angular momentum $l-1$ or $l+1$, i.e. $\Delta l = \pm 1$. Therefore, with (2.19), each selection rule $\{\Delta n_1, \Delta n_2, \Delta n_3, \Delta n_4\}$ satisfies either $\Delta n_1 - \Delta n_2 + \Delta n_3 - \Delta n_4 = \pm 4$ or $\Delta n_1 - \Delta n_2 + \Delta n_3 - \Delta n_4 = 0$. From (2.55) we see that the operators T, V and B (which are also operators of the unperturbed eigenvalue problem) do not couple states of different k value – only the field operator $\mathcal{F}_\alpha(\theta)$ couples states where k differs by ± 1. Therefore, the selection rules for k are again $\Delta k = 0, \ \pm 1$. Furthermore, $\Delta k + \Delta l$ can equal 0, 2, or -2, thus $k + l \bmod 2$ is a conserved quantity.

2.4.4 Basis adapted to P_{12} and Π_x

The driven 2D helium atom is no more invariant under rotations around a perpendicular axis z, and its Hamiltonian (2.4) is not invariant under parity

Π symmetry. Therefore, the only remaining symmetries are the exchange symmetry P_{12}, and the symmetry Π_x with respect to the x axis – provided the field is polarized along this direction. Additionally, the representation in parabolic coordinates introduces nonphysical symmetries already described in section 2.3.4. Since the basis elements (2.37) are not eigenstates of Π_x, this basis is not well adapted to solve the problem under periodic driving. Nevertheless, from (2.33) it follows that basis elements defined by

$$|n_1 n_2 n_3 n_4\rangle^{+\epsilon_x} = |n_1 n_2 n_3 n_4\rangle^{+} + \epsilon_x |n_2 n_1 n_4 n_3\rangle^{+}, \tag{2.57}$$

where $\epsilon_x = \pm 1$, are eigenstates of Π_x with the eigenvalue ϵ_x.

As described in section 2.4.1, there is an additional quantum number k introduced by the Floquet formalism. Thus, the basis set adapted to solve the GEVP (2.55) is given by the states

$$|n_1 n_2 n_3 n_4 k\rangle^{+\epsilon_x} = |n_1 n_2 n_3 n_4\rangle^{+\epsilon_x} \otimes |k\rangle, \tag{2.58}$$

with $n_1 - n_2 \equiv n_3 - n_4 \equiv 0 \bmod 4$ for singlet states and $n_1 - n_2 \equiv n_3 - n_4 \equiv 2 \bmod 4$ for triplet states (see our discussion at the end of section 2.3.5).

Due to the external driving, angular momentum L_z is no more a conserved quantity. However, as we have seen in the previous section, $(k + l) \bmod 2$ is conserved. Therefore, the basis (2.58) can be decomposed into odd and even subspaces with respect to the generalized parity $\Pi_{kl} = (-1)^{k+l}$.

To conclude this section, let us remark that the basis (2.57) can also be used to represent the unperturbed 2D helium atom. In that case, for given values of P_{12}, Π_x and $L_z^2 = l^2$, the eigenfunctions $|\psi_E\rangle$ corresponding to a given energy are superpositions of eigenfunctions with $L_z = l$ and $L_z = -l$, by virtue of (2.57) and (2.19).

2.4.5 Matrix structure of the generalized Floquet eigenvalue problem

If we set $\mathcal{H}_\alpha^{(k)}(\theta) = -Te^{-2i\theta}/2\alpha^8 + Ve^{-i\theta}/\alpha^4 - k\omega B$, the matrix representation of (2.55) in the basis (2.58) can be written as a GEVP

$$\mathcal{A}\mathcal{X}_i = \varepsilon_i \mathcal{B}\mathcal{X}_i, \tag{2.59}$$

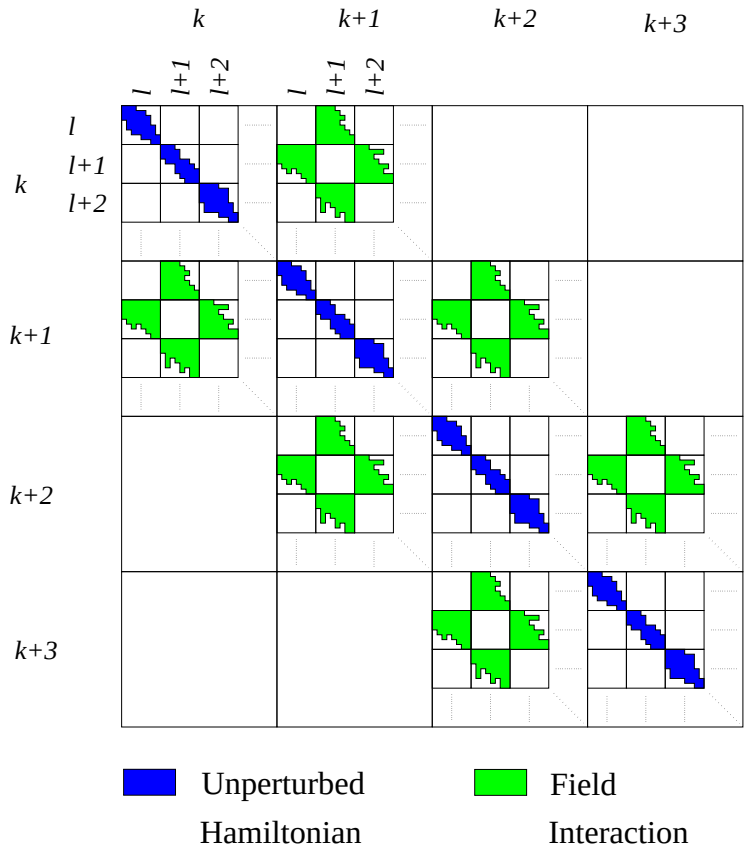

Figure 2.6: General form of the complex symmetric matrix $\mathcal{A}$ of the GEVP (2.59). The diagonal blocks ($\Delta k = 0$) represent $\mathcal{H}_\alpha^{(k)}(\theta)$, while the blocks with $\Delta k = \pm 1$ correspond to $\eta\mathcal{F}_\alpha(\theta)$. For $\mathcal{H}_\alpha^{(k)}(\theta)$, $\Delta l = 0$, and for $\mathcal{F}_\alpha(\theta)$, $\Delta l = \pm 1$. The internal structure of the subblocks is determined by the selection rules in $n_1,\ n_2,\ n_3,\ n_4$, and by the ordering of the basis.

where $\mathcal{A}$ and $\mathcal{B}$ are the infinite block matrices

$$\begin{pmatrix} \ddots & \vdots & \vdots & \vdots & \\ \dots & \mathcal{H}_\alpha^{(k-1)}(\theta) & \eta\mathcal{F}_\alpha(\theta) & 0 & \dots \\ \dots & \mathcal{F}_\alpha(\theta) & \mathcal{H}_\alpha^{(k)}(\theta) & \eta\mathcal{F}_\alpha(\theta) & \dots \\ \dots & 0 & \mathcal{F}_\alpha(\theta) & \mathcal{H}_\alpha^{(k+1)}(\theta) & \dots \\ & \vdots & \vdots & \vdots & \ddots \end{pmatrix} \quad \text{and} \quad \begin{pmatrix} \ddots & \vdots & \vdots & \vdots & \\ \dots & B & 0 & 0 & \dots \\ \dots & 0 & B & 0 & \dots \\ \dots & 0 & 0 & B & \dots \\ & \vdots & \vdots & \vdots & \ddots \end{pmatrix}, \tag{2.60}$$

and $\mathcal{X}_i$ is the column vector which represents $|\phi_{\varepsilon_i}^k\rangle$, with $k \in \mathbb{Z}$.

Since T, V and B are Hermitian operators, the matrices $\mathcal{H}_\alpha^{(k)}(\theta)$ are complex

symmetric. In the position gauge, the representation of $\mathcal{F}_\alpha(\theta)$ is also complex symmetric, but in the velocity gauge its representation is complex antisymmetric. In any case from (2.56) $\mathcal{F}_\alpha(\theta)^T = \eta\mathcal{F}_\alpha(\theta)$. Hence, the matrices $\mathcal{A}$ and $\mathcal{B}$ of GEVP (2.59) are complex symmetric.

Since $\mathcal{H}_\alpha^{(k)}(\theta)$ is the representation of the unperturbed Hamiltonian (2.2) (shifted by multiples of the Jacobian (2.11)), its elements corresponding to different values of the angular momentum are not coupled ($\Delta l = 0$). On the other hand, for the field matrices only elements with $\Delta l = \pm 1$ are coupled. Hence, both $\mathcal{H}_\alpha^{(k)}(\theta)$ and $\mathcal{F}_\alpha(\theta)$ are block matrices. In each block only a few terms are nonzero due to the selection rules in $n_1,\ n_2,\ n_3,\ n_4$. Therefore, $\mathcal{A}$ and $\mathcal{B}$ are sparse banded matrices, with their general form depicted in figure 2.6.

2.5 Visualization of the wave functions

The diagonalization of the rotated Hamiltonian not only provides the resonance spectrum (energies and decay rates), but also allows to calculate physical quantities like probability densities [63], cross sections [64, 68, 69], ionization probabilities [65, 66, 70], etc. Along this work many properties of the eigenstates of 2D helium or of its dynamics under periodic driving will be illustrated in configuration space through the associated electronic density. In the present section, we therefore describe the necessary technical details for the representation of the electronic wave functions and of their time evolution once the eigenvectors of the complex rotated Hamiltonian are obtained.

2.5.1 Wave functions in the field free case

Given the projector (2.52) on the energy state $|E\rangle$, the electronic probability density in configuration space reads

$$\begin{aligned} |\Psi_E(\boldsymbol{r})|^2 &= \langle \boldsymbol{r}|E\rangle\langle E|\boldsymbol{r}\rangle \\ &= \frac{1}{\pi}\mathrm{Im}\sum_j \frac{\langle \boldsymbol{r}|R(-\theta)|E_{j\theta}\rangle\langle\overline{E_{j\theta}}|R(\theta)|\boldsymbol{r}\rangle}{E_{j\theta}-E} \\ &= \frac{1}{\pi}\mathrm{Im}\sum_j \frac{\langle \boldsymbol{r}|R(-\theta)|E_{j\theta}\rangle^2}{E_{j\theta}-E}. \end{aligned} \tag{2.61}$$

A well isolated resonance $|E_{j\theta}\rangle$ with $E_{j\theta} \approx E$ and $|E_{j\theta} - E_{i\theta}| \gg |E_{j\theta} - E|$, $\forall i \neq j$, gives the dominant contribution to the above sum, and one can use the *single pole approximation*

$$|\Psi_E(\boldsymbol{r})|^2 \approx \frac{1}{\pi|\mathrm{Im}\, E_{j\theta}|}\mathrm{Re}\,\langle \boldsymbol{r}|R(-\theta)|E_{j\theta}\rangle^2, \tag{2.62}$$

which we will use in our subsequent visualizations of atomic eigenstates.

In order to calculate the wave functions using the representation described in section 2.4.4, it is necessary to express $\langle \boldsymbol{r}|R(-\theta)|E_{j\theta}\rangle$ in terms of the basis set (2.57):

$$\langle \boldsymbol{r}|R(-\theta)|E_{j\theta}\rangle = \sum_{\substack{n_1,\,n_2\\ n_3,\,n_4}} \langle \boldsymbol{r}|n_1n_2n_3n_4\rangle^{+\epsilon_x\ +\epsilon_x}\langle n_1n_2n_3n_4|R(-\theta)|E_{j\theta}\rangle. \tag{2.63}$$

Therefore, we need an expression for the basis states $|n_1n_2n_3n_4\rangle^{+\epsilon_x}$ in the coordinate representation, together with a matrix representation of the operator $R(-\theta)$. In both cases, it is sufficient to restrict to the product states $|n_1n_2n_3n_4\rangle$, by virtue of (2.37) and (2.57).

- **Product state $\langle \boldsymbol{r}|n_1n_2n_3n_4\rangle$:**

  The circular operators given by (2.18) are independently defined for the pairs (x_p, y_p) and (x_m, y_m) of parabolic coordinates, and $\langle \boldsymbol{r}|n_1n_2n_3n_4\rangle$, if written in parabolic coordinates, can therefore be expressed as a product of two functions depending on (x_p, y_p) and (x_m, y_m), respectively, i.e.

  $$\langle \boldsymbol{r}|n_1n_2n_3n_4\rangle = \langle x_p, y_p|n_1n_2\rangle\langle x_m, y_m|n_3n_4\rangle. \tag{2.64}$$

  Now let us note that $|n_1n_2\rangle$ are simultaneous eigenstates of $N_1 - N_2$ and $N_1 + N_2$, and therefore of a 2D harmonic oscillator, as shown in appendix B.2. Additionally, from eq. (2.16) and (B.14) in appendix B.2, the frequency of the corresponding harmonic oscillator is 1. Thus, if r_p and ϕ_p are the polar transformation of the coordinates (x_p, y_p), and $\psi_{n_1n_2}(r_p, \phi_p) = \langle r_p, \phi_p|n_1n_2\rangle$, from eq. (B.27) it follows that

  $$\begin{cases} \psi_{n_1n_2}(r_p, \phi_p) = \sqrt{\dfrac{1}{\pi}}\sqrt{\dfrac{n_p!}{(n_p + |m_p|)!}}\, e^{im_p\phi_p}\, r_p^{|m_p|}\, e^{-r_p^2/2}\, L_{n_p}^{(|m_p|)}(r_p^2), \\ n_p = \min\{n_1, n_2\}, \\ m_p = n_1 - n_2. \end{cases} \tag{2.65}$$

By analogy, the expression for $\psi_{n_3n_4}(r_m, \phi_m) = \langle r_m, \phi_m | n_3 n_4 \rangle$ has precisely the same form.

In particular, we note that the coordinate representation of $|n_1 n_2 n_3 n_4\rangle$ contains the factor $e^{-(r_p^2+r_m^2)/2} = e^{-(x_p^2+y_p^2+x_m^2+y_m^2)/2}$, and therefore, from (2.10), the wave function decays roughly as $e^{-\sqrt{r_1+r_2}}$.

- **Matrix elements of $R(-\theta)$:**

  The general complex rotation operator acting on a d dimensional configuration space $\mathbb{R}^d$ is a particular case of the complex dilation operator

$$D_\beta = \exp\left(i\beta \frac{\boldsymbol{r}\cdot\boldsymbol{p} + \boldsymbol{p}\cdot\boldsymbol{r}}{2} \right), \tag{2.66}$$

  for any complex number β, and $\boldsymbol{r} \in \mathbb{R}^d$ (thus, unifying eqs. (2.49) and (2.54)). The action of this operator on a wave function $\psi(\boldsymbol{r})$, $\boldsymbol{r} \in \mathbb{R}^d$, is defined by [67]

$$D_\beta \psi(\boldsymbol{r}) = e^{d\beta/2} \psi(\boldsymbol{r} e^{\beta}). \tag{2.67}$$

  In our particular case we can express the complex rotation operator $R(-\theta)$ as a product of two rotation operators $R_p(-\theta)$ and $R_m(-\theta)$, acting on the spaces (x_p, y_p) and (x_m, y_m), respectively, and thus, as before:

$$\langle n_1 n_2 n_3 n_4 | R(-\theta) | n_1' n_2' n_3' n_4' \rangle = \langle n_1 n_2 | R_p(-\theta) | n_1' n_2' \rangle \langle n_3 n_4 | R_m(-\theta) | n_3' n_4' \rangle. \tag{2.68}$$

  If restricted to two dimensions, the matrix elements of D_β in the representation given by the product states $|n_1 n_2\rangle$ read [67]

$$\begin{aligned} &\langle n_1 n_2 | D_\beta | n_1' n_2' \rangle = \\ &\quad \frac{(-1)^{n_p}}{\Gamma(|m_p|+1)} \sqrt{\frac{\Gamma(n_p + |m_p| + 1)\Gamma(n_p' + |m_p| + 1)}{\Gamma(n_p+1)\Gamma(n_p'+1)}} \, (\operatorname{sh}\beta)^{n_p + n_p'} \\ &\quad (\operatorname{ch}\beta)^{-(n_p + n_p' + |m_p| + 1)} \, F\left(-n_p, -n_p', |m_p|+1; -\frac{1}{\operatorname{sh}^2\beta} \right) \delta_{m_p m_p'}, \end{aligned} \tag{2.69}$$

  where $n_p = \min\{n_1, n_2\}$, $m_p = n_1 - n_2$, $n_p' = \min\{n_1', n_2'\}$, $m_p' = n_1' - n_2'$, and $F(a, b, c; x)$ the hypergeometric function [71] (which here reduces to a polynomial).

For purely imaginary $\beta = i\theta$, (2.69) can be simplified to give

$$\langle n_1 n_2|R_p(-\theta)|n_1' n_2'\rangle = (-1)^{n_p'}\sqrt{\binom{n_p+|m_p|}{n_p}\binom{n_p'+|m_p|}{n_p'}}\, i^{n_p+n_p'}\,(\sin\theta)^{n_p+n_p'}$$
$$(\cos\theta)^{-(n_p+n_p'+|m_p|+1)}\,F\left(-n_p,-n_p',|m_p|+1;-\tfrac{1}{\sin^2\theta}\right)\delta_{m_p m_p'}. \tag{2.70}$$

Analogously we obtain the expression for the matrix elements of $R_m(-\theta)$, with formally identical result.

If we write $\beta = i\theta + \log\alpha$, for arbitrary dilation parameters α and rotation angles θ, we find a generalized version of (2.63):

$$\begin{aligned}\langle \boldsymbol{r}|D_\beta^{-1}|E_{j\theta}\rangle &= \langle \boldsymbol{r}|D_{\log\alpha}^{-1}R(-\theta)|E_{j\theta}\rangle \\ &= \frac{1}{\alpha^2}\sum_{\substack{n_1,\,n_2\\ n_3,\,n_4}}\langle \boldsymbol{r}/\alpha|n_1 n_2 n_3 n_4\rangle^{+\epsilon_x\ +\epsilon_x}\langle n_1 n_2 n_3 n_4|R(-\theta)|E_{j\theta}\rangle,\end{aligned} \tag{2.71}$$

what provides the configuration space representation of wave functions $|E_{j\theta}\rangle$ given in complex scaled coordinates $(\alpha_c \boldsymbol{r}e^{i\theta}, \boldsymbol{p}e^{-i\theta}/\alpha_c)$.

2.5.2 Time evolution of the wave functions

In the driven case, we are interested in the electronic density of the time evolution of the resonance eigenstates. This implies the single pole approximation for isolated resonances already discussed above [63], i.e. the temporal dynamics of the electronic density at real energy $E = E_p$ is essentially given by the time evolution of a Floquet eigenstate $|E_{p\theta}\rangle$ under the action of the time evolution operator (2.53), with the single pole approximation $|E_{p\theta}\rangle =: R(\theta)|E_p\rangle$. The Fourier expansion of $|E_{p\theta}\rangle$ at $t = 0$ reads

$$|E_{p\theta}\rangle = \sum_k |\phi_{p\theta}^k\rangle. \tag{2.72}$$

Therefore, at any time t,

$$\phi_p(\boldsymbol{r},t) = \sum_{j,k_1,k_2,k} e^{-i\varepsilon_{j\theta}t}e^{-ik_2\omega t}\langle \boldsymbol{r}|R(-\theta)|\phi_{\varepsilon_j,\theta}^{k_2}\rangle\langle\overline{\phi_{\varepsilon_j,\theta}^{k_1}}|\phi_{p\theta}^k\rangle. \tag{2.73}$$

Using the orthogonality relation (2.42) for the Fourier components of the Floquet states we obtain

$$|\psi_p(\boldsymbol{r},t)|^2 = e^{2(\mathrm{Im}\,\varepsilon_{p,\theta})t}\mathrm{Re}\sum_{k,k'} e^{-i(k-k')\omega t}\langle \boldsymbol{r}|R(-\theta)|\phi^k_{\varepsilon_j,\theta}\rangle\langle \boldsymbol{r}|R(-\theta)|\phi^{k'}_{\varepsilon_j,\theta}\rangle, \tag{2.74}$$

as a generalization of (2.62) up to normalization. Here, the product $\langle \boldsymbol{r}|R(-\theta)|\phi^{k'}_{\varepsilon_j,\theta}\rangle$ is equivalent to the expression (2.63), and can be calculated in precisely the same way as described in the previous section.

Chapter 3

Numerical treatment of the problem

3.1 Symbolic calculus

As already noticed in chapter 2, we use the symbolic language Mathematica to find the analytic expressions for the Hamiltonian operators, in terms of circular operators (2.18), together with the associated selection rules. In Mathematica we represent the annihilation operators a_i by the arrays $\{1, i\}$, the creation operators $a_i^\dagger$ by $\{1, i+4\}$, for $i = 1, 2, 3, 4$, and the identity operator by $\{1, 0\}$. In this way, if M is a monomial term of the form $cd_1d_2 \ldots d_n$, where c is a complex number and each of the operators d_j, with $j = 1, 2, \ldots, n$, is a creation or annihilation operator with array representation $\{1, i_j\}$, then M can be represented by the array $\{c, i_1, i_2, \ldots, i_n\}$ denoted by $\{M\}$. For example, the array representation of $2\pi a_2^2 a_1^\dagger a_4$ is $\{2\pi, 2, 2, 5, 4\}$.

The sum of two monomial arrays $\{M_1\}$ and $\{M_2\}$ is defined by the set $\{\{M_1\}, \{M_2\}\}$. Then a polynomial is represented by the set of the respective monomial arrays: if $P = M_1 + M_2 + \cdots + M_k$ is the sum of the monomials M_1, $M_2, \ldots,$ M_k then the array representation $\{P\}$ of P is $\{\{M_1\}, \{M_2\}, \ldots, \{M_k\}\}$. For instance, the parabolic coordinates and their partial derivatives are polynomial functions of the circular operators, and therefore they can be represented in the form described above. Here we show as an example the representation of x_p, which follows from (2.24):

$$\{x_p\} = \left\{\left\{\tfrac{1}{2}, 1\right\}, \left\{\tfrac{1}{2}, 2\right\}, \left\{\tfrac{1}{2}, 5\right\}, \left\{\tfrac{1}{2}, 6\right\}\right\}. \tag{3.1}$$

The product of two monomial arrays $\{M_1\} = \{c^{(1)}, i_1^{(1)}, i_2^{(1)}, \ldots, i_n^{(1)}\}$ and

$\{M_2\} = \{c^{(2)}, i_1^{(2)}, i_2^{(2)}, \ldots, i_k^{(2)}\}$ is defined in a natural way by

$$\{M_1\} \cdot \{M_2\} = \{c^{(1)}c^{(2)}, i_1^{(1)}, i_2^{(1)}, \ldots, i_n^{(1)}, i_1^{(2)}, i_2^{(2)}, \ldots, i_k^{(2)}\}. \tag{3.2}$$

Thus, using distributivity of the sum, this can be extended for the product with a polynomial:

$$\{M_1\} \cdot \{\{M_2\}, \{M_3\}\} = \{\{M_1\} \cdot \{M_2\}, \{M_1\} \cdot \{M_3\}\}. \tag{3.3}$$

The commutation relations (2.20) of the circular operators in array representation read

$$\begin{array}{rcl} \{1, i, i+4\} & = & \{1, i+4, i\} + \{1, 0\}, \quad \text{for } i = 1, 2, 3, 4, \\ \{1, i, j\} & = & \{1, j, i\}, \quad \text{for } |i-j| \neq 4. \end{array} \tag{3.4}$$

Hence, normal ordering of a monomial $M = \{\cdots, j, j+4, k, \ldots\}$ (and, consequently, of a polynomial) is done step by step taking into account that

$$\{\ldots, i, j, j+4, k, \ldots\} = \{\{\ldots, i, j+4, j, k, \ldots\}, \{\ldots, j, k, \ldots\}\}. \tag{3.5}$$

It turns out that this algebra in the array representation is easily implemented using basic Mathematica functions like `Insert, Delete, Join` etc. Then, using the array representation of the parabolic coordinates and their derivatives and the commutation relations of the creation and annihilation operators, the normally ordered expressions of the eigenvalue problem in parabolic coordinates are calculated. The selection rules defined by a given polynomial are now straightforwardly found: a normally ordered monomial has the form

$$\{c, \underbrace{8, \ldots, 8}_{n_4 \text{ times}}, \underbrace{4, \ldots, 4}_{n_4' \text{ times}}, \underbrace{7, \ldots, 7}_{n_3 \text{ times}}, \underbrace{3, \ldots, 3}_{n_3' \text{ times}}, \ldots\}, \tag{3.6}$$

from which the corresponding selection rule is $\{\Delta n_1, \Delta n_2, \Delta n_3, \Delta n_4\}$ with $\Delta n_i = n_i - n_i'$.

The matrix elements of a normally ordered monomial can be calculated directly using equation (2.27). In order to calculate the matrix elements of a polynomial P that defines exactly m selection rules, we notice that each basis element $|n_1 n_2 n_3 n_4\rangle$ is coupled to exactly m basis elements. More precisely, the expression for $P|n_1 n_2 n_3 n_4\rangle$ is given by

$$\sum_{k=1}^{m} C_k(n_1, n_2, n_3, n_4) |n_1 + \Delta n_1^{(k)}; n_2 + \Delta n_2^{(k)}; n_3 + \Delta n_3^{(k)}; n_4 + \Delta n_4^{(k)}\rangle, \tag{3.7}$$

where $\{\Delta n_1^{(k)}, \Delta n_2^{(k)}, \Delta n_3^{(k)}, \Delta n_4^{(k)}\}$ are the selection rules and $C_k(n_1, n_2, n_3, n_4)$ are the corresponding matrix elements.

Finally, the expressions for the matrix elements are transcribed into Fortran code using the Maple instruction:

$$\texttt{codegen[fortran]}(\texttt{ELEMENT}, \texttt{precision} = \texttt{double}, \texttt{optimized}),$$

where `ELEMENT` is the array that contains the matrix elements.

3.2 Construction of the basis set

As described in section 2.4.4, the basis $|n_1 n_2 n_3 n_4 k\rangle^{+\epsilon_x}$ decomposes into the subspaces of singlet or triplet states, and of even or odd states with respect to the symmetries Π_x and Π_{kl}, with the following identification:

$$\begin{cases} \epsilon_x = \pm 1 & \text{even or odd states with respect to } \Pi_x, \\ n_1 - n_2 \equiv n_3 - n_4 \equiv 0 (\mathrm{mod}\, 4) & \text{singlet states}, \\ n_1 - n_2 \equiv n_3 - n_4 \equiv 2 (\mathrm{mod}\, 4) & \text{triplet states}, \\ k + l \equiv 0 (\mathrm{mod}\, 2) & \text{even states with respect to } \Pi_{kl}, \\ k + l \equiv 1 (\mathrm{mod}\, 2) & \text{odd states with respect to } \Pi_{kl}. \end{cases} \tag{3.8}$$

However, due to the double symmetrization ((2.37) followed by (2.57)) of the basis, each element of the symmetrized basis can be represented by four quadruplets (n_1, n_2, n_3, n_4), (n_2, n_1, n_4, n_3), (n_3, n_4, n_1, n_2) and (n_4, n_3, n_2, n_1), and only one of them must be contained in the basis. Nevertheless, the basis can be defined non-ambiguously for $\epsilon_x = 1$ if each quadruplet (n_1, n_2, n_3, n_4) satisfies one of the following conditions:

$$\begin{cases} l > 0 \quad \text{and} \quad n_1 \geq n_3, \\ l = 0 \quad \text{and} \quad n_1 > n_3 \quad \text{and} \quad n_1 \geq n_4 > n_2, \\ \qquad\quad\;\; n_1 > n_3 \quad \text{and} \quad n_1 > n_2 > n_4, \\ \qquad\quad\;\; n_1 > n_3 \quad \text{and} \quad n_1 = n_2, \\ \qquad\quad\;\; n_1 = n_3 \quad \text{and} \quad n_2 > n_4, \\ \qquad\quad\;\; n_1 = n_3 = n_2 = n_4. \end{cases} \tag{3.9}$$

For the basis generating the odd subspace with respect to the symmetry of the x axis ($\epsilon_x = -1$) the basis states are defined by the same conditions, but the states with $n_1 = n_2 = n_3 = n_4$ are forbidden (see eq. (2.57)).

In addition, for the numerical implementation, the infinite symmetrized basis

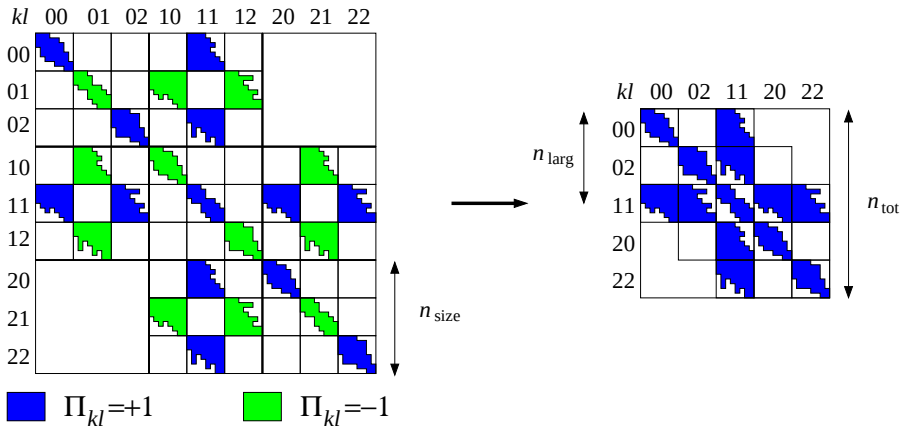

Figure 3.1: General form of the matrices of the GEVP for a basis truncated with $l_{\max} = 2$, $k_{\min} = 0$ and $k_{\max} = 2$, for both subspaces $\Pi_{kl} = \pm 1$ (left), and for the subspace $\Pi_{kl} = +1$ (right).

set has to be truncated. We truncate the basis according to three rules:

$$\begin{aligned} &n_1 + n_2 + n_3 + n_4 \leq n_{\text{base}}, \\ &|l| \leq l_{\max}, \\ &k_{\min} \leq k \leq k_{\max}, \end{aligned} \tag{3.10}$$

for given positive integers n_{base}, $l_{\max}$, $k_{\min}$ and $k_{\max}$.

As we saw in section 2.4.5, for hierarchical ordering with respect to the angular momentum l and k, the matrix representation (2.59) of the eigenvalue problem is given by sparse banded matrices (2.60), and the width of the band n_{larg} depends on the ordering of the basis in n_1, n_2, n_3, n_4. If the size of the basis for the unperturbed problem (i.e., for a given k) is n_{size}, the size of the whole matrix corresponding to a given subspace with fixed generalized parity Π_{kl} is $n_{\text{tot}} \simeq n_{\text{size}}(k_{\max} - k_{\min} + 1)/2$, and the width of the band n_{larg} is bigger than $n_{\text{size}}/2$. For small values of $l_{\max}$, n_{larg} is of the order of n_{size} (s. figure 3.1). Moreover, in this case the bandwidth does not change under variation of $k_{\min}$ and $k_{\max}$ whilst keeping the ordering of the basis $|n_1 n_2 n_3 n_4 k\rangle^{+\epsilon_x}$ with respect to the quantum numbers n_1, n_2, n_3, n_4 fixed, and one obtains the estimate

$$\frac{1}{k_{\max} - k_{\min} + 1} \leq \frac{n_{\text{larg}}}{n_{\text{tot}}} \leq \frac{2}{k_{\max} - k_{\min} + 1}. \tag{3.11}$$

Thus, with hierarchical ordering, the ratio $n_{\text{larg}}/n_{\text{tot}}$ decreases with the number of photons. However, for small number of photons, n_{larg} is of the order of n_{tot}.

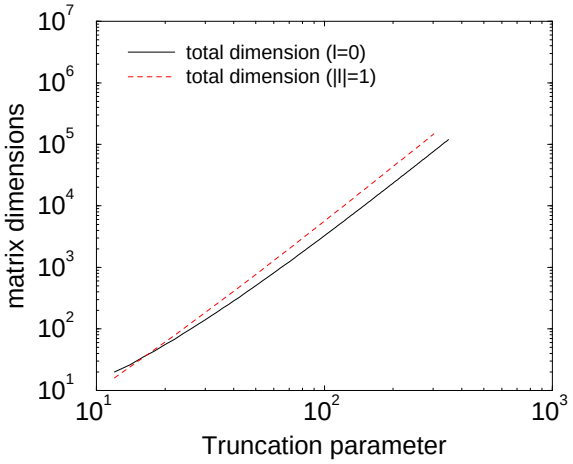

Figure 3.2: Diagonal dimension n_{tot} of the GEVP (2.59) as a function of n_{base} (see (3.10)), for $l = 0$ (solid line) and $|l| = 1$ (dashed line), according to (3.12).

In practice, the dimensions of the matrices which give good converged eigenvalues and eigenvectors are very large: for a fixed value of k and angular momentum $l = 0$, the number of elements along the diagonal scales as $n_{\mathrm{size}} \simeq n_{\mathrm{base}}^3/360$, and for a given angular momentum $|l| > 0$, $n_{\mathrm{size}} \simeq n_{\mathrm{base}}^3/180$ (s. figure 3.2). In the general case, the number of photons and the number of angular momenta have to be included:

$$n_{\mathrm{tot}} \simeq \frac{n_{\mathrm{base}}^3}{180}(k_{\mathrm{max}} - k_{\mathrm{min}} + 1)\left(l_{\mathrm{max}} + \frac{1}{2}\right). \tag{3.12}$$

Typically, for an accurate description of the 15th series of doubly excited states of unperturbed 2D helium $n_{\mathrm{tot}} = 119460$ ($n_{\mathrm{base}} = 350$), and for driven frozen planet states of the 6th series $n_{\mathrm{tot}} = 521795$. This rather slow convergence of the eigenvalues (and eigenvectors) can be understood if we consider the explicit form of the coordinate representation of the basis elements – which can be expressed as the product of two functions of the form given in (2.65). As explained in section 2.5.1, the asymptotic behavior of these wave functions is given by $e^{-\sqrt{r_1+r_2}}$, where r_1 and r_2 are the distances of the electrons from the nucleus. On the other hand, since the Coulomb interaction vanishes at long distances, 2D helium eigenfunctions are expected to decay exponentially (i.e., as $e^{-(r_1+r_2)}$) (see appendix B.3 and equation (B.30)). Therefore, in order to reproduce 2D helium eigenstates, we need a large number of basis elements.

Coming back to the matrix dimensions of the GEVP, using hierarchical ordering of the basis, the bandwidths in the given examples are $n_{\mathrm{larg}} = 11616$ for the unperturbed case, and $n_{\mathrm{larg}} = 114761$ for the driven case. In terms of memory needed to store such matrices, this requires 22 GB and 958 GB, respectively. However, as already pointed out, the bandwidth of the matrices depends on the ordering of the basis, and both the required memory space as well as the total number of floating point operations carried out to diagonalize such matrices depends on the bandwidth.

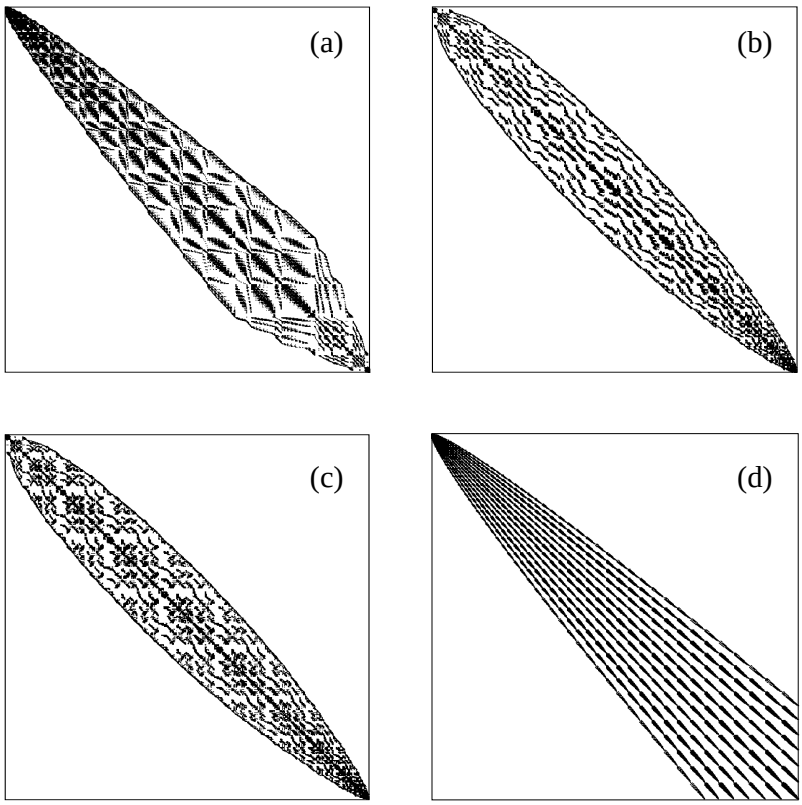

Figure 3.3: Matrix structure for $n_{\mathrm{base}} = 120$ ($n_{\mathrm{tot}} = 5456$), $l = 0$, singlet states, and $\epsilon_x = +1$, for different orderings of the basis set. In (a)−(c) the ordering is obtained with the propagation algorithm for $n_{\mathrm{repeat}} = 1,\ 2$ and 8, respectively, and $n_{\mathrm{fix}}^{(i)} = i \times n_{\mathrm{tot}}/20,\ i = 1, 2, \ldots, 8$. In (d) hierarchical ordering is used.

Finding the optimal permutation of the basis that yields the minimum value of n_{larg} in limited time is a particular case of an open problem of graph partitioning, and several heuristic algorithms have been developed for this

purpose [72–74]. We use a recursive algorithm developed by B. Grémaud [75] that considerably reduces the bandwidth of the matrices. In order to describe this algorithm, let us use the short hand notation $|\alpha\rangle = |n_1 n_2 n_3 n_4 k\rangle^{+\epsilon_x}$ and $\Delta\alpha = \{\Delta n_1, \Delta n_2, \Delta n_3, \Delta n_4, \Delta k\}$ for a given basis state and a given selection rule, respectively.

There are two principal parts of the algorithm:

1. A basis defined by the conditions (3.8), (3.9) and (3.10) is constructed recursively, starting with an arbitrary basis state $|\alpha_1^{(1)}\rangle$, according to the recursion law

   (a) $|\alpha_2^{(1)}\rangle = |\alpha_1^{(1)} + \Delta\alpha_1\rangle$, $|\alpha_3^{(1)}\rangle = |\alpha_1^{(1)} + \Delta\alpha_2\rangle$, and so on until all selection rules are exhausted.

   (b) Step (a) is repeated starting with the seed state $|\alpha_2^{(1)}\rangle$, then with $|\alpha_3^{(1)}\rangle$, etc. If at some point a basis element is met that was already found, it is not included again in the basis.

   Due to the truncation of the basis the algorithm stops at some point. Furthermore, since all symmetries of the problem are already considered in the conditions (3.8), (3.9) and (3.10), all basis elements are coupled by the selection rules. Therefore the recursion described above generates all basis elements as a sequence $|\alpha_1^{(1)}\rangle$, $|\alpha_2^{(1)}\rangle, \ldots,$ $|\alpha_{n_{\mathrm{tot}}}^{(1)}\rangle$.

2. Once the basis is constructed for the first time the process begins again, but this time the initial basis state is the last basis state generated during the preceding ordering cycle: $|\alpha_1^{(2)}\rangle = |\alpha_{n_{\mathrm{tot}}}^{(1)}\rangle$. Additionally, $n_{\mathrm{fix}}^{(2)}$ states of the preceding ordering are kept fixed, i.e. $|\alpha_i^{(2)}\rangle = |\alpha_{n_{\mathrm{tot}}-i+1}^{(1)}\rangle$ for $i = 1, 2, \ldots, n_{\mathrm{fix}}^{(2)}$.

   This procedure is repeated n_{repeat} times (for $n_{\mathrm{repeat}} = 1$, only step 1 of the algorithm is applied).

To understand the action of the algorithm let us observe figure 3.3, where we show the structure of the matrices generated by subsequent iterations of the propagation algorithm (in (a), (b) and (c)), in comparison to the matrix obtained with hierarchical ordering (in (d)), for $n_{\mathrm{base}} = 120$, $l = 0$, singlet states, and $\epsilon_x = +1$. Non vanishing matrix elements are represented by dots, and the diagonal size of the matrices is $n_{\mathrm{tot}} = 5456$. After the first step of the algorithm a sparse banded matrix is obtained, and the widths of its columns increases monotonously until a certain point (around the 3000th column) where the width is maximal ($n_{\mathrm{larg}}^{(1)} = 1194$). Beyond that point the

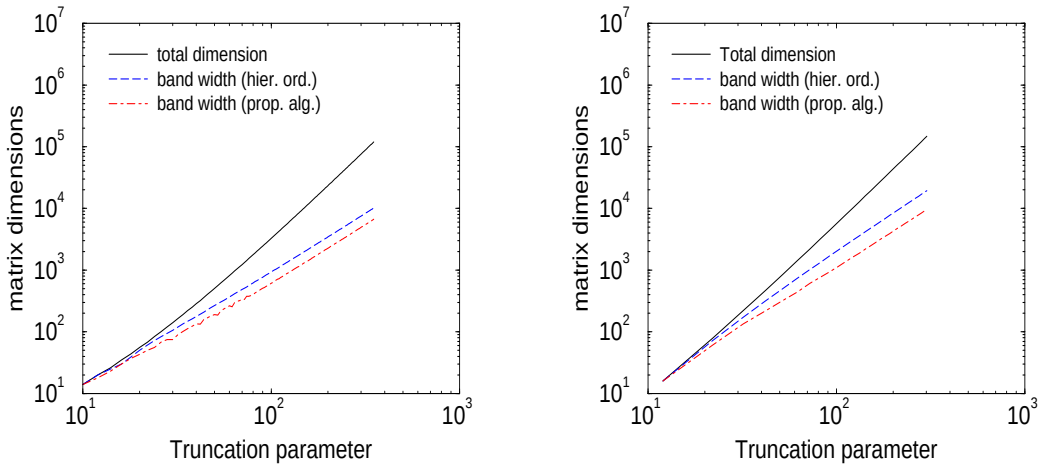

Figure 3.4: $n_{\rm tot}$ (solid line) and $n_{\rm larg}$ (dashed and dotted lines) as a function of $n_{\rm base}$, for $l = 0$ (left) and $l = 1$ (right). The dashed lines are the values of $n_{\rm larg}$ obtained by hierarchical ordering, while the dash-dotted lines are obtained by the propagation algorithm.

width rapidly decreases due to the truncation of the basis. The algorithm takes advantage of this decrease, and fixing the last $n_{\rm fix} = 272$ basis elements the bandwidth after $n_{\rm repeat} = 2$ is $n^{(2)}_{\rm larg} = 864$. Typically, for $n_{\rm repeat} > 2$, the bandwidth improves only slightly. For instance in figure 3.3(c) obtained with $n_{\rm repeat} = 8$ and $n^{(i)}_{\rm fix} = i \times n_{\rm tot}/20$, for $i = 2, 3, \ldots, n_{\rm repeat}$, the bandwidth is $n^{(8)}_{\rm larg} = 861$. Nevertheless, in all our numerical calculations we use $n_{\rm repeat} = 8$.

For the general case of the periodically driven atom we have tested several choices for $n^{(i)}_{\rm fix}$, and it turns out as an "experimental" finding that $n^{(i)}_{\rm fix} = i \times n_{\rm tot}/20$ is a good one.

For the field-free case, the propagation algorithm improves the bandwidth of the matrix approximately by a factor 2 (Fig 3.4 and 3.6). In the general driven case, the improvement depends on the number of photons. For small number of photons (Fig. 3.5) the value of $n_{\rm larg}$ obtained with the propagation algorithm is again approximately two times smaller than the value obtained by hierarchical ordering, though for large photon numbers the values obtained with either method are approximately equal. For instance, for $n_{\rm base} = 200$, $l_{\rm max} = 3$, $k_{\rm min} = -2$ and $k_{\rm max} = 4$, the values of $n_{\rm larg}$ obtained with the propagation algorithm and by hierarchical ordering are 50717 and 114761, respectively, while for $n_{\rm base} = 80$, $l_{\rm max} = 16$, $k_{\rm min} = 0$ and $k_{\rm max} = 25$,

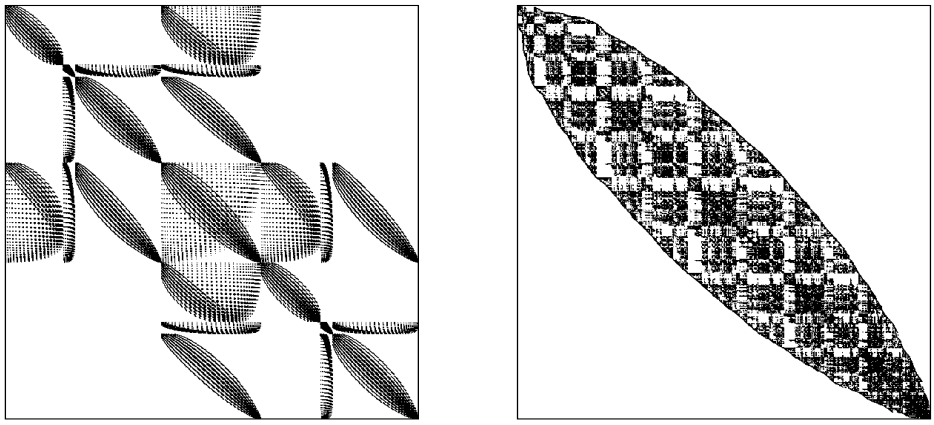

Figure 3.5: Matrix structure for $n_{\text{base}} = 80$, $0 \leq k \leq 2$ and $l_{\text{max}} = 2$. The dimension of the matrix is $n_{\text{tot}} = 12354$. The bandwidth using hierarchical ordering of the basis (left) is $n_{\text{larg}} = 7626$, while the propagation algorithm yields $n_{\text{larg}} = 2920$.

$n_{\text{larg}} = 17983$ vs. $n_{\text{larg}} = 18026$. In the first case, with $n_{\text{tot}} = 521795$, the required memory for matrix storage amounts to 958 GB for hierarchical ordering, compared to only 424 GB when the propagation algorithm is used.

3.3 Lanczos algorithm

Along this work we will be interested in the spectral structure as well as in the localization properties of specific quantum states of the unperturbed 2D helium atom or in the dynamics and stability properties of the driven atom. Therefore we need specific eigenvalues and eigenstates of the eigenvalue problems (2.12) and (2.59). As we saw in the previous section, the typical dimensions of the involved matrices become rather large in the spectral range of highly excited states and/or in the presence of the external field, which couples different angular momenta. However, we do not need to extract all the eigenvalues and eigenstates, but only those in a given spectral region of interest, which is either defined by the initial state in which the atom is prepared in a specific experimental setting, or by the energy range which is probed, e.g., in an experimental scan of a suitably defined cross section.

The Lanczos routine provides an algorithm suitable for precisely this task, and finds a few eigenvalues and eigenvectors of a huge eigenvalue problem in

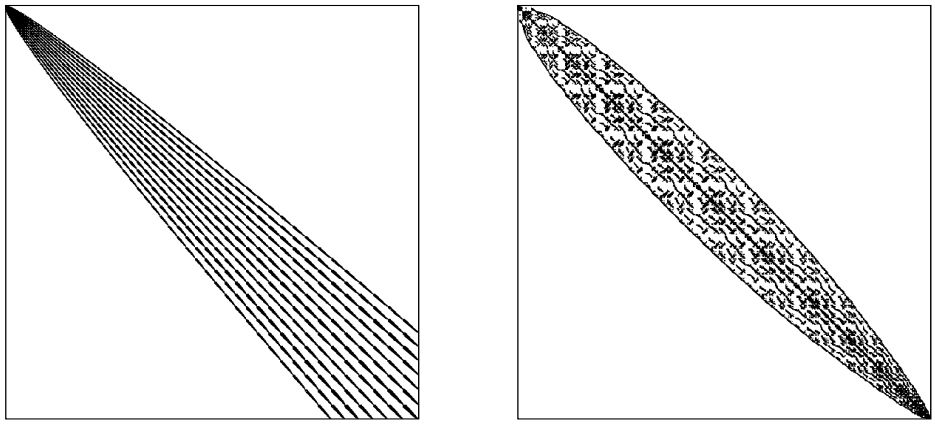

Figure 3.6: Matrix structure for $n_{\text{base}} = 150$, and $l_{\max} = 0$. The dimension of the matrix is $n_{\text{tot}} = 10260$. The bandwidth with hierarchical ordering of the basis (left) is $n_{\text{larg}} = 1996$, vs. $n_{\text{larg}} = 1312$, with the propagation algorithm.

the vicinity of some predefined position on the energy axis. More specifically, this algorithm was originally developed to find a few extremal eigenvalues of a large symmetric matrix, along with the associated eigenvectors [76,77], and later [78] adapted for generalized symmetric eigenvalue problems $\mathcal{A}\boldsymbol{x} = \varepsilon\mathcal{B}\boldsymbol{x}$ of dimension n_{tot}. In this case the GEVP is equivalent to an eigenvalue problem obtained by multiplication from the left with $\mathcal{A}^{-1}$

$$\mathcal{A}^{-1}\mathcal{B}\boldsymbol{x} = \mu\boldsymbol{x}, \tag{3.13}$$

where $\mu = 1/\varepsilon$. The Lanczos algorithm finds the largest values of μ (i.e. $\varepsilon_i \simeq 0$). Since, in our specific case, we will be interested in the eigenvalues in the vicinity of some energy E_s, we have to shift the matrix $\mathcal{A}$ by E_s before diagonalizing it with the Lanczos routine, i.e.

$$\mathcal{A} \to \mathcal{A} - E_s\mathcal{B}. \tag{3.14}$$

In the Lanczos algorithm a set $\boldsymbol{q}_1,\ \boldsymbol{q}_2, \ldots,\ \boldsymbol{q}_{n_{\text{lancz}}}$ ($n_{\text{lancz}} \leq n_{\text{tot}}$) of orthogonal column vectors of dimension n_{tot} is iteratively constructed in such a way that the matrix $\mathcal{Q} = (\boldsymbol{q}_1, \boldsymbol{q}_2, \ldots, \boldsymbol{q}_{n_{\text{lancz}}})$ be an orthogonal matrix with respect to $\mathcal{B}$ (i.e., $\mathcal{Q}^T\mathcal{B}\mathcal{Q} = 1$, where $\mathcal{Q}^T$ is the transpose matrix of $\mathcal{Q}$), which transforms

the matrix $\mathcal{A}^{-1}\mathcal{B}$ into a tridiagonal matrix $\mathcal{A}^{-1}\mathcal{B}\mathcal{Q} = T\mathcal{Q}$, where

$$T = \begin{pmatrix} \alpha_1 & \beta_1 & 0 & \dots & 0 & 0 \\ \beta_1 & \alpha_2 & \beta_2 & \dots & 0 & 0 \\ 0 & \beta_2 & \alpha_3 & \dots & 0 & 0 \\ \vdots & \vdots & \vdots & \ddots & \vdots & \vdots \\ 0 & 0 & 0 & \dots & \alpha_{n_{\text{lancz}}-1} & \beta_{n_{\text{lancz}}-1} \\ 0 & 0 & 0 & \dots & \beta_{n_{\text{lancz}}-1} & \alpha_{n_{\text{lancz}}} \end{pmatrix}. \tag{3.15}$$

Then the largest eigenvalues μ_i of (3.13) are given by the eigenvalues of T.

The j-th matrix elements α_j and β_j of T are obtained from the jth column of $\mathcal{A}^{-1}\mathcal{B}\mathcal{Q} = T\mathcal{Q}$, taking into account that the vectors $\boldsymbol{q}_j$ are orthonormal with respect to $\mathcal{B}$. Thus, choosing an arbitrary normalized initial vector $\boldsymbol{q}_1$, the iterative formulae read [77, 79]

$$\begin{cases} \alpha_j &= \boldsymbol{q}_j^T \mathcal{B}\mathcal{A}^{-1}\mathcal{B}\boldsymbol{q}_j, \\ \beta_j &= \|\boldsymbol{t}_{j+1}^T \mathcal{B} t_{j+1}\|, \text{ with } \boldsymbol{t}_{j+1} = \mathcal{A}^{-1}\mathcal{B}\boldsymbol{q}_j - \alpha_j \boldsymbol{q}_j - \beta_{j-1}\boldsymbol{q}_{j-1}, \\ \boldsymbol{q}_{j+1} &= \dfrac{1}{\beta_{j+1}} \boldsymbol{t}_{j+1}. \end{cases} \tag{3.16}$$

From this relations we note that the matrix $\mathcal{A}^{-1}$ is never used explicitly, but only products of the type $\mathcal{A}^{-1}\mathcal{B}\boldsymbol{x}$. It is therefore not necessary to invert $\mathcal{A}$. Instead, using the LL^T factorization of $\mathcal{A}$ [80] the vector $\boldsymbol{x} = \mathcal{A}^{-1}\mathcal{B}\boldsymbol{x}$ can be found solving the linear system of equations $\mathcal{A}\boldsymbol{x} = \mathcal{B}\boldsymbol{x}$ by backward substitution [80].

Therefore the Lanczos algorithm is composed of three fundamental steps:

1. LL^T factorization of $\mathcal{A}$.
2. n_{lancz} iterations of the recursive expressions (3.16), in order to find T.
3. Diagonalization of T, which can be diagonalized by standard diagonalization routines like the $QR-$decomposition [80].

3.4 Numerical implementation

In section 3.2 we already discussed the typical sizes of the matrices we need to diagonalize. Such matrices cannot be stored in the main memory of standard PC's, and therefore the corresponding eigenvalue problem cannot be

numerically solved using them. Instead, it can be solved on parallel computers, where all processing elements work simultaneously on different parts of the problem, and therefore special techniques of parallel programming have to be used. In this section we discuss the principal features of the parallel implementation of our code, starting with an introduction on parallel programming.

3.4.1 Basic notions of parallel programming

In a parallel program different parts of the problem are distributed on several processing elements of a given parallel computer. Thus, the program speeds up by some factor not bigger than the number of processing elements. As the handling of the memory is concerned, there are two basic concepts: *shared memory* computers, where each processing element has access to the entire memory, and *distributed memory* computers, where the memory is distributed over different processing elements. However, in the new generation of supercomputers a mixture of both concepts is used, called *hybrid architecture*, where subgroups of processing elements (e.g., eight in the case of the HITACHI SR8000-F1 [81], or thirty-two in the case of the IBM p690 [82]) form nodes with shared memory and the nodes are organized as distributed memory machines.

In our specific case the matrices $\mathcal{A}$ and $\mathcal{B}$ are splitted into smaller matrices, which are treated locally on the processing elements. During the diagonalization of the eigenvalue problem each of the processing elements exchanges information with the others. Therefore, for the design of it is of crucial importance to optimize the interaction between the single processing elements, besides, of course, an efficient sequential computation. There is special message passing software to ease the communication between different processing elements, like MPI [83,84] (Message Passing Interface), or PVM (Parallel Virtual Machine). Additionally, there are special message passing libraries for shared memory architectures like OpenMP (Open Message Passing), or vendor specific libraries like COMPAS in the case of the HITACHI SR8000-F1.

Since MPI appears to become standard [85] and is portable between different machines, we choose it for the implementation of our code. Also on the HITACHI SR8000-F1 we combine MPI with COMPAS which is easily implementable [86].

In MPI, there are basically two forms of communication:

- Point-to-point communication: a single processing element sends or

receives a message to or from another processing element.

- Collective communication: in this case several processing elements are involved, i.e., a single processing element sends or receives a message to or from all the other processing elements, all processing elements are synchronized at some point, or global reduction operations (maximum, minimum, sum, etc) of data distributed over all processing elements are performed.

With the help of MPI an existing scalar code can be transformed into a parallel code using these communication elements. One only needs to choose carefully where to place the communication directives, and whether communication with a single or with all processing elements is preferable, in order to achieve optimal efficiency of the code.

The speed-up $S(p)$ of a code running on p processing elements is defined as [79]

$$S(p) = \frac{T(1)}{T(p)}, \tag{3.17}$$

where $T(p)$ is the execution time on p processing elements. Thus the efficiency $E(p)$ is given by

$$E(p) = \frac{S(p)}{p} = \frac{T(1)}{pT(p)}. \tag{3.18}$$

In an efficient parallel code the time required for communication is short compared with the time spent for purely local operations, i.e., $E(p) \to 1$. However, since there is always a fraction of the calculation that has to be solved sequentially, it is impossible to achieve efficiency $E(p) = 1$.

3.4.2 Storage of the matrices

As already described in section 3.2, the matrices $\mathcal{A}$ and $\mathcal{B}$ are complex symmetric banded sparse matrices. Therefore all information is contained in the lower triangular band. In addition, the recursion relations (3.16) show that the matrix $\mathcal{B}$ is only used to calculate products with vectors $\boldsymbol{x}$ of the type $\mathcal{B}\boldsymbol{x}$. Thus we do not need to store the whole matrix, but only its non-vanishing elements, which are very few (at most the number of selection rules, per row) compared to the total dimension of the matrix. However, in the course of the LL^T decomposition of $\mathcal{A}$ we *do* need all storage space occupied by the lower triangular band since L is not sparse anymore, and we have to distribute it over n_{procs} processing elements. Since the memory needed to store a complex

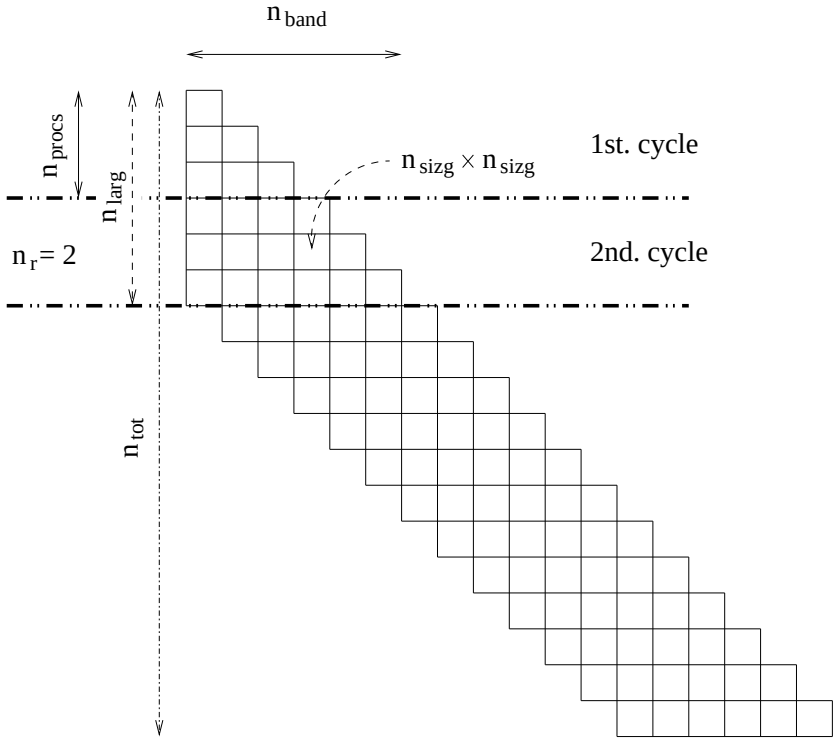

Figure 3.7: Partitioning of the matrices: n_{larg} and n_{tot} are the bandwidth and the dimension, respectively; n_{sizg} is the dimension of the subblocks; n_{band} is the number of subblocks in a line, and n_{r} is the number of such lines per processing element that are contained in the bandwidth.

array of n_{larg} by n_{tot} is $(16 \times n_{\text{larg}} \times n_{\text{tot}}/2^{30})$ GB, the number of processing elements is approximately given by

$$n_{\text{procs}} = \frac{16 \times n_{\text{larg}} \times n_{\text{tot}}}{M}, \tag{3.19}$$

where M is the accessible memory per processing element given in Bytes. On the HITACHI SR8000-F1, $M \simeq 800$ MB for a pure MPI application, while combining MPI with COMPAS allow for $M \simeq 6.5$ GB. On the IBM p690, where we use MPI alone, two kinds of processors with $M \simeq 8$ GB or $M \simeq 2$ GB are available.

For the distribution on the different processors, the matrix $\mathcal{A}$ is partitioned into $n_{\text{sizg}} \times n_{\text{sizg}}$ blocks as sketched in figure 3.7, such that

$$n_{\text{larg}} = n_{\text{r}} \times n_{\text{procs}} \times n_{\text{sizg}}, \tag{3.20}$$

where $n_{\rm r}$ is an integer number which represents the number of lines of $n_{\rm band} = n_{\rm r} \times n_{\rm procs}$ of the $n_{\rm sizg} \times n_{\rm sizg}$ blocks that each processing element has to process until a $n_{\rm larg} \times n_{\rm larg}$ block of the matrix is completed. To complete an operation through the whole matrix requires to process $n_{\rm cycle}$ lines, where

$$n_{\rm cycle} = \frac{n_{\rm tot}}{n_{\rm larg} \times n_{\rm procs}}. \tag{3.21}$$

Any vector is stored in the same way, since it can be seen as a banded matrix of bandwidth 1. However, the storage of the matrix $\mathcal{B}$ is completely different: whilst $\mathcal{B}$ is also complex symmetric sparse banded, and therefore has the structure depicted in figure 3.7, in each processing element only the non vanishing matrix elements in the lower band are stored, in an array of length $n_{\rm b}(PE)$, for $PE = 1, 2, \ldots, n_{\rm procs}$. In addition, we keep track of the position of the elements of that array in the $n_{\rm sizg} \times n_{\rm sizg}$ blocks, as well as of the position of the respective block itself.

Finally, we point out that most of the local calculations on the $n_{\rm sizg} \times n_{\rm sizg}$ blocks are carried out using BLAS (Basic Linear Algebra Subprograms, and here in particular BLAS 3 for matrix-matrix operations). These subroutines are standarized, and optimized on most computers.

3.4.3 Implementation of the Lanczos algorithm

After filling the matrices $\mathcal{A}$ abd $\mathcal{B}$ as described in the preceding section, the generalized eigenvalue problem is diagonalized using the Lanzos algorithm (3.16) already described in section 3.3. To complete those iterations we need routines that carry out three operations: scalar product between two vectors, product between the matrix $\mathcal{B}$ and a vector, and products of the form $\mathcal{A}^{-1}\mathcal{B}\boldsymbol{x}$ using LL^T decomposition and backward substitution (here $\boldsymbol{x}$ is a vector). The first and second operations can be easily implemented using BLAS, however the situation is a bit more complicated for the third operation. A detailed description of the implementation of the LL^T decomposition and of the backward substitution is given in [79].

3.4.4 Performance of the code

The speed of a computer is characterized by the performance of the CPU (central process unit), which is measured by the number of floating point operations per second (Flops). Thus the performance of a parallel code

Table 3.1: Performance of the parallel code on the HITACHI SR8000-F1, with and without COMPAS, and on the IBM, for different realistic problem dimensions $n_{\text{tot}} \times n_{\text{band}}$, and different numbers of processing elements and of nodes.

n_{tot}	n_{band}	Memory (GB)	Number of nodes	Number of procs	Performance (Mflops)		
					HITACHI		IBM
					No COMPAS	COMPAS	
44704	3463	9.5	7	56	276	– – –	– – –
96957	12314	38.0	10	80	202	284	– – –
119460	6662	23.4	11	88	300	– – –	– – –
119460	6662	23.4	1	8	– – –	– – –	1041
296632	26027	127.0	32	256	– – –	254	– – –
296632	26027	127.0	1	32	– – –	– – –	1750
347876	30759	171.2	1	32	– – –	– – –	1850
521795	50717	423.4	16	512	– – –	– – –	783

can be measured in terms of MFlops (10^6Flops) achieved per processing element. In addition, a well performing parallel code should be scalable, i.e., the solution of a large problem should achieve the same performance per processing element as the solution of a smaller problem, where the number of processing elements is smaller. As mentioned above, we use BLAS to achieve good single processing element performance. However, to achieve an optimal single processing element performance, n_{sizg} can be tuned in order to (a) optimize BLAS performance (limited by the latency of memory access), (b) minimize the communication overhead between different processors, and (c) minimize the required memory for storage of the entire matrix (which is subjected to finite size effects due to the discrete partitions of the matrix, see figure 3.7). In addition, typically, the accessible number of processors is multiple of 32 (on the IBM p690) or 8 (on the HITACHI SR8000-F1) which further constrains the possible choices of n_{sizg}. In our numerical calculations, n_{sizg} is chosen as an integer value between 30 and 400, for which the required memory M for matrix storage per processing element is minimal.

Under these conditions, typical mono processor performances achieved by the code are shown in table 3.4.4. On the Hitachi the code presents good scalability with a peak performance of 300 MFlops (which is a factor five smaller than the peak performance, and a factor 2.5 larger than the most unfavorable case [81]). With the implementation of COMPAS the perfor-

mance improves slighty. On the IBM the situation is much better. The top performance we achieved is 1850 MFlops, what represents more than 30% of the peak performance [82].

3.5 Applications

3.5.1 Ground state of the 2D helium atom

As a first example of our numerical approach, we show a very simple calculation, the ground state of the 2D three body Coulomb problem as a function of the electron-electron interaction γ (s. eq. (2.2)). We compare the numerical result with first order perturbation theory, considering the electron-electron interaction as a perturbative potential. The expected value of $1/r_{12}$ in the ground state $|\psi_0\rangle$ without electron-electron interaction is given by [38]

$$\langle\psi_0|\frac{1}{r_{12}}|\psi_0\rangle = \frac{3\pi Z}{4}. \tag{3.22}$$

Therefore, the ground state energy at first order in γ is $E = E_0 + \Delta E$, where $\Delta E = 3\pi Z\gamma/4$, and $E_0 = -16\,\text{a.u.}$ is the energy of the ground state of the planar three body problem without electron-electron interaction (s. eq. (B.31)).

For the numerical calculation of the ground state (and in general of any bound state of the first series of Rydberg states) we do not need to use complex rotation (i.e., $\theta = 0$), since it is not a decaying state. However, due to the truncation of the basis, the energy depends on the dilation parameter α. The variational character of α can be seen in the left plot of figure 3.8, where the dependence of the energy of the 2D He ($Z = 2,\ \gamma = 1$) ground state on α is shown for $n_{\text{base}} = 60$ ($n_{\text{tot}} = 816$). For $0.26 \leq \alpha \leq 0.5$, the numerical values are stable, and for α around 0.36 the curve has a minimum. In this way we obtain for the ground state energy

$$E = -11.899822342953\,\text{a.u.} \tag{3.23}$$

In the right plot of figure 3.8 we corroborate the linear behavior of the energy of the ground state of the 2D three body Coulomb problem as a function of the electron-electron interaction γ, as predicted by first-order perturbation theory, for small values of γ ($\gamma \leq 0.3$).

As described in appendix B.3, the wave functions of the states of the planar three body Coulomb problem without e-e interaction have analytic expres-

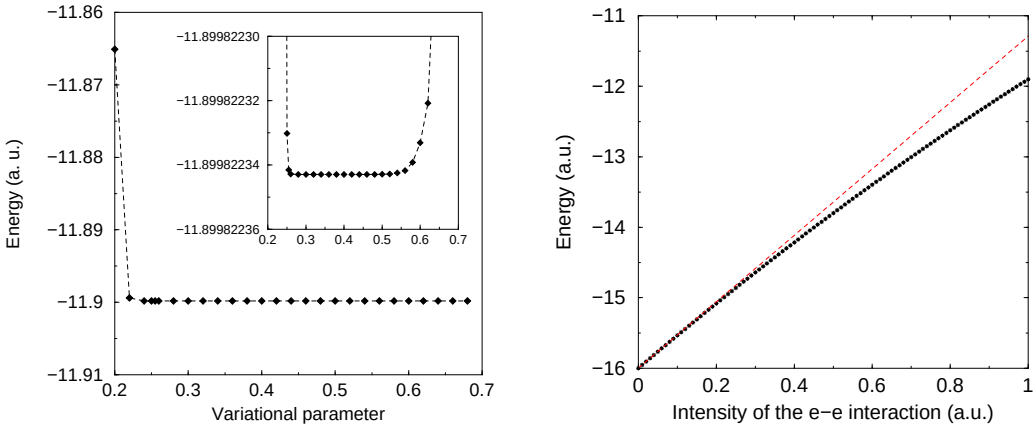

Figure 3.8: Dependence of the energy of the ground state of the 2D helium atom ($\gamma = 1$) on the dilation parameter α for $n_{\text{base}} = 60$ (left), and energy of the ground state as a function of the strength γ of the electron-electron interaction (right). In the right plot, the dashed line is obtained from first order perturbation theory, while the stars are our numerical results.

sions. As an example, the probability density of the ground state is

$$|\psi_0(r_1, r_2)|^2 = \frac{64}{\pi^2} Z^4 e^{-4Z(r_1+r_2)}. \tag{3.24}$$

In figure 3.9 we can see the perfect agreement between the numerical (circles) and analytic (solid line) results. For instance, at $r_1 = r_2 = 0$ the analytic and the numerical values of the probability density are $|\psi_0(0,0)|^2 = \frac{64}{\pi^2} Z^4 = 103.7528920$.

Any probability in parabolic coordinates has to be multiplied by the Jacobian $B = 16 r_1 r_2 r_{12}$ of the transformation. Therefore all wave functions presented in the sequel of this work are obtained after multiplication with the Jacobian. In figure 3.10 we show the probability density of the 2D He ground state with (left) and without (right) e-e interaction projected on the x axis. As expected, the inclusion of the Coulomb repulsion broadens the probability density, and the electrons are more separate, as obvious from the positions of the maxima in these plots.

3.5.2 Resonant coupling between $|1s1s\rangle$ and $|1s2p\rangle$

We first consider the case of 2D He without electron-electron interaction. In appendix B.3 the corresponding energy eigenvalues are calculated. From

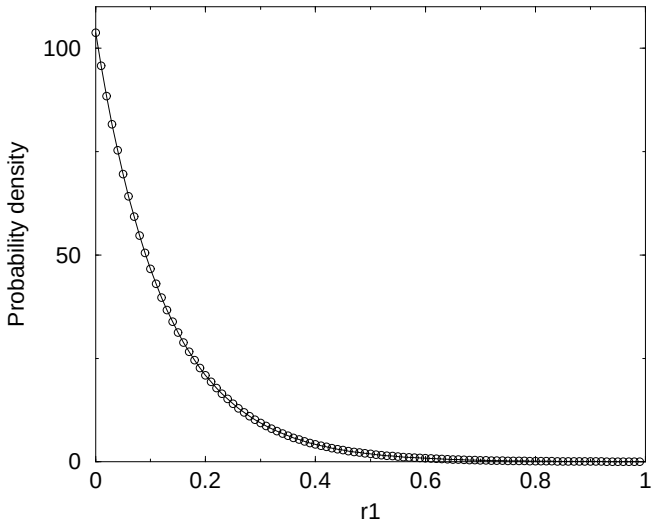

Figure 3.9: Probability density of the 2D He ground state without electron-electron interaction, for $r_2 = 0$. The solid line is the analytical result (3.24), while the circles are obtained by numerical diagonalization.

(B.31) the energies of $|1s1s\rangle$ and $|1s2p\rangle$ in that case are $E_0 = -16$ a.u. and $E_1 = -80/9$ a.u., respectively. Therefore, a driving field with frequency $\omega_{01} = E_1 - E_0 = 64/9$ will couple the states $|1s1s\rangle$ and $|1s2p\rangle$ resonantly. Furthermore, the state $|2p2p\rangle$, whose energy is $E_2 = -16/9$, will be also coupled. For small values of the field amplitude F the Floquet eigenvalue problem (2.44) can be treated perturbatively [49]. If $F = 0$, the states $|1s1s; k = 0\rangle$, $|1s2p; k = 1\rangle$ and $|2s2p; k = 2\rangle$ are degenerate eigenstates of (2.44). Therefore, in order to calculate the correction ΔE to the energy of the ground state to first order, it is necessary to diagonalize the matrix containing the matrix elements of the field operator $F(x_1 + x_2)/2$ between the states $|1s1s\rangle$, $|1s2p\rangle$, $|2p1s\rangle$ and $|2p2p\rangle$.

For instance, $\langle 1s1s|F(x_1 + x_2)/2|1s2p\rangle = \langle 1s|Fx_2/2|2p\rangle$, where $|1s\rangle$ and $|2p\rangle$ are 2D-hydrogenic eigenfunctions, given essentially by (B.29). Actually, $|2p\rangle$ is a superposition of the two eigenfunctions with $|L| = 1$:

$$\begin{aligned} \langle r|1s\rangle &= 2Z\sqrt{\frac{2}{\pi}}e^{-2Zr}, \\ \langle r|2p\rangle &= \frac{8Z^2}{9}\sqrt{\frac{2}{3\pi}}\cos\phi r e^{-2Zr/3}. \end{aligned}$$

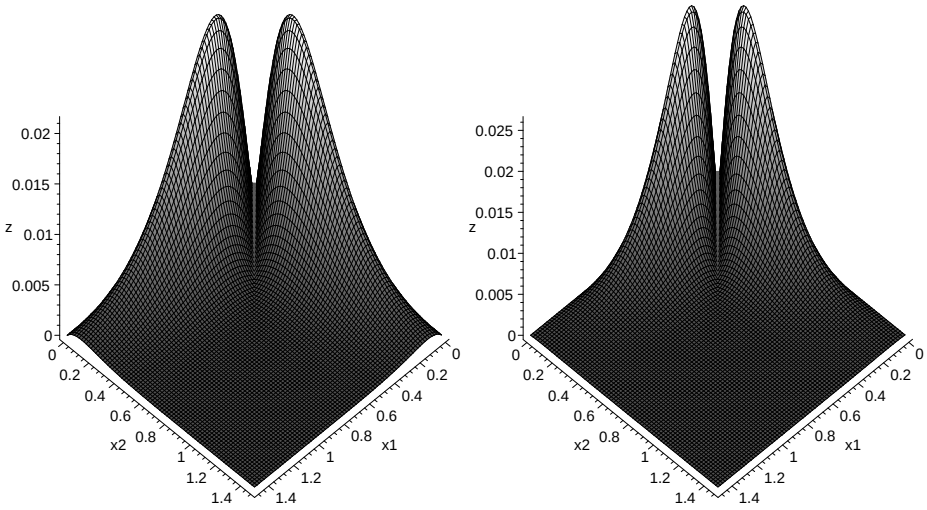

Figure 3.10: x-projection of the probability density of the 2D He ground state with (left) and without (right) electron-electron interaction, projected on the x axis.

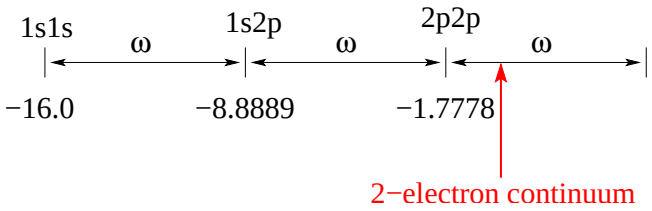

Figure 3.11: Resonant coupling between the states $|1s1s\rangle$, $|1s2p\rangle$, and $|2p2p\rangle$ of the 2D helium atom without electron-electron interaction.

Hence,

$$\langle 1s1s|\frac{F}{2}(x_1+x_2)|1s2p\rangle = \frac{9\sqrt{3}F}{128Z}. \tag{3.25}$$

Analogously, all the remaining matrix elements can be calculated. Indeed, all matrix elements are equal to 0 or are given by (3.25). In addition, since the state $|-\rangle = (|1s2p\rangle - |2p1s\rangle)/\sqrt{2}$ is a triplet state (and therefore not coupled to the ground state), it is enough to diagonalize the matrix that incorporates the states $|1s1s\rangle$, $|2p2p\rangle$ and $|+\rangle = (|1s2p\rangle + |2p1s\rangle)/\sqrt{2}$, i.e.

$$M = \begin{pmatrix} 0 & 0 & z\sqrt{2} \\ 0 & 0 & z\sqrt{2} \\ z\sqrt{2} & z\sqrt{2} & 0 \end{pmatrix}, \tag{3.26}$$

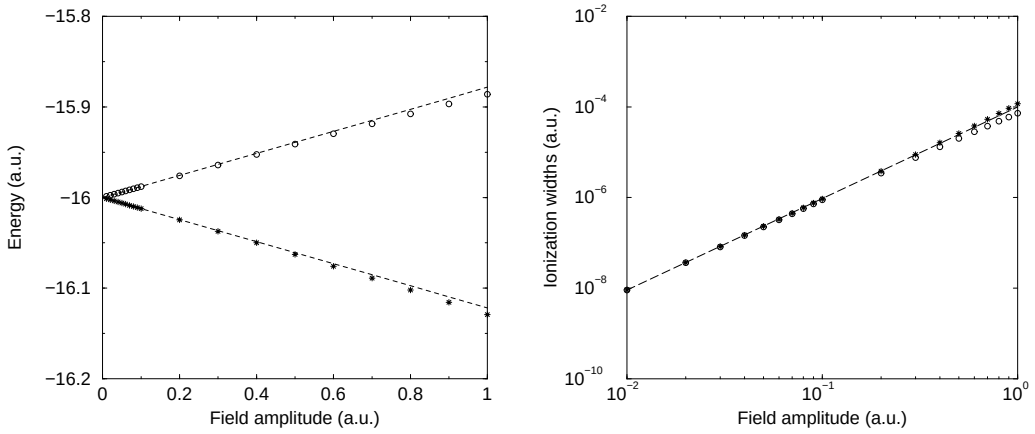

Figure 3.12: Energy (left) and ionization widths (right) of two of the states coupled by resonant driving (see figure 3.11). The dashed lines on the left show the first order approximation (3.27), while dashed line on the right was obtained by a linear fit.

where $z = 9\sqrt{3}F/128Z$ is given by (3.25). The eigenvalues of the matrix M are $0, \ \pm 2z$. Therefore, up to first order in F, the splitting of the energy levels between $E_0 + z$ and $E_0 - z$ is given by

$$\Delta E = \pm \frac{9\sqrt{3}F}{64Z}. \tag{3.27}$$

In figure 3.12 the numerically calculated energies (left plot, circles and stars) and the predictions of first order perturbation theory (dashed lines) are shown. For small values of the field amplitude the energies obtained with both methods coincide, however for bigger values we observe small deviations. In the right plot we show the ionization widths obtained after diagonalization of the rotated Floquet operator (circles and stars). The dashed line represents a linear fit of one of these data sets, on the double-logarithmic scale of the plot. As expected from the Fermi's golden rule [39], the single ionization rates are proportional to F^2.

Including now the electron-electron interaction, the resonant frequency between the states $|1s1s\rangle$ and $|1s2p\rangle$ is $\omega = 3.6882802531$ a.u. In this case the state $|2p2p\rangle$ is not coupled to $|1s1s\rangle$ and $|1s2p\rangle$ anymore, nevertheless the qualitative behavior observed in figure 3.12 has to be the same for small field amplitudes. In the left plot of figure 3.13, the absolute value of the energy shift ΔE (modulo ω for $|1s2p\rangle$) of the resonantly coupled levels is plotted. The circles (stars) correspond to the upwards (downwards) shifted states.

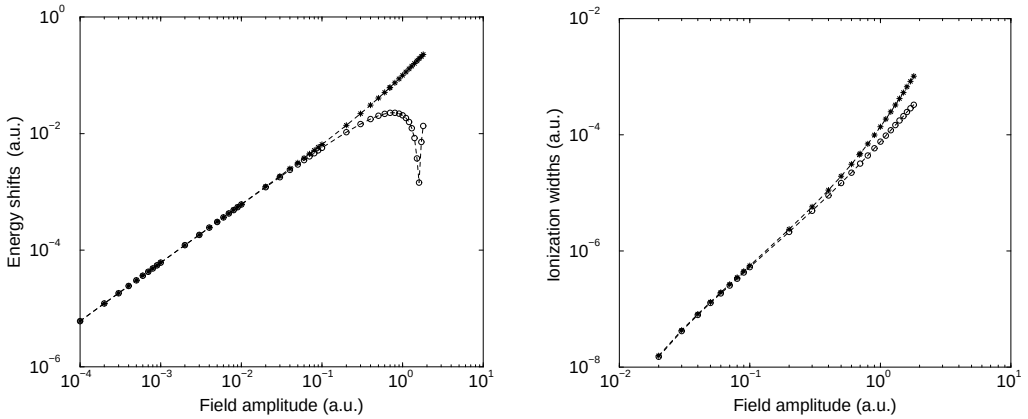

Figure 3.13: Absolute values of the energy shifts ΔE (left), and ionization rates Γ (right) of the resonantly coupled states $|1s1s\rangle$ and $1s2p\rangle$, for $\omega = 3.6882802531$ a.u., as function of the field amplitude F. The circles (stars) represent the dressed state with positive (negative) field-induced energy shift.

For small values of the field amplitude ($F < 2 \times 10^{-2}$ a.u.) the observed behavior coincides with the predictions of first order perturbation theory. At $F \simeq 10^{-1}$ a.u. we observe a significant deviation from first order perturbation theory, and at higher field amplitudes the up-shifted state interacts with excited states, exhibiting avoiding crossings. The associated decay rates are shown in the right plot of this figure, and as expected $\Gamma \sim F^2$ for small values of the field amplitude.

A typical spectrum of the rotated Floquet operator in this case is shown in figure 3.14. As expected from Floquet theory, the spectrum is periodic with period ω, and the continuum is rotated around the multiphoton ionization thresholds $I_N + k\omega$, where $k \in \mathbb{Z}$ and $I_N = -Z^2/2(N - 1/2)^2$. The inset zooms in the first and the second ionization threshold $I_1 = -8$ a.u. and $I_2 = -8/9$ a.u.

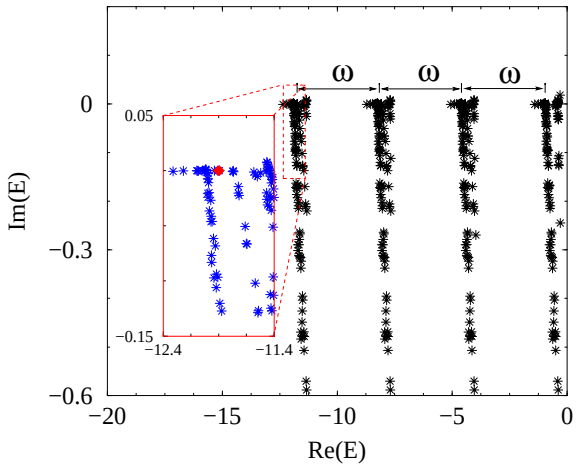

Figure 3.14: Spectrum of the rotated Floquet operator for resonant coupling between the $|1s1s\rangle$ and $|1s2p\rangle$ states of helium, obtained by several runs of the Lanczos algorithm. The shift parameter E_s was chosen close to the photoionization thresholds $I = I_1 + k\omega$, with $k = 0, 1, 2$ and 3, respectively. $\omega = 3.6882802531$ a.u., $n_{\text{base}} = 80$.

Chapter 4

Spectrum of 2D helium

As in the general three dimensional case [6], the eigenstates of 2D helium are organized in Rydberg series converging to single ionization thresholds which all converge to the double ionization threshold at zero energy. The threshold structure of the spectrum is essentially the same as for the case without electron-electron interaction described in the appendix B.3, and the location of the various single ionization thresholds is unaffected by the term $1/r_{12}$, since the electron interaction vanishes at large distances. Thus the N-th ionization thresholds are given by

$$I_N = -\frac{Z^2}{2(N-1/2)^2}, \quad N \geq 1 \text{ integer}, \tag{4.1}$$

a series which obviously converges to zero with $N \to \infty$.

Hence, the first series of eigenenergies converges to the threshold $I_1 = -8$ a.u., and above this energy all bound states with $N > 1$ are embedded into the continuum of lower series and therefore are resonance states with finite width [61].

Additionally, as described in chapter 2, the spectrum can be classified by the particle exchange symmetry, the symmetry Π_x with respect to the x-axis, and the absolute value of the angular momentum $|l|$. The energy levels for l and $-l$ ($l > 0$) are degenerate, what further implies the degeneracy of $\Pi_x = +1$ and $\Pi_x = -1$ for given $|l| > 0$. Indeed, if $|\Psi^+_{E,|l|}\rangle$ is a symmetric eigenstate of 2D helium with respect to Π_x, with eigenenergy E, then $|\Psi^+_{E,|l|}\rangle$ is a superposition of two degenerate eigenstates $|\psi_{E,l}\rangle$ and $|\psi_{E,-l}\rangle$ of 2D helium with angular momentum l and $-l$, respectively. Thus, up to normalization constants

$$|\Psi^+_{E,|l|}\rangle = |\psi_{E,l}\rangle + |\psi_{E,-l}\rangle. \tag{4.2}$$

Table 4.1: Singlet energy levels below the first ionization threshold for $|l| = 1$ and $\Pi_x = \pm 1$. Basis truncation $n_{\text{base}} = 250$ (see (3.10)). The total size of the basis is 84 320, for both $\Pi_x = -1$ and $\Pi_x = +1$. Optimal value of the scaling parameter: $\alpha = 0.40 \pm 0.02$.

$\Pi_x = +1$	$\Pi_x = -1$
-8.211 542 089 886	-8.211 542 089 886
-8.077 637 328 985	-8.077 637 328 985
-8.039 947 879 467	-8.039 947 879 467
-8.024 280 94	-8.024 280 94
-8.016 303 52	-8.016 303 52
-8.011 69	-8.011 69

From the anticommutation relation (2.29), it follows that $|\Psi^-_{E,|l|}\rangle = |\psi_{E,l}\rangle - |\psi_{E,-l}\rangle$ is an antisymmetric eigenstate of 2D helium with the same eigenenergy E. This degeneracy is corroborated in table 4.1, where singlet energy levels below the first ionization threshold for $|l| = 1$ are given.

In the absence of the electron-electron interaction, the zero angular momentum energy levels below the first ionization threshold are doubly degenerate (except for the ground state, which is not degenerate, as follows from (B.31) in appendix B.3), with one singlet state and one triplet state. Moreover, from (2.29) all these states have symmetry $\Pi_x = +1$.

In the 2D helium atom the interelectronic repulsion breaks this degeneracy as we can observe from the energy level structure in figure 4.1. The electron-electron interaction appears in the Hamiltonian (2.2) as γ/r_{12}, with $0 \leq \gamma \leq 1$. One can trace the energy levels as a function of γ, from the independent electron case ($\gamma = 0$) to the helium atom ($\gamma = 1$). The degenerate levels for $\gamma = 0$ split in two distinct levels for $\gamma > 0$, one singlet state and one triplet state, which both correspond to $\Pi_x = +1$ symmetry. This can be understood if we consider $\gamma = 0$: as explained in appendix B.3, the states of 2D helium without electron-electron interaction can be labeled by the principal quantum numbers N_1, N_2 ($N_i \geq 1$), and the angular momenta L_1, L_2 ($-N_i + 1 \leq L_i \leq N_i - 1$) of the electrons. Therefore zero angular momentum states are of the form $|N_1, N_2, L, -L\rangle$. Now, from (2.29) the states

$$|N_1, N_2, L, -L\rangle^{\epsilon_x} = |N_1, N_2, L, -L\rangle + \epsilon_x |N_1, N_2, -L, L\rangle, \quad \text{with } \epsilon_x = \pm 1, \tag{4.3}$$

are symmetric ($\epsilon_x = +1$) and antisymmetric ($\epsilon_x = -1$) with respect to Π_x.

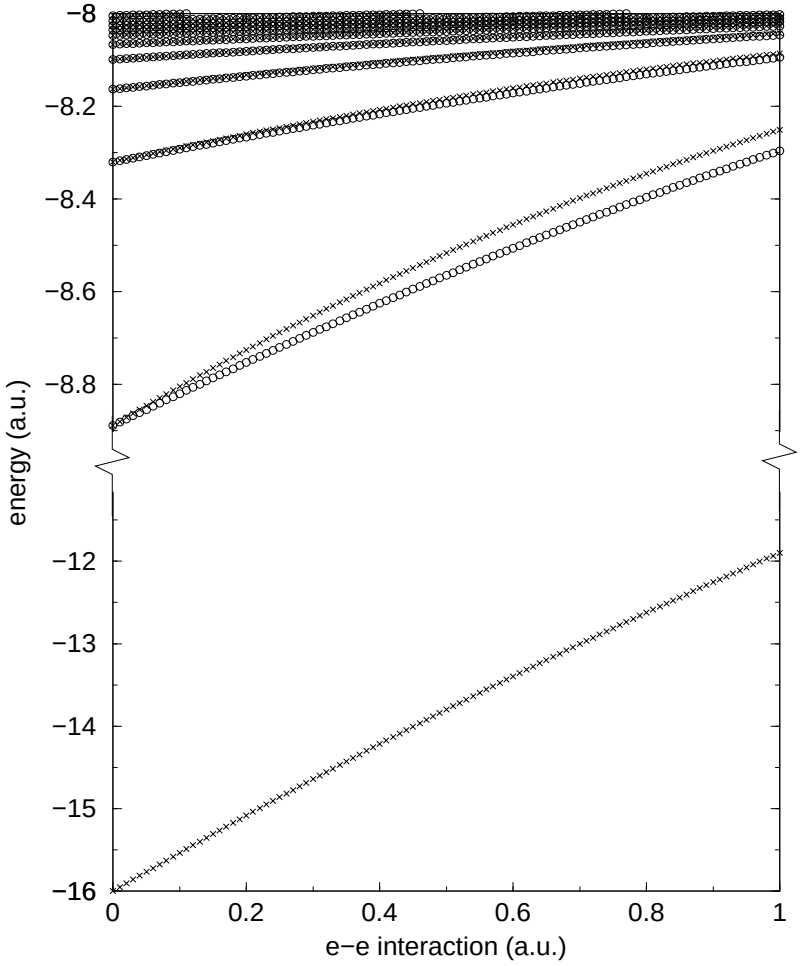

Figure 4.1: Level dynamics of the eigenenergies of (2.2), below the first ionization threshold $I_1 = -8.0\,\text{a.u.}$, as a function of the magnitude γ of the e-e interaction, for singlet (crosses) and triplet (circles) states with $|l| = 0$. As expected, with the exception of the ground state, all states are doubly degenerate for $\gamma = 0$.

Table 4.2: First four bound energy leves in atomic units below the second ionization threshold, for $\Pi_x = -1$ and $|l| = 0$. N and n label the excitation of the inner and of the outer electron, respectively. The truncation parameter was chosen as $n_{\text{base}} = 200$, and the optimal scaling parameter is $\alpha = 0.40 \pm 0.02$.

N	n	triplet states	singlet states
2	2	-1.273 641 219 559	
2	3	-0.984 664 061 020	-1.003 293 436 315
2	4	-0.934 882 211 552	-0.940 478 975 302
2	5	-0.915 916 000 683	-0.918 334 694 991
2	6	-0.906 668 776 66	-0.907 931 197 24

In particular, zero angular momentum states of the first series are $|1, N_2, 0, 0\rangle$ and $|N_2, 1, 0, 0\rangle$. Therefore, from (4.3), it follows that there are no $\Pi_x = -1$ eigenstates below the first ionization threshold. Since the electron-electron interaction does not break the Π_x symmetry, the latter result remains true for any value of γ. Furthermore, we have numerically verified that, for $|l| = 0$ and $\Pi_x = -1$, there are no bound states below I_1 and, a forteriori, no continuum states attached to this threshold. This implies that the lowest eigenenergies for this symmetry correspond to bound states. Indeed, all $\Pi_x = -1$, $|l| = 0$ eigenstates of 2D helium below the second ionization threshold are bound, and in table 4.2 we summarize the lowest energy levels of this series (see figure 4.4 for the level dynamics of the triplet $\Pi_x = -1$ ground state).

Table 4.3 collects the lowest energy levels below the first ionization threshold for singlet and triplet states. For each value of $|l|$ we obtain a Rydberg series converging to the first ionization threshold $I_1 = -8\,\text{a.u.}$ For such excited states the outer electron is dominantly localized far from the nucleus, while the inner electron essentially resides in its ground state. This behaviour can be confirmed by inspection of the probability distribution of such states. However, since the configuration space of 2D helium is four dimensional, it is not possible to provide a complete visualization in one plot. Therefore, we consider projections of the electronic density (2.62) in two dimensional subspaces of configuration space. For instance, in figure 4.2 the probability density of an excited singlet state with angular momentum $|l| = 1$ is shown. In (a), the projection on the x coordinates of the electrons for $y_1 = y_2 = 0$ is shown, which is localized around the point $x_1 = 33\,\text{a.u.}$ and $x_2 = 0.12\,\text{a.u.}$, as seen in (b), i.e., the inner electron sits close to the nucleus while the outer electron is very far. Moreover, from (c) the inner electron exhibits a perfectly

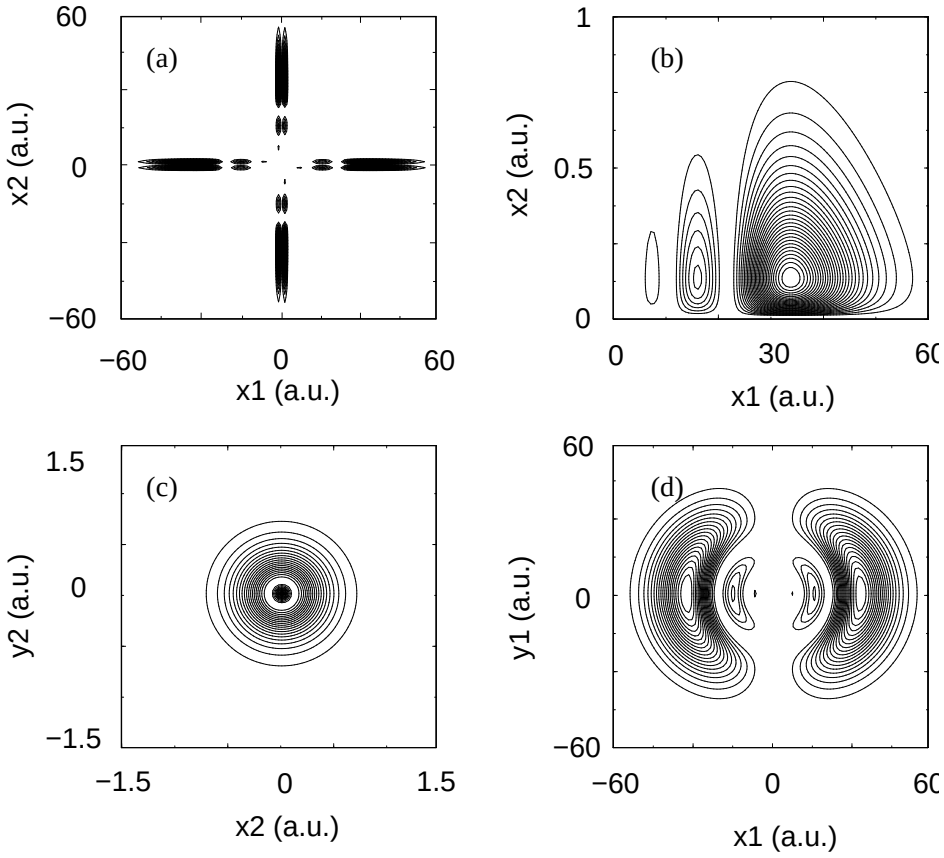

Figure 4.2: Probability density (2.62) of the $(N, n) = (1, 5)$ singlet state with angular momentum $|l| = 1$. The projection on the x coordinates of the electrons is shown in (a); A detail of this projection in (b) shows a maximum for $x_1 = 33\,\text{a.u.}$ and $x_2 = 0.12\,\text{a.u.}$; (c) displays the probability density of the inner electron when the outer electron is fixed at $x_1 = 33\,\text{a.u.}$, and (d) shows the probability density of the outer electron when the inner electron is fixed at $x_2 = 0.12\,\text{a.u.}$

Table 4.3: Helium energy leaves below the first ionization threshold, in atomic units, for $\Pi_x = +1$ and $|l| = 0, 1, 2$. N and n label the excitation of the inner and of the outer electron, respectively. The truncation parameter was chosen as $n_{\text{base}} = 250$, and the optimal scaling parameter is $\alpha = 0.40 \pm 0.02$.

N, n	$\|l\|$	Singlet states	Triplet states
1,1	0	-11.899 822 342 953	
1,2	0	-8.250 463 875 379	-8.295 963 728 090
1,3	0	-8.085 842 792 777	-8.094 583 618 582
1,4	0	-8.042 911 011 139	-8.045 941 305 571
1,5	0	-8.025 668 309 756	-8.027 055 169 374
1,6	0	-8.017 061 079 81	-8.017 807 434 60
1,7	0	-8.012 155 50	-8.012 602 197
1,8	0	-8.009 097 3	-8.009 385 5
1,2	1	-8.211 542 089 886	-8.225 772 173 259
1,3	1	-8.077 637 328 985	-8.080 919 691 737
1,4	1	-8.039 947 879 467	-8.041 165 882 92
1,5	1	-8.024 280 935	-8.024 858 501
1,6	1	-8.016 303 52	-8.016 621 18
1,7	1	-8.011 69	-8.011 89
1,3	2	-8.079 805 619 119	-8.079 819 688 304
1,4	2	-8.040 745 816 89	-8.040 751 693 482
1,5	2	-8.024 657 756 3	-8.024 661 159 15
1,6	2	-8.016 510 49	-8.016 512 44
1,7	2	-8.011 82	-8.011 82

symmetric probability distribution similar to the hydrogenic ground state in figure B.1.

Thus, the energy levels below the first ionization threshold can additionally be labeled by the principal quantum number n of the outer electron as if the electrons were non-interacting electrons. This picture can be also extended to $\Pi_x = -1$, $|l| = 0$ bound states and to moderately doubly excited states, where the quantum number N of the inner electron labels its Rydberg level as well as the single ionization thresholds.

As already described, above the first ionization threshold all states are embedded into the continuum of lower series. Therefore we use complex rotation for the numerical calculation of these states, and thus, also have to adjust the rotation angle, besides the scaling parameter α, in order to achieve optimal convergence. A typical spectrum of the rotated Hamiltonian of field free 2D

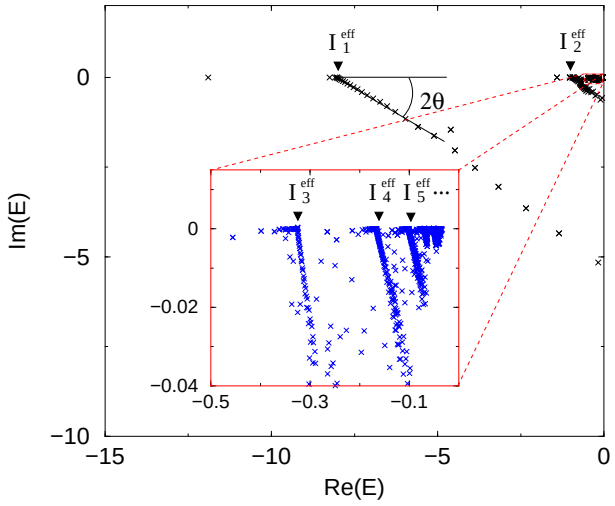

Figure 4.3: Complex energy spectrum of the rotated 2D helium Hamiltonian (2.2), for singlet states, $\Pi_x = +1$, and $|l| = 0$. The data were obtained by several runs of the Lanczos algorithm, choosing the shift parameter E_s (see (3.14)) close to the ionization thresholds I_N, $N = 1 \ldots 5$. Due to the truncation of the basis, $I_N^{\text{eff}} < I_N$ [65]. In all cases $\theta = 0.3$, whilst the parameters α and n_{base} have to be readjusted to obtain optimal convergence in the different spectral ranges. For the eigenvalues above the sixth ionization series, we used $n_{\text{base}} = 300$, what implies a basis size of 76 076.

Table 4.4: Degeneracy of the energy levels of the $N = 2$ Rydberg series in the non-interacting case ($\gamma = 0$), for $n = 2$, $n = 3$, and $|l| = 0, 1, 2, 3$, in the four symmetry subspaces of 2D helium (fourth to seventh columns): singlet and triplet, $\Pi_x = \pm 1$. The total degeneracy of the lowest energy level $E_{N=2,n=2}$ is 9, while for $n = 3$ the total degeneracy is 30 (s. app. B.3).

N	n	$\|l\|$	Singlet		Triplet		Total
			$\Pi_x = +1$	$\Pi_x = -1$	$\Pi_x = +1$	$\Pi_x = -1$	
2	2	0	2	-	-	1	3
2	2	1	1	1	1	1	4
2	2	2	1	1	-	-	2
2	3	0	2	1	2	1	6
2	3	1	3	3	3	3	12
2	3	2	2	2	2	2	8
2	3	3	1	1	1	1	4

helium atom is shown in figure 4.3, for singlet states with $\Pi_x = +1$ and zero angular momentum. One clearly observes how the continuum part of the spectrum is rotated by an angle close to 2θ into the lower half of the complex plane, and around the single ionization thresholds I_1, $I_2, \ldots,$ $I_5, \ldots$. Indeed, due to the truncation of the basis the exact thresholds cannot be reached, but only effective ionization thresholds I_N^{eff} [65,79]. The doubly excited states appear as isolated complex eigenvalues: the real part is the energy E of the resonance, and the imaginary part is equal to $-\Gamma/2$, with Γ the decay rate.

The first resonance of 2D helium is found for zero angular momentum and singlet exchange symmetry. The complex eigenvalue of this resonance state is

$$E = -1.411\,496\,328\,143 - i\,0.001\,241\,734\,389 \text{ a.u.}$$

It is obtained for the parameters $\theta \simeq 0.4$, $\alpha \simeq 0.35$, $n_{\text{base}} = 200$, and a basis size of 23426. For triplet exchange symmetry the lowest resonance is found for $|l| = 1$, and its energy and its decay rate are $E = -1.386138210196$ a.u. and $\Gamma/2 = 0.000056648625$ a.u., respectively.

The energy and decay-rate structure of singlet and triplet states for zero angular momentum below the second ionization threshold is illustrated in figure 4.4, for variable strength of the electron-electron interaction. For $\gamma = 0$, the levels correspond to the $N = 2$ Rydberg series, with $n \geq 2$, converging to the second ionization threshold ($I_2 = -8/9$). In that case the total degeneracy of the energy level $E_{N=2,n=2} = -16/9$ is 9, with three levels which correspond

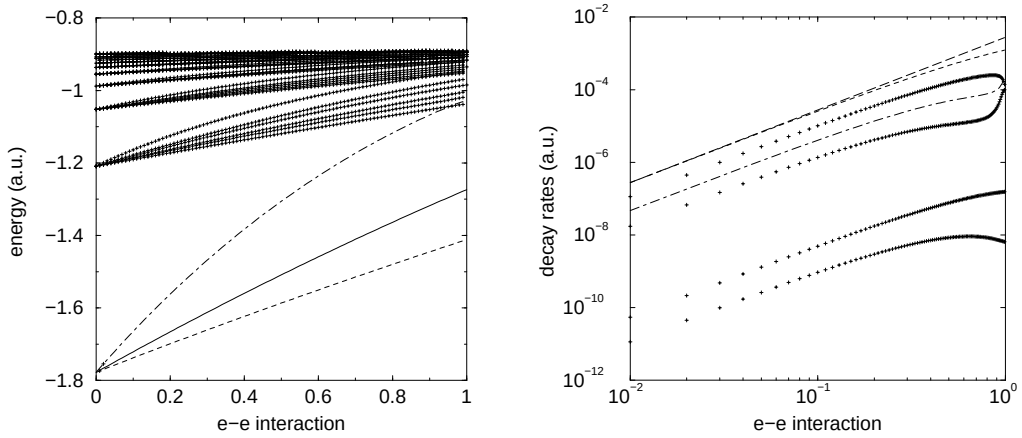

Figure 4.4: Energy levels (left) and decay rates (right) of the $|l| = 0$ states of the 2D helium atom between the first (-8 a.u.) and the second ($-0.888\ldots$ a.u.) ionization threshold, as a function of γ. The dashed line depicts the energy level (left) and the decay rate (right) dynamics of the first resonance state of the 2D He. The dash-dotted line corresponds to the singlet, $\Pi_x = +1$, $N = 2$, $n = 2$ resonance, while the solid line depicts the triplet, $\Pi_x = -1$, $N = 2$, $n = 2$ bound state. The long dashed line in the right panel indicates a fit $\sim \gamma^2$.

to $|l| = 0$. Indeed, since 2D helium without electron-electron interaction is equivalent to two coupled 2D hydrogen atoms, the degeneracy of the energy levels in this case can be easily calculated from the degeneracy of 2D hydrogen energy levels (s. app. B.3). In this particular case, the degeneracy of the 2D hydrogen energy level $E_{N=2}$ (or $E_{n=2}$) is 3 (s. app. B.2), with angular momentum $L_{1,2} = -1, 0, 1$ (the indices 1 and 2 label the electrons). Consequently, the total degeneracy of the energy level $E_{N=2,n=2}$ is 9. Furthermore, since the total angular momentum L_z is the sum of the angular momenta L_1 and L_2 of the electrons, the degeneracy of the zero angular momentum $E_{N=2,n=2}$ is three ($(L_1, L_2) = (0, 0)$, $(1, -1)$ and $(-1, 1)$). For $n = 3$ the total degeneracy is 30 (s. app. B.3), 6 of them with zero angular momentum (3 triplet and 3 singlet states, as shown in table 4.4).

In the case of the $N = 3$ Rydberg series the total degeneracy of the lowest energy level $E_{N=3,n=3} = -16/25$ is 25, and only 5 of them correspond to $|l| = 0$: 3 singlet states with $\Pi_x = +1$ and 2 triplet states with $\Pi_x = -1$. For $n = 3$ the total degeneracy is 70. For $|l| = 0$ there are each 3 singlet and triplet states with $\Pi_x = +1$, and each 2 singlet and triplet states with

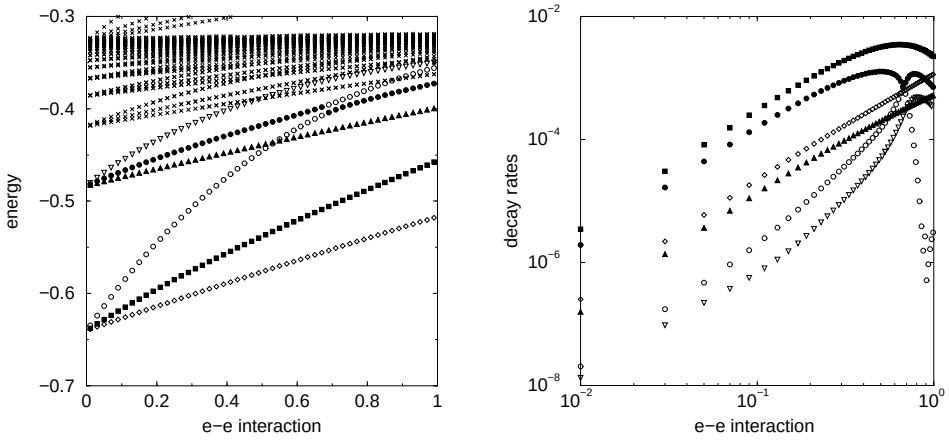

Figure 4.5: Energy (left) and decay-rate (right) dynamics of the $|l| = 0$, $\Pi_x = +1$ singlet resonances of 2D He between the second ($I_2 = -0.888\ldots$ a.u.) and the third ($I_3 = 0.32\ldots$ a.u.) ionization threshold. One of the $N = 3, n = 3$ states ($\circ$) and one of the $N = 3, n = 4$ states ($\bullet$) exhibit an isolated avoided crossing of their energies at $\gamma \simeq 0.67$, whilst their decay rates (right) cross precisely at the same value.

$\Pi_x = -1$, i.e. the degeneracy in this case is 10.

These simple considerations for the lowest excited states of the first few Rydberg series already impressively illustrate the dramatic enhancement of the density of states as we increase the electronic excitation. This is already manifest for the second Rydberg series shown in figure 4.5, where the level and decay rate dynamics between the second and the third ionization threshold for singlet states with $\Pi_x = +1$ and $|l| = 0$ is depicted. The situation complicates rapidly, as illustrated in figures 4.6 and 4.7, where level and decay rate dynamics close to the 4th ($I_4 = -8/49$ a.u.) and between the 4th and the 5th ionization threshold ($I_5 = 8/81$ a.u.) are shown.

In all cases, in the perturbative regime of small values of the parameter γ we observe a linear behaviour of the energy levels, while the decay rates grow proportional to γ^2, in agreement with perturbation theory for degenerate states [39]. This behaviour prevails for the lowest lying resonances, over a large range of γ. However, for higher excitations, different resonances start to interact, and deviations from the perturbative regime are observed.

Closer inspection of the spectral structure in the regime of highly doubly excited states shows that the level dynamics is governed by avoided crossings [87–89] which stem from the coupling induced by the e-e interaction. As an

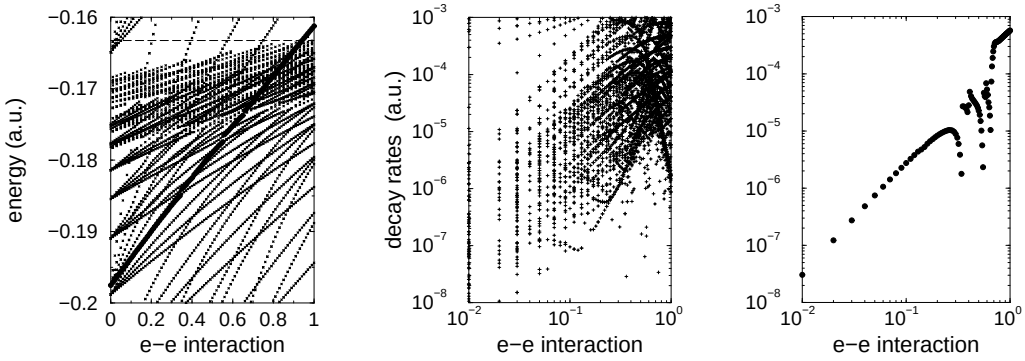

Figure 4.6: Energies (left) and decay rates (center and right) of the resonances of 2D He, for singlet exchange symmetry, $\Pi_x = +1$, and $|l| = 0$, close to the 4th ionization threshold ($I_4 = -8/49$ a.u.), as a function of γ. The lowest resonance (•) of the 5th Rydberg series exhibits several avoided crossings before crossing the 4th ionization threshold (indicated by the long dashed line), with associated dramatic enhancements of its decay rate at the crossings (note the logarithmic scale of the middle and right plot!).

example, an avoided crossing between two resonances is illustrated in figure 4.5 for singlet exchange symmetry, $\Pi_x = +1$, and $|l| = 0$. With increasing γ, the state which emanates from the $N = 3,\ n = 3$ multiplet at $\gamma = 0$ ($E = 0.64$ a.u.) with large energy (open circles) encounters the adiabatic continuation (filled circles) of one of the states emerging from the $N = 3$, $n = 4$ multiplet, at $\gamma \simeq 0.67$. Here, at an isolated avoided crossing, both states exchange their character, and it is the *diabatic* rather than the adiabatic continuation of the $N = 3,\ n = 3$ state (i.e., the adiabatic continuation of the $N = 3,\ n = 4$ state) which, for $\gamma > 0.67$ beyond the avoided crossing, has the largest overlap (indicated by open circles) with its origin at $\gamma = 0$. Furthermore, we observe in the right plot of Fig. 4.5 that, right at the avoided crossing of the energies at $\gamma \simeq 0.67$, the decay rates of these anticrossing resonances are precisely equal (they cross). For larger values of γ (e.g. $\gamma = 0.9$), avoided crossings with higher lying resonance states occur.

Increasing the excitation energy not only provokes the interaction of resonances, but, in addition, the overlap of different Rydberg series. For instance, in the non-interacting case overlapping Rydberg series can be observed starting at $N = 3$. Such overlap will again enhance the density of states, and thus multiply the incidences of resonance interaction. The left plot in figure 4.6 shows the level dynamics of the lowest resonance of the

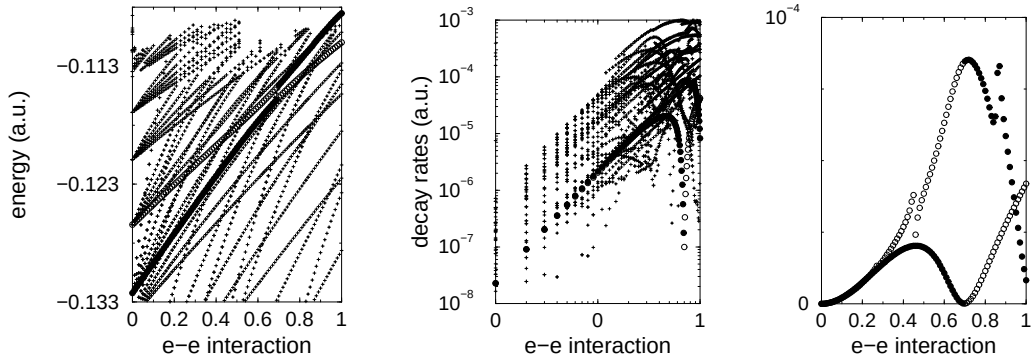

Figure 4.7: Energy (left) and decay rate (center and right) of the lowest resonance $N = 6, n = 6$ (•) of the 6th Ryberg series for singlet exchange symmetry, $\Pi_x = +1$, and $|l| = 0$. This resonance exhibits a clear avoided crossing with one of the $N = 4, n = 9$ resonances (∘). In the right panel the dynamics of the decay rates of these two interacting states is shown on a linear scale.

5th Rydberg series, hightlighted by full circles (•). At $\gamma = 0$, the level has energy $E_{N=5,n=5} = -(16/81)$ a.u., below the 4th ionization threshold $I_4 = -(8/49)$ a.u. – hence, the 4th and the 5th Rydberg series overlap. Alike our strategy described above, we identify the diabatic continuation of $E_{N=5,n=5}$ by its maximal overlap with the original eigenstate at $\gamma = 0$, leading to the the sequence of energy levels marked by •. As we can see, before evolving into the lowest resonance of the 5th series of 2D He ($\gamma = 1$), the continuation of the $N = 5$, $n = 5$, $\gamma = 0$ state exhibits several avoided crossings, due to the high density of states close to the ionization threshold. Finally it *crosses* the 4th ionization threshold at I_4 and only then settles into the corresponding He state.

The situation for the lowest resonance of the 6th series is a little bit different, as illustrated in figure 4.7. In this case the resonance starts at the energy level $E_{N=6,n=6} = -(16/121)$ a.u.$= -0.1322$ a.u. which is far below the next ionization threshold at $I_5 = -(8/81)$ a.u.$=-0.0988$ a.u. In this energy range the number of interacting states is reduced, and the state exhibits a prominent avoided crossing before it settles into the corresponding 2D He state. The interaction at $\gamma \simeq 0.7$ with one of the $N = 4$, $n = 9$ resonances, marked with open circles (∘), dramatically suppresses its decay rate (right plot) to values close to zero (9×10^{-8} a.u.). This behaviour is strongly reminiscent of a quasibound state in the continuum [90].

In table 4.5 we show the converged energy levels and decay rates of the lowest doubly excited states, up to the 7th Rydberg series. All these resonances are found for singlet exchange symmetry, $\Pi_x = +1$, and $|l| = 0$. We see that the lowest resonance of the 6th series lies below the 5th ionization threshold I_5. Hence, the 5th Rydberg series overlaps with the 6th series of the 2D helium atom. Similarly, the 6th and the 7th series overlap, and so forth. Thus, starting at the 5th series, all series mix.

In figure 4.8, the two-electron probability densities of the lowest states of the series $N = 2$ and 4 are shown, while the electronic density of the $N = n = 6$ state is shown in 4.9. If we inspect the probability density projected on the x axis (upper plots in Figs. 4.8 and 4.9), the electrons tend to occupy opposite sides of the nucleus, at equidistant positions. This conjecture might appear incompatible with the bottom plots in these figures, where the projection of the probability density on perpendicular axes is shown. However, the maximum of the functions in the upper plots is at least one order of magnitude bigger than in the lower plots. Moreover, the ratio of these maxima increases with N.

Furthermore, these figures suggest also that the structure of the wave functions is preserved as $N = n$ is increased, with the exception of the resonance $N = 6, n = 6$: in figure 4.9 (a) and (c), one only hardly recognizes the dominant structure of the less excited states in figure 4.8, in the central part of the plots (note the larger scale as compared to figure 4.8). The latter are zoomed in in panels (b) and (d) of the figure. We attribute this difference to the overlap of the 5th series with the 6th series, what destroys the rather simple structure observed in the nonoverlapping case, as a consequence of the interaction with other resonances, as illustrated in figure 4.7.

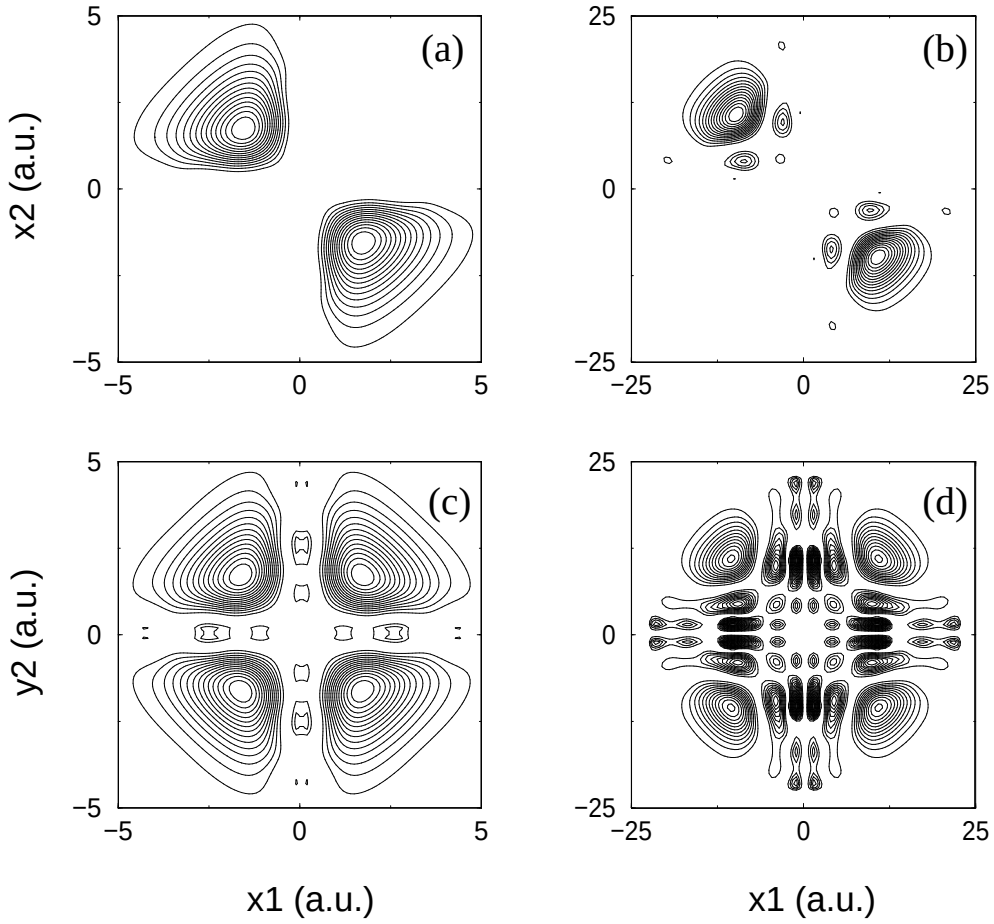

Figure 4.8: Probability density of the eigenstates $N = n$ of the Rydberg series of 2D He, for $n = 2$ ((a) and (c)), and $n = 4$ ((b) and (d)). In (a) and (b) the conditional probability densities along the x direction ($y_1 = y_2 = 0$) are shown, while (c) and (d) depict the probability densities as function of x_1 and y_2, for $x_2 = y_1 = 0$. [Note that the tiny apparent asymmetry of the electronic density with respect to the $x_1 = 0$ and $y_2 = 0$ axes in (c) and (d) is an artifact of the graphics software.]

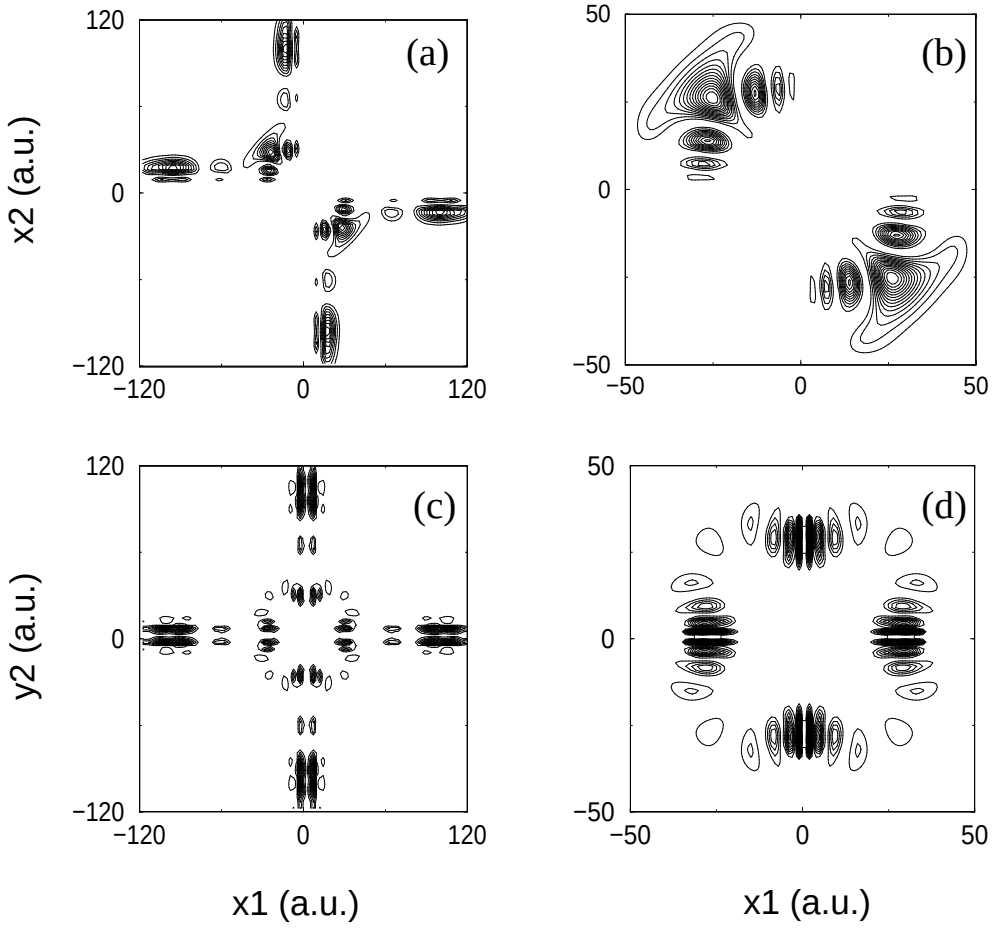

Figure 4.9: Probability density of the lowest energy level $N = n = 6$ of the 6th series. In (a) and (b) the conditional probability density along the x direction is shown ((b) is a detail close to the center of (a)), while (c) and (d) depict the probability density as function of x_1 and y_2, for $x_2 = y_1 = 0$ ((d) zooms into the center of (c)). [As in Fig. 4.8, the apparent asymmetry of the densities in (c) and (d) with respect to the $x_1 = 0$ and $y_2 = 0$ axes is an artifact of the graphics software.]

Table 4.5: Lowest energy levels and decay rates of doubly excited states, found for zero angular momentum, singlet exchange symmetry, and $\Pi_x = +1$, up to the 7th series. For the higher excitations we used $n_{\text{base}} = 300$, with a basis size 76076. The relatively poor convergence of the 5th state is due to its interaction with the rotated continuum emanating from the I_4 threshold.

N, n	I_N	Energy(a.u.)	$\Gamma/2$ (a.u.)
2,2	-0.88889	-1.411 496 328 143	-0.001 241 734 389
3,3	-0.32000	-0.516 872 103 407	-0.001 165 786 319
4,4	-0.16327	-0.265 531 275 47	-0.000 774 567 15
5,5	-0.09877	-0.161 223 759	-0.000 572 27
6,6	-0.06612	-0.108 510 920 110	-0.000 008 262 814
7,7	-0.04734	-0.077 577 461 413	-0.000 044 363 709

Chapter 5

The frozen planet configuration

In the present chapter, we concentrate on the quantum aspects of a special classical configuration of the field free three body Coulomb problem – the *frozen planet configuration* (FPC) first described by Richter and Wintgen, at the beginning of the last decade [16]. We start this chapter with an introduction on the most relevant (semi)classical issues concerning this configuration, before turning to the quantum treatment and to specific results on the frozen planet states in 2D He.

5.1 Introduction

In the FPC both electrons are located on the same side of the nucleus, with asymmetric excitation. On the first glance, this highly asymmetric structure might appear to be unstable. However, classical studies [5, 16, 91, 92] show that, indeed, it is *dynamically stable*: while the inner electron follows highly eccentric elliptic trajectories which precess around the symmetry axis of the configuration, the outer electron is localized around some equilibrium distance far from the inner electron. It is dynamically stabilized due to the fast oscillation of the latter, which implies a rapidly oscillating potential experienced by the outer electron, due to the competition between electron-electron repulsion and the Coulomb attraction exerted on the outer electron by the screened Coulomb potential of the nucleus. Upon averaging [93] over the characteristic time scale of the inner electron's motion, the outer electron experiences an effective, time-independent, weakly attractive potential what determines the equilibrium distance [94].

The classical dynamics of the FPC is governed by the Hamiltonian (2.2) of

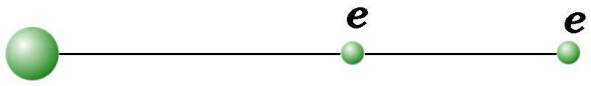

Figure 5.1: Collinear frozen planet configuration of He [16]: The three particles of the atom lie on the same line, and both of the electrons are located on the same side of the nucleus.

the helium atom. As already described in chapter 2, the classical dynamics generated by (2.2) is invariant under the scaling transformations

$$\begin{array}{lcll} H_0 & \mapsto & \lambda^{-1} H_0, & \\ \boldsymbol{r}_i & \mapsto & \lambda \boldsymbol{r}_i, & (i=1,2), \\ \boldsymbol{p}_i & \mapsto & \lambda^{-1/2} \boldsymbol{p}_i, & (i=1,2), \\ t & \mapsto & \lambda^{3/2} t, & \end{array} \tag{5.1}$$

where λ is an arbitrary positive real number. Thus, for bound configurations, i.e. configurations with negative total energy, it is sufficient to restrict to the manifold with total energy $E = -1$. An additional external, linearly polarized driving field interaction (s. eq. (2.4)) will not destroy this scale invariance. In that case, the scaled field amplitude and frequency read

$$\begin{array}{lcl} F & \mapsto & \lambda^{-2} F, \\ \omega & \mapsto & \lambda^{-3/2} \omega, \end{array} \tag{5.2}$$

respectively. Restricted to the collinear unperturbed FPC (Fig. 5.1), the classical dynamics is regular as evident from the Poincaré surface of section in figure 5.2 [5, 91, 92], [1] where position and momentum of the outer electron are represented by a point each time when the inner electron collides with the nucleus. Thus, the phase space of the collinear FPC contains a large region of bound motion.

The effective potential seen, as already mentioned above, by the outer electron, is attractive Coulombic for large distances, and strongly repulsive for positions close to the nucleus, with a minimum which precisely defines the equilibrium position of the FPC. From this potential one can read off intrinsic frequency and amplitude scales which completely determine the effect of an external driving field on the configuration [19, 95]. Due to the invariance

[1] The figure 5.2 was extracted from reference [92].

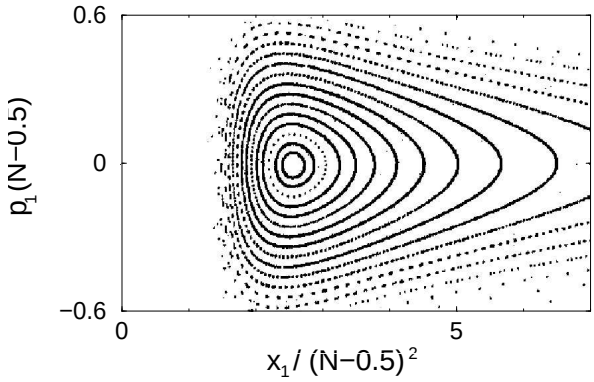

Figure 5.2: Poincaré surface of section of the collinear frozen planet configuration. The scaled position $x_1/(N-0.5)^2$ and momentum $p_1(N-0.5)^2$ of the outer electron are plotted whenever the inner electron collides with the nucleus. $N-1/2$ is the effective quantum number of the inner electron in 2D He, see (B.13).

of the Hamiltonian under the scaling transformations (5.1) and (5.2), the intrinsic quantities depend only [19] on the action integral $\oint p_2 dx_2$ over one cycle of the Kepler oscillation of the inner electron, where x_2 and p_2 are its position and momentum. Since this action integral is an invariant in the framework of adiabatic approximations, the position $x_{\min}$ of the minimum of the effective potential (i.e., the equilibrium position of the outer electron), the minimum energy $E_{\min}$, the intrinsic frequency scale ω_I, and the intrinsic field strength F_I for the FPC, in atomic units are,

$$\begin{aligned} x_{\min} &= 2.6\, S^2, \\ E_{\min} &= -2.22\, S^{-2}, \\ \omega_I &= 0.3\, S^{-3}, \\ F_I &= 0.03\, S^{-4}, \end{aligned} \tag{5.3}$$

where

$$S = \frac{1}{2\pi} \oint p_2\, dx_2.$$

The natural scale F_I for the field strength is given by the maximum slope of the effective potential, and defines the minimum static field necessary to ionize the configuration. The frequency scale ω_I is given by the curvature of the potential at its minimum, this is the frequency of small oscillations around the equilibrium position.

In a quantum description, the action S is replaced by the effective quantum number of the inner electron, which in the 1D and 3D case is N, while in the 2D case is $N - 1/2$, due to the additional term $1/2$ in the denominator of the expression (B.13) for the eigenenergies of 2D hydrogen atoms. Thus, the scaled quantities (5.3) take the form

$$x_{\min} = 2.6\,(N-0.5)^2, \tag{5.4}$$
$$E_N = -2.22\,(N-0.5)^{-2}, \tag{5.5}$$
$$\omega_I = 0.3\,(N-0.5)^{-3}, \tag{5.6}$$
$$F_I = 0.03\,(N-0.5)^{-4}. \tag{5.7}$$

Due to the large phase space volume occupied by the stability region of the FPC, it is possible to identify eigenstates in the spectrum which are localized along the frozen planet orbit, even for relatively weak excitations. Indeed, calculations on 3D [17] and 1D [19] helium demonstrate the existence of such configurations for quantum numbers $N \geq 3$ of the inner electron. As we will see, also in 2D He such *frozen planet states* (FPS) exist. In all these cases, for each N, the FPS form a Rydberg series characterized by the long life time of its constituents. Thus, the FPC are well-defined configurations of the classical three body Coulomb problem, with unambiguous quantum correspondence.

In contrast to the available theoretical results, FPS have so far not been unambiguously identified in experiments, though sequential multiphoton excitation schemes [96–98] have successfully been used for the creation of planetary states [99], i.e. helium like atoms where both electrons are highly excited and move in different regions of space ($\langle \boldsymbol{r}_2 \rangle < \langle \boldsymbol{r}_1 \rangle$).

5.2 Identification of frozen planet states in 2D He

In chapter 4 we gave a description of the spectrum of 2D He. As we have seen there, increasing the excitation of the electrons the density of states increases dramatically. Now we shall extract specific quantum states localized along classical frozen planet trajectories from typical spectra of the rotated Hamiltonian (Fig 5.3). Since these states are localized along a collinear configuration, the expectation value of the cosine of the angle θ_{12} between the electron radii $\boldsymbol{r}_1$ and $\boldsymbol{r}_2$ has to be close to unity ($\langle \cos\theta_{12} \rangle \simeq 1$). However, this quantity alone does not fully characterize the FPS. A complete picture

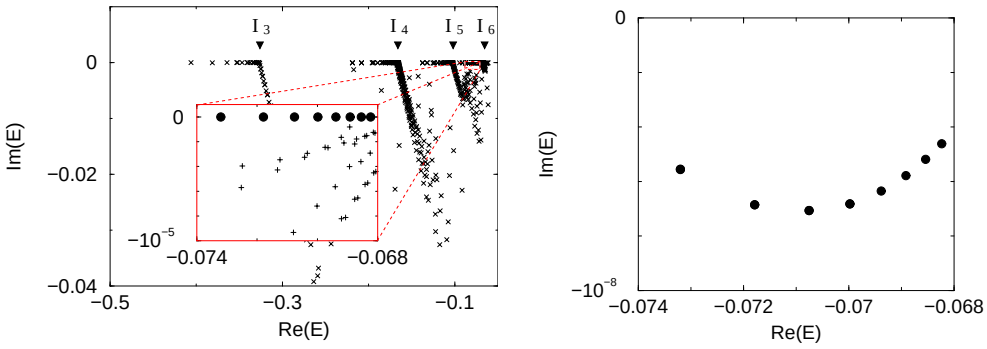

Figure 5.3: Triplet spectrum of the rotated Hamiltonian up to the sixth ionization threshold: Frozen planet states (filled circles - ● - in the inset on the left, and on the right) build a Rydberg series, typically characterized by small decay rates.

is only provided by the wave function itself, and a direct comparison of the electronic density with the phase space of the FPC will give detailed insight in the localization properties of the FPS. Thus, in the following we will characterize the FPS by $\langle \cos\theta_{12} \rangle$, as well as by their electronic densities in configuration space and in phase space.

The formal expression for $\langle \cos\theta_{12} \rangle$ in terms of the eigenvalues and eigenvectors of the rotated Hamiltonian can be obtained similarly as the derivation of the expression (2.61) for the probability density. However, the numerical implementation is not that straightforward. Likewise, the phase space of 2D helium has eight dimensions, and a phase space representation will therefore necessitate a projection on a suitable subspace. Here we will chose the submanifold spanned by the collinear configuration. Hence, the identification and visualization of the FPS in the spectrum of the rotated Hamiltonian is not trivial, and the rest of this section is devoted to an outline of the technical machinery which is necessary to accomplish this task.

5.2.1 Expectation value of $\cos\theta_{12}$

We notice that, in Cartesian coordinates,

$$\langle E|\cos\theta_{12}|E\rangle = \int d^4r \langle \boldsymbol{r}|E\rangle\langle E|\boldsymbol{r}\rangle \cos\theta_{12}. \tag{5.8}$$

Thus, transforming to parabolic coordinates we have

$$\langle E|\cos\theta_{12}|E\rangle = \int d^4r_p \langle \boldsymbol{r}_p|E\rangle\langle E|\boldsymbol{r}_p\rangle B\cos\theta_{12}, \tag{5.9}$$

where $\boldsymbol{r}_p$ denotes the set of parabolic coordinates (x_p, y_p, x_m, y_m) and B is the Jacobian (2.11) of the transformation. With the help of the projector (2.52) on the resonant state $|E\rangle$ we obtain that

$$\langle E|\cos\theta_{12}|E\rangle = -\frac{1}{\pi}\mathrm{Im}\sum_j \frac{\langle\overline{E_{j\theta}}|B\cos\theta_{12}|E_{j\theta}\rangle}{E_{j\theta}-E}. \tag{5.10}$$

If we proceed with the single pole approximation (which is well justified here, see figure 5.3), as in equation (2.62), we obtain

$$\langle E|\cos\theta_{12}|E\rangle \simeq \frac{1}{\pi|\mathrm{Im}E_{j\theta}|}\mathrm{Re}\,\langle\overline{E_{j\theta}}|B\cos\theta_{12}|E_{j\theta}\rangle. \tag{5.11}$$

The expression of $\cos\theta_{12}$ in terms of the the distances from the nucleus to the electrons r_1 and r_2 and of the interelectronic distance r_{12} reads

$$\cos\theta_{12} = -\frac{r_{12}^2 - r_1^2 - r_2^2}{2r_1r_2}. \tag{5.12}$$

Thus, from (2.10), $B\cos\theta_{12} = -8r_{12}(r_{12}^2 - r_1^2 - r_2^2)$ is a polynomial function of the parabolic coordinates, and can therefore be expressed precisely in the same way as described in section 2.3.2 in terms of the circular operators (2.18). The explicit expression together with its matrix elements has been calculated analytically, once again by symbolic calculus. In total, the expression of $B\cos\theta_{12}$ has 2088 monomial terms in $a_1,\ a_2,\ a_3,\ a_4$ and their adjoint operators, with 171 selection rules in the Fock basis (2.21).

As an illustration, let us again consider the lowest resonances $N = n$ of the Rydberg series described at the end of chapter 4. In table 5.1 we show the calculated values of $\langle\cos\theta_{12}\rangle$ for these states. As N increases, $\langle\cos\theta_{12}\rangle$ progressively tends towards the value -1, what is perfectly consistent with our discussion of their localization properties illustrated in figure 4.8: as N increases, the electrons are always better localized on opposite sides of the nucleus.

5.2.2 Husimi distributions

The Husimi function $Q_\psi(q,p)$ of a quantum state $|\psi\rangle$ is defined as the diagonal element of the associated density matrix with respect to harmonic

Table 5.1: Expectation value of $\cos\theta_{12}$, for the lowest states of subsequent series, $2 \leq N = n \leq 7$. $\langle\cos\theta_{12}\rangle$ decreases monotonously to -1 with increasing electronic excitation, fully consistent with our discussion of the electronic density in figure 4.8.

N, n	Energy(a.u.)	$\langle\cos\theta_{12}\rangle$
2,2	-1.411 496 328 143	-0.64
3,3	-0.516 872 103 407	-0.76
4,4	-0.265 531 275 47	-0.82
5,5	-0.161 223 759	-0.86
6,6	-0.108 510 920 110	-0.88
7,7	-0.077 577 461 413	-0.90

oscillator coherent states $|z\rangle$ with squeezing parameter ω_s (which is nothing but the harmonic oscillator frequency),

$$W_\psi(q,p) = |\langle z|\psi\rangle|^2. \tag{5.13}$$

The coherent state $|z\rangle$ is a minimum uncertainty Gaussian wave packet with coordinate representation

$$\langle r|z\rangle = \exp\left(-\frac{1}{2}\omega_s(r-q)^2 - irp\right), \tag{5.14}$$

centered at the point (p,q) in the phase space [100] (with appropriate scaling according to $z = (\sqrt{\omega_s}q + ip/\sqrt{\omega_s})/\sqrt{2}$).

However, for the study of the FPC this definition has to be amended [19,92]. Let us assume that x_1 and p_1 (x_2 and p_2) are the position and the momentum of the outer (inner) electron in the collinear FPC. Then, for each point (x_1, p_1) of the Poincaré surface of section shown in figure 5.2: $x_2 = 0$ and $p_2 = 0$. Hence, in order to compare the 2D FPS with the classical phase space of the collinear FPC, we first have to project the 2D FPS onto the (x, p_x) subspace, and then to calculate its overlap with the Gaussian wave packets in (x_1, p_{x_1}) space, whilst imposing $x_2 \simeq 0$. For this purpose, equation (5.14) has to be multiplied by $\delta(y_1)\delta(x_2 - x_2^0)\delta(y_2)$, where x_2^0 is close to zero (though not precisely zero, since the wave function vanishes in the coordinate origin). We finally obtain for the modified coherent state

$$\phi_{q,p}(x_1,y_1,x_2,y_2) = \exp\left(-\frac{1}{2}\omega_s(x_1-q)^2 - ix_1p\right)\delta(y_1)\delta(x_2-x_2^0)\delta(y_2), \tag{5.15}$$

where we choose $\omega_s = \omega_I = 0.3(N-1/2)^{-3}$, i.e., the intrinsic frequency of the FPC, as squeezing parameter.

The projected Husimi function of an energy eigenstate $|E\rangle$ is given by

$$\begin{aligned} W_\psi(q,p) &= |\langle\phi_{q,p}|E\rangle|^2 \\ &= \int d\boldsymbol{r}d\boldsymbol{r}'\phi^*_{q,p}(\boldsymbol{r})\phi_{q,p}(\boldsymbol{r}')\langle\boldsymbol{r}|E\rangle\langle E|\boldsymbol{r}'\rangle, \end{aligned} \tag{5.16}$$

and equation (2.52), together with the single resonance approximation, leads to the final result

$$W_\psi(q,p) \simeq \frac{1}{\pi|\mathrm{Im}\, E_{j\theta}|}\mathrm{Re}\int d\boldsymbol{r}\phi_{q,p}(\boldsymbol{r})\langle\boldsymbol{r}|R(-\theta)|E_{j\theta}\rangle\int d\boldsymbol{r}'\phi^*_{q,p}(\boldsymbol{r}')\langle\boldsymbol{r}'|R(-\theta)|E_{j\theta}\rangle. \tag{5.17}$$

5.3 Frozen planet states of 2D He

5.3.1 Energies and decay rates

Starting from the third series of the 2D helium spectrum we have identified quantum states which are localized on the FPC. These FPS are organized in subseries converging to the single ionization thresholds, and typically exhibit small decay rates (Fig. 5.3), as compared to other eigenstates. Therefore, each FPS can be labeled by the excitation of the inner electron N and by a quantum number n_F which refers to the position of the specific FPS in the associated subseries converging to I_N.

In table 5.2 we summarize the energies and decay rates of the lowest ($n_F = 1$) singlet (^1S) and triplet (^3S) FPS of the subseries converging to the Nth ionization threshold for $N = 3, 4, \ldots, 14$. The table gives the converged results of the quantum calculations. The energy values in the fourth column of this table are the energies of the classical configuration obtained from equation (5.5).

As can be seen from table 5.2, the simple classical adiabatic energy gives a good approximation of the fundamental FPS energies, which progressively improves as N is increased, i.e. in the semiclassical limit. Of course, the classical energy estimates neglects particle exchange effects, though the energy splitting due to the electron exchange symmetry decreases exponentially with N, as clearly spelled out by figure 5.4.

Table 5.2: Energies of the singlet (^1S) and triplet (^3S) FPS in the fundamental state $n_F = 1$. E_N is the energy of the classical configuration obtained from (5.5). As N increases, the exact quantum result progressively converges towards the classical expectation.

N	$E^{(2D)}(^1S)$	$E^{(2D)}(^3S)$	E_N	$(\Gamma/2)^{(2D)}(^1S)$	$(\Gamma/2)^{(2D)}(^3S)$
3	−0.354 907 546	−0.352 128 586	−0.35520	0.000 003 372	0.000 001 529
4	−0.180 560 506	−0.180 360 429	−0.18122	0.000 000 877	0.000 000 418
5	−0.109 297 550	−0.109 260 500	−0.10963	0.000 003 748	0.000 000 021
6	−0.073 207 046	−0.073 203 013	−0.07339	0.000 010 180	0.000 000 005
7	−0.052 445 661	−0.052 443 726	−0.05254	0.000 001 443	0.000 000 129
8	−0.039 408 949	−0.039 408 949	−0.03947	0.000 000 317	0.000 000 31
9	−0.030 693 094	−0.030 693 093	−0.03073	0.000 000 158	0.000 000 390
10	−0.024 578 744	−0.024 578 820	−0.02460	0.000 000 087	0.000 000 037
11	−0.020 125 003	−0.020 125 045	−0.02014	0.000 000 105	0.000 000 016
12	−0.016 780 71	−0.016 780 695	−0.01679	0.000 000 03	0.000 000 007
13	−0.014 205 703	−0.014 205 698	−0.01421	0.000 000 006	0.000 000 003
14	−0.012 180 962	−0.012 180 961	−0.01218	0.000 000 002	0.000 000 001

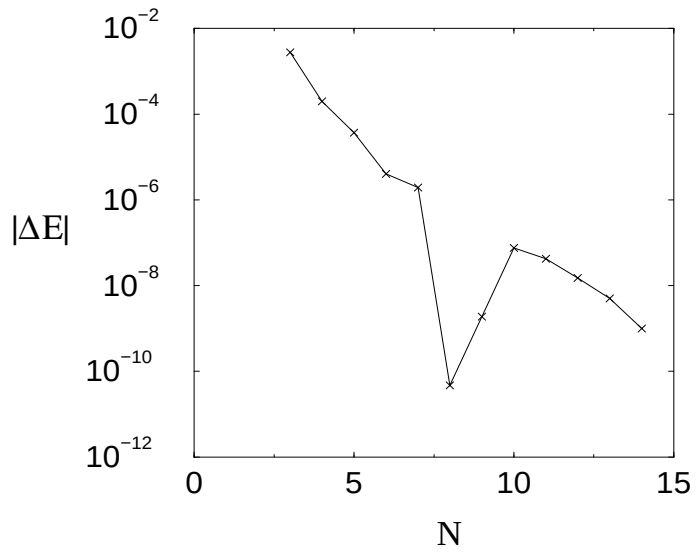

Figure 5.4: Absolute energy splitting between the lowest singlet and triplet states of the FPS series N. Clearly, ΔE decreases exponentially as N is increased, i.e. in the semiclassical limit.

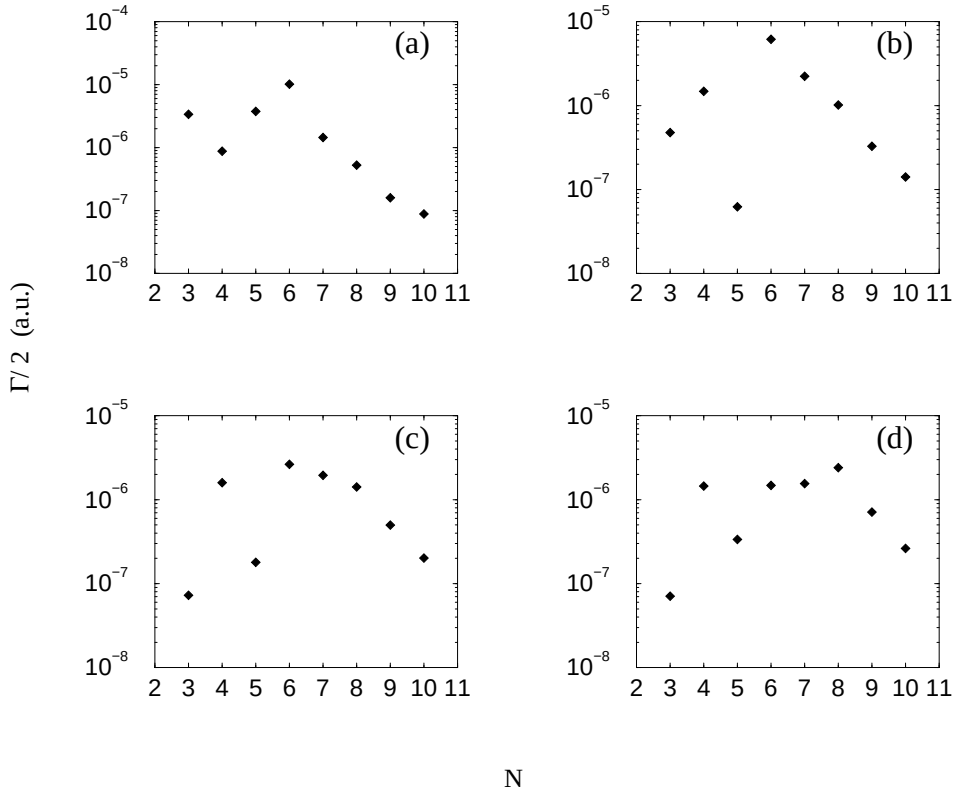

Figure 5.5: Ionization rates Γ of the four lowest frozen planet states $n_F = 1 - 4$ (a - d) of the Nth series. Whilst the rates exhibit some fluctuations for $N \leq 6$, they tend to exhibit a smooth exponential decay for $N \geq 6$, in agreement with a semiclassical interpretation as tunneling decay from the frozen planet island shown in figure 5.2. As the excitation within the island increases (with n_F), clear exponential decay can only be observed for larger values of N ($N \geq 8$ in (c) and (d)), due to the finite extension of the wave function as compared to the size of the island (see also figures 5.11 and 5.12).

Table 5.3: Decay rates of the 1D [19], 2D and 3D [17] frozen planet states below the 10th ionization threshold.

N	$\Gamma^{(1D)}/2$	$(\Gamma^{(3D)}/2)(^1S)$	$(\Gamma^{(3D)}/2)(^3S)$	$(\Gamma^{(2D)}/2)(^1S)$	$(\Gamma^{(2D)}/2)(^3S)$
3	$1.4 \cdot 10^{-12}$	$1.1 \cdot 10^{-5}$	$6.8 \cdot 10^{-6}$	$3.4 \cdot 10^{-6}$	$1.5 \cdot 10^{-6}$
4	$4.4 \cdot 10^{-12}$	$1.2 \cdot 10^{-5}$	$4.4 \cdot 10^{-6}$	$8.8 \cdot 10^{-7}$	$4.2 \cdot 10^{-7}$
5	$2.5 \cdot 10^{-12}$	$2.0 \cdot 10^{-6}$	$1.8 \cdot 10^{-7}$	$3.7 \cdot 10^{-6}$	$2.1 \cdot 10^{-8}$
6	$1.0 \cdot 10^{-13}$	$5.6 \cdot 10^{-7}$	$3.3 \cdot 10^{-8}$	$1.0 \cdot 10^{-5}$	$5.6 \cdot 10^{-9}$
7	$3.9 \cdot 10^{-13}$	$2.0 \cdot 10^{-7}$	$3.8 \cdot 10^{-7}$	$1.3 \cdot 10^{-7}$	$1.3 \cdot 10^{-7}$
8	$1.5 \cdot 10^{-13}$	$3.7 \cdot 10^{-7}$	$1.4 \cdot 10^{-7}$	$5.3 \cdot 10^{-7}$	$3.2 \cdot 10^{-7}$
9	$6.4 \cdot 10^{-14}$	$1.2 \cdot 10^{-6}$	$2.2 \cdot 10^{-8}$	$1.6 \cdot 10^{-7}$	$3.9 \cdot 10^{-8}$
10	$2.8 \cdot 10^{-14}$	$5.3 \cdot 10^{-7}$	$3.5 \cdot 10^{-8}$	$8.7 \cdot 10^{-8}$	$3.7 \cdot 10^{-8}$

Also the decay rates of the FPS decrease exponentially with the excitation, as observed in table 5.3 and in figure 5.5(a), where the ionization rates $\Gamma/2$ of the singlet states of table 5.2 up to $N = 10$ are given. Much as for the above splitting ΔE, this exponential decay can be interpreted semiclassically in terms of dynamical tunneling [101,102] between different phase space regions. The tunneling decay from a classical phase space region associated with an FPS, with probability

$$P(E) \sim e^{-\alpha S/\hbar}, \tag{5.18}$$

is determined by some tunneling action S which only depends on the classical dynamics [45]. From the scale invariance (5.1), with scaling parameter $\lambda = -E_N$, the scaled action is defined through $S = S^{\mathrm{sc}}/\sqrt{-E_N}$. Thus, from equation (5.5) the semiclassical widths decrease exponentially with N.

A direct comparison of the decay rates of 1D [92], 3D [17] FPS (s. table 5.3) shows that the frozen planet, when restricted to one single dimension of configuration space, exhibits autoionization rates which are several orders of magnitude *smaller* than those of the real 3D atom. This contrasts a wide spread argument [103, 104], according to which 1D models should exhibit enhanced autoionization rates as compared to the actual 3D problem, since in the 1D case no space is left for the electrons to avoid the detrimental Coulomb singularity of the electron-electron interaction term in (2.2). On the basis of simulations of the 3D classical dynamics the authors of the 1D calculation in [19] therefore conjectured that, once again, the origin of this counterintuitive effect is caused by the dynamical stabilization mechanism sketched above: only not too large transverse deviations from the ideal collinear case maintain the stability – the region of classical stability has a finite extension in the

Table 5.4: Expectation value of $\cos\theta_{12}$ for the lowest FPS of the singlet series of 3D and 2D helium. Note that $\langle\cos\theta_{12}\rangle$ is systematically larger in the 2D case, consistent with the restriction of the dynamics to the plane.

N	$E^{(2D)}(^1S)$	$\langle\cos\theta_{12}\rangle^{(2D)}$	$E^{(3D)}(^1S)$	$\langle\cos\theta_{12}\rangle^{(3D)}$
3	−0.354 907 546	0.672	−0.257 371	0.351
4	−0.180 560 506	0.787	−0.141 064	0.534
5	−0.109 297 550	0.772	−0.089 570	0.712
6	−0.073 207 046	0.950	−0.062 053	0.747
7	−0.052 445 661	0.888	−0.045 538	0.776
8	−0.039 408 949	0.905	−0.034 842	0.802
9	−0.030 693 094	0.914	−0.027 517	0.817
10	−0.024 578 744	0.921	−0.022 284	0.848
11	−0.020 125 003	0.929	−0.018 411	0.866
12	−0.016 780 71	0.935	−0.015 468	0.876
13	−0.014 205 703	0.939	−0.013 178	0.885
14	−0.012 180 962	0.944	−0.011 361	0.893
15	−0.010 560 175	0.947	−0.009 896	0.900

phase space component spanned by the transverse dimension.

If this argument holds true, already the frozen planet configurations of planar helium should exhibit enhanced autoionization rates as compared to the 1D case, as indeed can be seen from table 5.3. Furthermore, the decay rates of the 2D FPS are not only significantly enhanced with respect to the 1D case, but, equally important, exhibit comparable values as obtained in the 3D case.

Finally, table 5.4 collects the expectation values of $\cos\theta_{12}$ for the singlet 2D and 3D [17] frozen planet states for $n_F = 1$ and $N = 3, 4, \ldots, 15$. In both cases $\langle\cos\theta_{12}\rangle$ increases monotonously, with some exceptions in the 2D case (which we attribute to avoided crossings alike the ones discussed in chapter 4), and in all cases the 2D expectation value is larger than the 3D one, which only emphasizes the restriction to the plane, where transverse deviations in only two directions from the collinear configuration are allowed.

5.3.2 Wave functions

The precise localization properties of the FPS emerge from the study of their wave functions. However, since the configuration space of 2D He is four

dimensional, it is not possible to provide a complete visualization in one single plot. In the following, besides the Husimi functions already described, we will consider two alternative projections of the electronic density (2.62) in configuration space:

- *Conditional probability distributions for a given angle* θ_{12}: from the rotational invariance of the helium atom, the probability distributions depend only on the relative position of the electrons, i.e., for a given angle θ_{12}, the wave function depends only on the radii r_1 and r_2 (as also numerically verified – for instance, see figure 5.6 (c) and (d)). Therefore it is always possible to choose r_1 to be the Cartesian coordinate x_1, what automatically determines r_2. In particular, for $\theta_{12} = 0$ the conditional probability is obtained from the general electronic density (2.62) by substituting $r_1 = x_1$ and $r_2 = x_2$, with $x_1 \geq 0$, $x_2 \geq 0$, and $y_1 = y_2 = 0$.

- *One-electron probability densities:* The wave functions of the 2D helium states contain the correlated information on both electrons. Nevertheless, we can impose some condition on one electron, to obtain the *conditional probability density* for the other. For the one-electron wave functions presented here we fix one of the electrons at some point $(x_1^{(0)}, y_1^{(0)})$, and thus the conditional probability density of the other electron obtained from equation (2.62) is given by

$$|\psi(x_2, y_2 | x_1 = x_1^{(0)}, y_1 = y_1^{(0)})|^2 = |\psi(x_1^{(0)}, y_1^{(0)}, x_2, y_2)|^2 \qquad (5.19)$$

Figure 5.6 shows the probability density of the lowest FPS of the 6th triplet series. (a) depicts the conditional probability density of the two-electron state, as a function of the distances r_1 and r_2 of the electrons from the nucleus, for $\theta_{12} = 0$. The maximum of the function in this plot lies at the point ($r_1 \simeq 78\,\text{a.u.}, r_2 \simeq 23\,\text{a.u.}$), i.e., one electron is close to the nucleus, while the other is far, and thus we can address the electrons as the inner and outer one, respectively. This justifies our above labeling of the outer electron by subindex 1 and of the inner electron by 2. Thus, e.g., the position of the outer electron is given by the coordinates (x_1, y_1), and its distance to the nucleus is r_1, and analogously for the inner electron.

For the inner electron fixed at $r_2 = 23\,\text{a.u.}$, the probability density for the outer electron is illustrated in figure 5.6 (b). We observe that this electron is well localized at 78 a.u. from the nucleus. On the other hand, fixing the external electron at 78 a.u. from the nucleus the resulting probability density for the second electron is given in (c) and (d). In (c), the position of the outer electron in atomic units is ($x_1 = 78\,\text{a.u.}$, $y_1 = 0$), while in

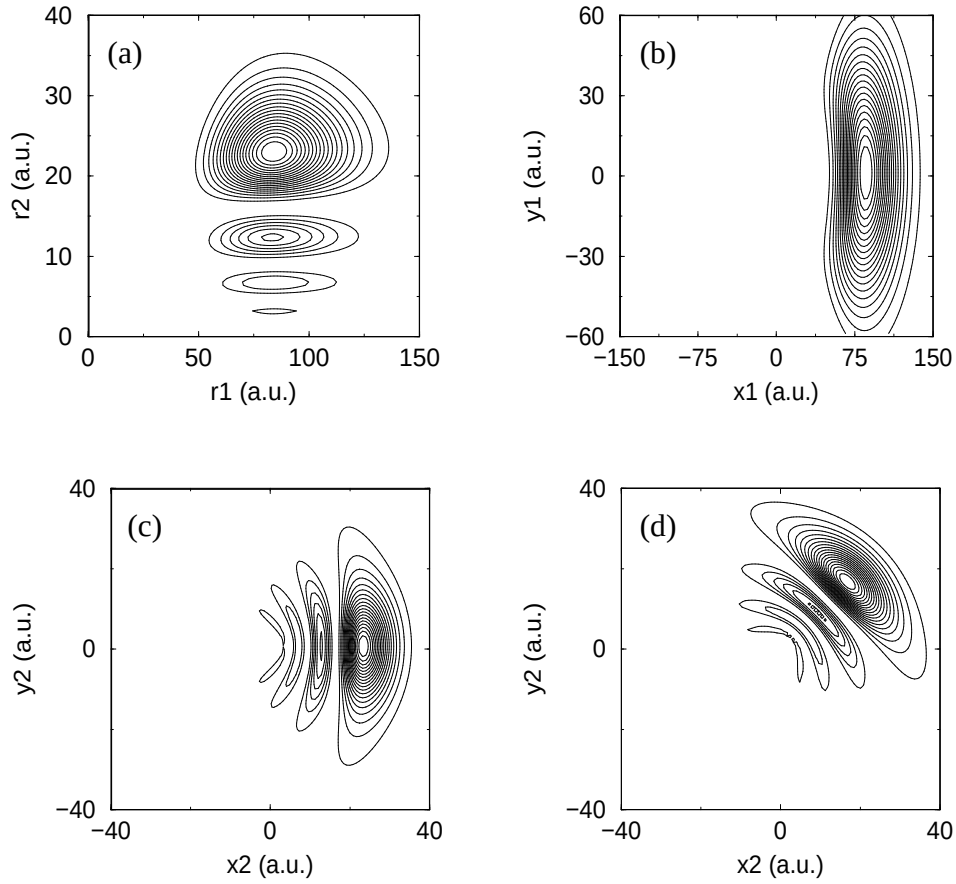

Figure 5.6: Contour plots of the electronic density of the $N = 6$, $n_F = 1$ triplet 2D FPS. The two-electron density (a) for $\theta_{12} = 0$ shows the electrons localized at different distances from the nucleus. Whilst the inner electron (c,d) is localized along a highly eccentric Kepler ellipse (the nucleus sits in the origin), the outer electron (b) is "frozen" at the minimum of the effective potential dynamically created by the interplay between the electron-electron interaction term in (2.2), and the rapid Kepler motion of the inner electron along its strongly polarized trajectory [96, 105]. (c) and (d) additionally illustrate the rotational invariance of the electronic density.

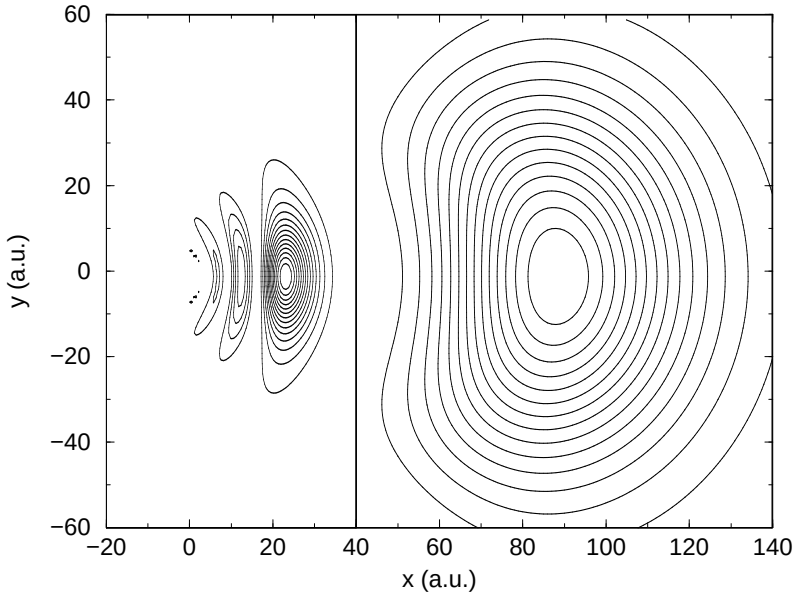

Figure 5.7: Contour plot of the electronic density of the planar frozen planet state of the $N = 6$ series, in 2D configuration space. The left part is the probability distribution for the inner electron at fixed radial distance r_1 of the outer electron, as in figure 5.6(c); the right part shows the density of the outer electron at fixed inner electron radius r_2 (as in figure 5.6(b)).

(d) ($x_1 = (78\cos 45°)$ a.u., $y_1 = (78\sin 45°)$ a.u.). As we can see, (d) is simply obtained from (c) by a rotation by 45° in configuration space, what corroborates the rotational invariance of our numerical solutions.

Furthermore, the position of the minimum (5.5) of the classical effective potential for $N = 6$ is $x_{\min} \simeq 78.65$, which corresponds to the location of the outer electron of the corresponding quantum state. Additionally, the electronic densities of the inner and of the outer electron are localized in completely different regions of the real 2D space, as illustrated in figure 5.7.

The electronic density of the excited triplet states of this series is shown in figure 5.8. These states exhibit the same general behaviour as the $n_F = 1$ state. In particular, the electrons are localized at different regions of space. The maximum in the radial direction of the inner electron remains invariant for all these excited states, which shows that the excitation of the inner electron (i.e. the quantum number N) remains the same. On the other hand, the density of the outer electron peaks at different radial distances,

and this distance increases with n_F. Thus, n_F is a quantum number that labels the excitation of the outer electron. This is, additionally, reflected in the nodal structure of the wave functions.

The behaviour described here for the FPS $N = 6$ series of FPS is also observed for all other FPS series which we investigated, for both, singlet and triple symmetries. For instance, figure 5.9 depicts the probability densities for the first and second singlet FPS of the 15th series. In addition, zooming into the nodal structure of the wave functions in this plot shows that there are 14 nodes in the radial wave function of the inner electron, in agreement with the general expectation of $N - 1$ nodes [17].

The mapping of the FPS wave functions on the classical FPC phase space can be directly probed with the projective Husimi distributions described in section 5.2.2. Figure 5.10 shows the projected Husimi distributions of the first three FPS of the sixth triplet series and the Poincaré surface of section of the FPC. The localization of the frozen planet states is apparent in these plots: while the fundamental state of the series is well localized on the regular frozen planet periodic orbit at the minimum of the effective potential at 2.6 scaled units, excited states trace frozen planet trajectories which are well identified by the position of the outer turning point at the maximum of the Husimi function.

In the figure 5.11 we compare the Husimi functions of the singlet (left) and triplet (right) states of the 6th series. Though in both cases the quantum states are localized along periodic orbits of the frozen planet configuration, the $n_F = 2$ and $n_F = 3$ singlet states exhibit pronounced maxima at the outer turning point of the trajectory, while in triplet states the electronic density in the outer an inner turning points are of the same order of magnitude. We attribute this effect to Pauli exclusion principle: in singlet states, besides the Coulomb repulsion, the particles are identical, and thus both electrons tend to be as separated as possible.

In section 5.3.1, we already mentioned that, increasing the excitation N of the inner electron, also the expectation value of $\cos\theta_{12}$ increases (Tab. 5.4). This basically means that highly excited FPS are better confined along the collinear configuration. This trend is very clearly exposed by the localization properties of the corresponding Husimi distributions in figure 5.12, where the Husimi functions of the $N = 3 - 7$ and $N = 15$ singlet FPS for $n_F = 1$ are shown.

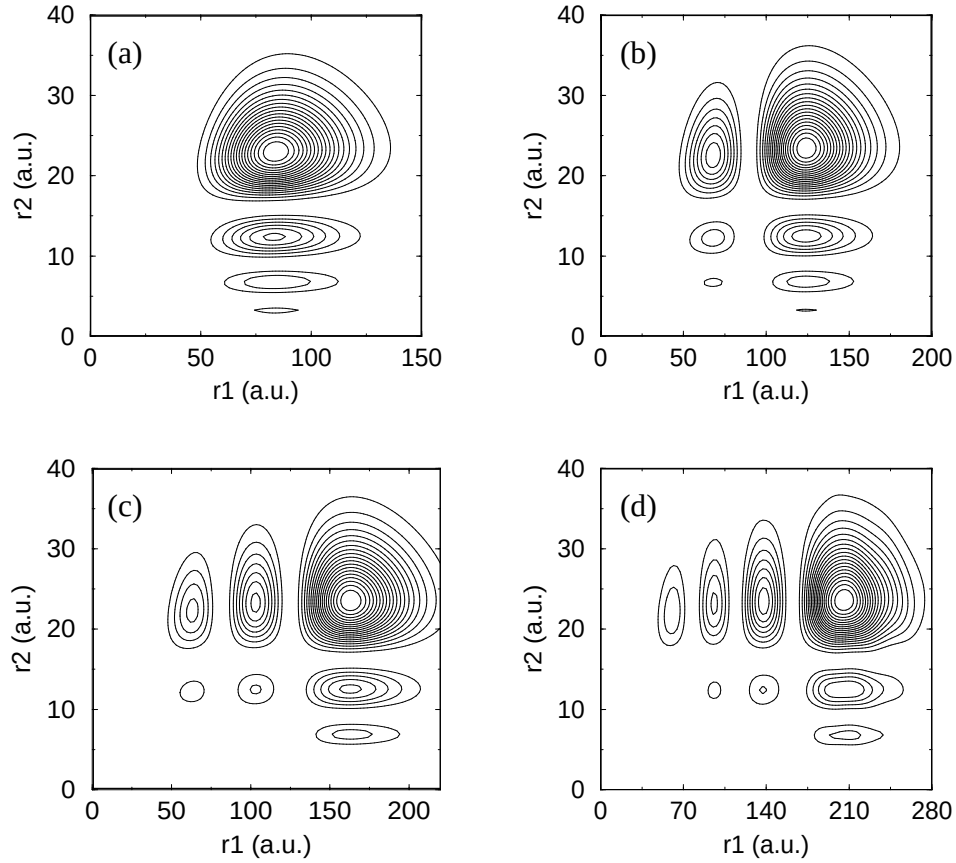

Figure 5.8: Conditional probability densities for $\theta_{12} = 0$ of the first four triplet FPS of the sixth series: (a) $n_F = 1$; (b) $n_F = 2$; (c) $n_F = 3$; (d) $n_F = 4$. The maximum of the electronic densities in the radial distance r_2 of the inner electron is invariant, while the position of the outer electron increases with n_F. The number of nodes in the radial distance r_1 of the outer is precisely $n_F - 1$.

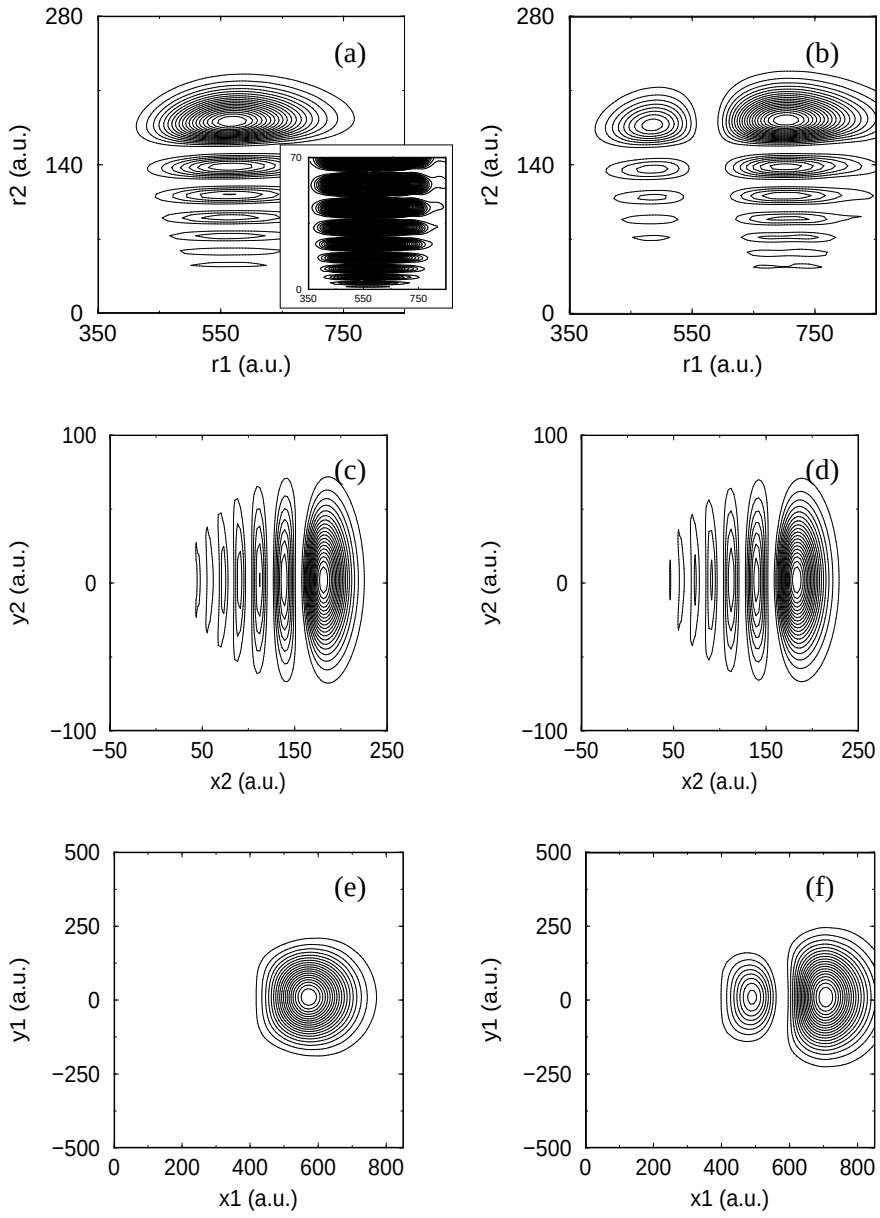

Figure 5.9: Electronic densities of the $n_F = 1$ (left) and $n_F = 2$ (right) FPS of the 15th singlet series. In (a) and (b) the two-electron probability density for $\theta_{12} = 0$ is shown. (c) and (d) show the electronic density of the inner electron, for the outer localized close to the maximum of (a) and (b) ($r_1 = 560\,\text{a.u.}$ in (c) and $r_1 = 700\,\text{a.u.}$ in (d)), respectively. In (e) and (f), the electronic density of the outer electron is plotted for $r_2 = 179\,\text{a.u.}$. The outer electron is perfectly localized, in its ground as well as in its excited state. The inset in (a) shows the nodal structure of the wave function in detail. In total there are 14 nodes, as expected.

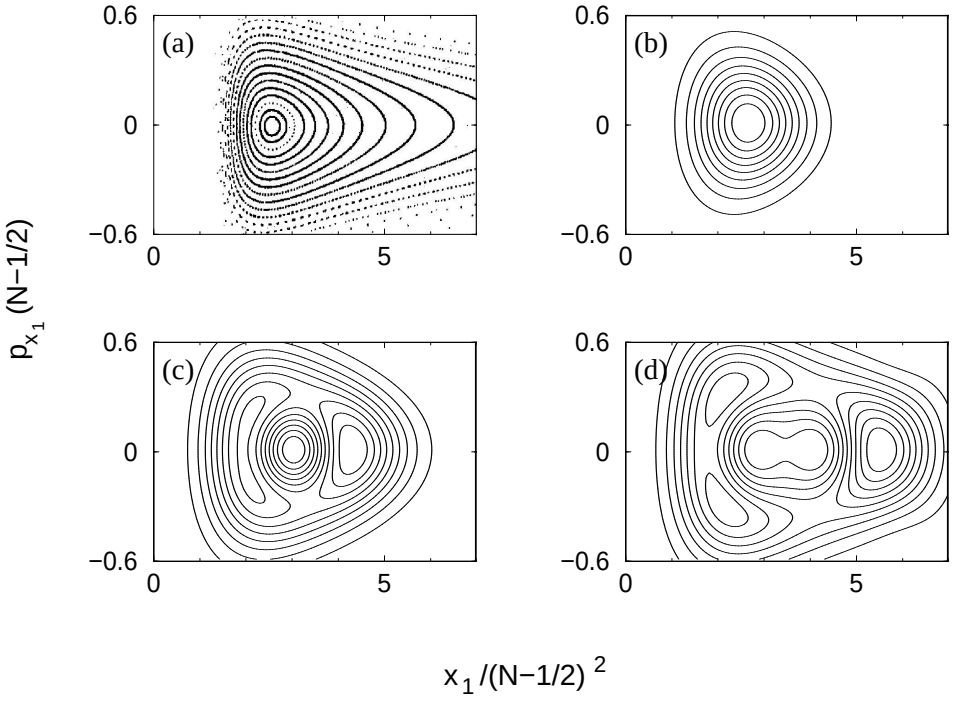

Figure 5.10: Contour plots of the Husimi distributions of the $n_F = 1$ (b), $n_F = 2$ (c) and $n_F = 3$ (d) triplet FPS of the sixth series, compared with the classical phase space of the collinear FPC in (a) [16, 92]. The Husimi functions show perfect phase space localization: while the fundamental state (a) is localized at the minimum of the effective potential at 2.6 scaled units, the excited states are localized along frozen planet trajectories with higher energy, with outer turning points (at the maximum of the distribution) at 4.2 (c) and 5.5 (d) scaled units.

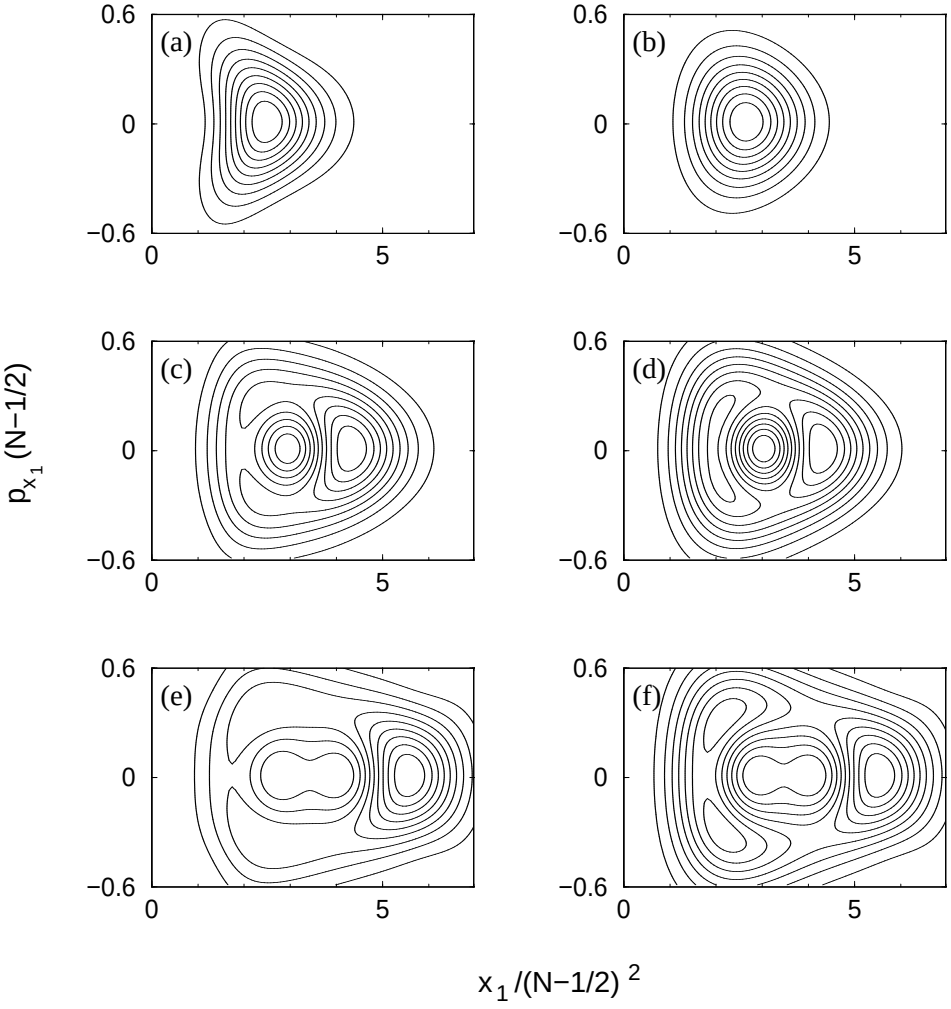

Figure 5.11: Contour plots of the Husimi distributions (5.17) of the lowest three singlet (left) and triplet (right) FPS of the 6th series.

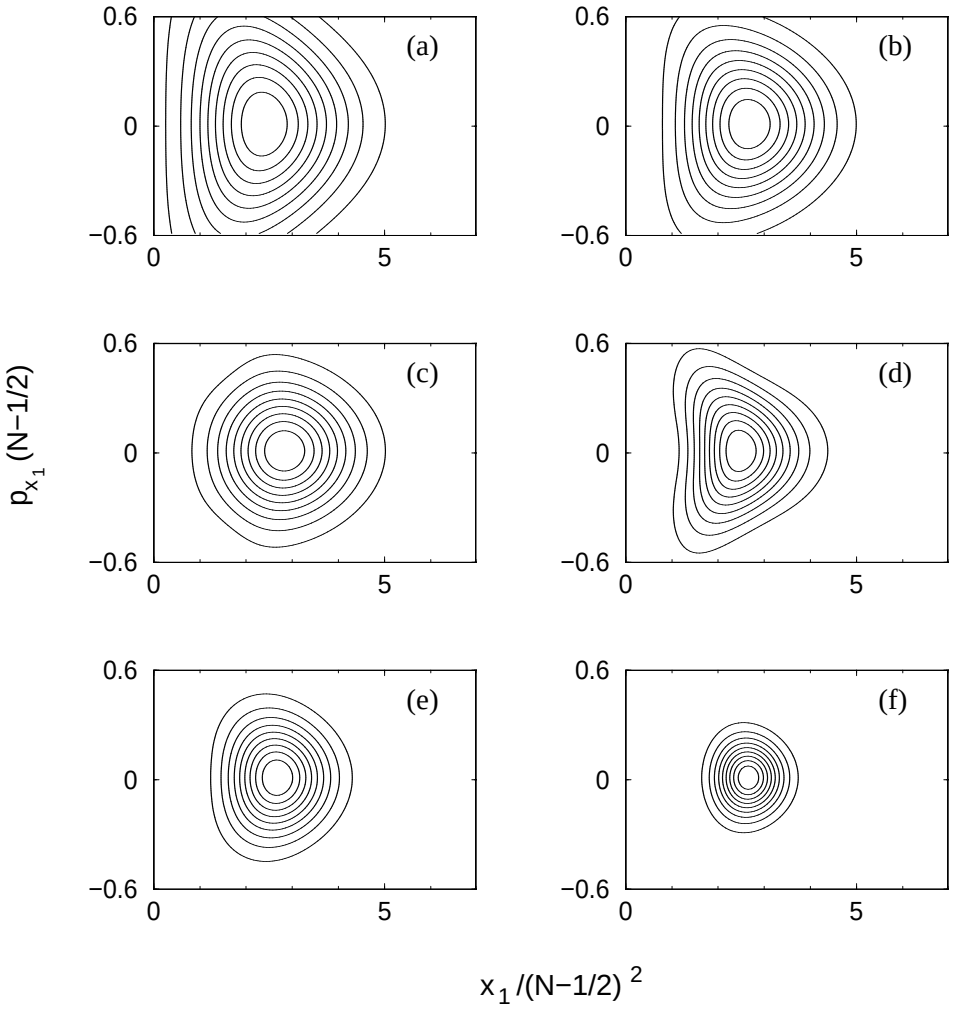

Figure 5.12: Contour plots of the Husimi functions of the fundamental (singlet) FPS of the $N = 3 - 7$ (a-e) and of the $N = 15$ (e) series. As the excitation is increased, the states are better and better localized along the frozen planet trajectory.

Chapter 6

Nondispersive wave packets in 2D Helium

Apart from its independent interest for the field free, autonomous helium problem already studied in the previous chapters, the frozen planet configuration is of potentially high relevance in the context of coherent control [106–108] in the electronic dynamics of Rydberg systems in the presence of electron-electron interactions [109]: During the last decade, it has been realized that near-resonant electromagnetic driving of atomic electrons in one-electron Rydberg systems allows to create *nondispersive electronic wave packets* [66, 110, 111] (in a quantum system with a *non-harmonic* spectrum!) which propagate along Kepler trajectories of essentially arbitrary eccentricity and orientation for very long times [18, 66, 112]. This field has by now been investigated theoretically in much detail and is well understood, and first experimental realizations of such long living "quantum particles" have been reported very recently [20]. An immediate question is of course whether such a localization and stabilization effect is also to be expected in Rydberg systems with additional electron-electron interaction, e.g., in helium. Since the unperturbed frozen planet configuration has a well defined associated eigenfrequency (5.6), the external field can be tuned such as to drive that frequency near resonantly, and, as a matter of fact, it already was shown that nondispersive two-electron wave packets which propagate along the frozen planet trajectory *do exist* in a one dimensional model of helium [19].

Now, the purpose of the present chapter is to investigate the localization properties of FPS under the influence of a near-resonant external driving field in more than one dimension, which until now has been an unaccessible regime of driven helium, simply due to the mere size of the corresponding

Floquet eigenvalue problem, brought about by the field induced coupling of many angular momentum states. Though, before coming to our results in section 6.3, we review very briefly the most important aspects of the classical driven frozen planet in the next section. Section 6.2 is then devoted to the technical details of the visualization of the electronic density of driven helium in phase space.

6.1 The classical helium atom under periodic driving

In section 5.1 we already reviewed the most relevant aspects of the unperturbed classical FPC. Here, we consider the driven case, when the field frequency is chosen near-resonant with the frequency (5.6) of the periodic orbit.

In the simplest case, as shown in [95], it is still possible to find classically stable configurations of the driven collinear frozen planet, which manifest as regular resonance islands in the mixed regular-chaotic associated phase space of the collinear model. However, a complete visualization of this five-dimensional space (spanned by the positions and momenta of the electrons, and by the phase ωt of the driving field) in two dimensions is not possible. Nevertheless, the separation of time scales of the inner and the outer electron's motion, for near resonant driving frequencies and moderate values of the field amplitude, allows to map the phase space structure onto a two dimensional surface, by a two-step Poincaré section method [92, 95]: In a first step, a simple Poincaré section is obtained by plotting the position x_1 and the momentum p_1 of the outer electron whenever the inner electron reaches the nucleus, which eliminates the fast Kepler oscillations. The resulting points are connected (by cubic interpolation) to constitute an effective trajectory, which allows to construct a stroboscopic section for fixed phase $\phi_0 = \omega t$.

Figure 6.1 [19] depicts the two-step Poincaré surface of section obtained for field frequency $\omega = 0.2(N - 0.5)^{-3}$a.u., field amplitude $F = 0.005(N - 0.5)^{-3}$ a.u., and field phases $\omega t = 0$ (left); $\omega t = \pi/2$ (center); $\omega t = \pi/2$ (right). Besides the intrinsic regular region centered around the equilibrium position of the configuration, that is also present in the unperturbed case (s. Fig. 5.2) and basically comes from the e-e interaction, there is an additional regular island immerged in the chaotic see, stemming from the resonant driving by the field, as a consequence of the Kolmogorov-Arnold-Moser theorem [93, 113]. The principal difference between the intrinsic island and the field-induced resonance consists in the response to the driving field: while the

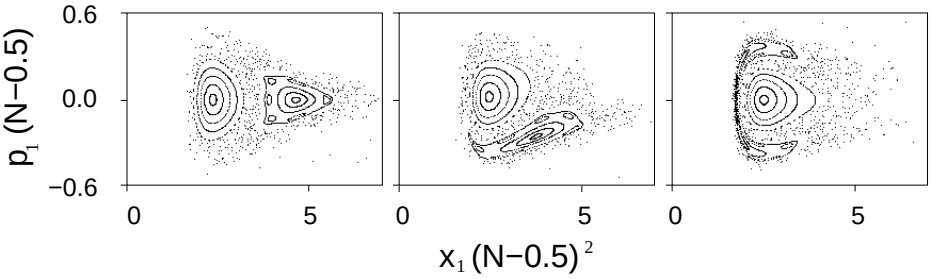

Figure 6.1: Poincaré surface of section of the collinear driven frozen planet configuration for $\omega = 0.2(N-0.5)^{-3}$a.u., field amplitude $F = 0.005(N-0.5)^{-3}$ a.u., and field phase $\omega t = 0$ (left), $\omega t = \pi/2$ (center), $\omega t = \pi/2$ (right) [19]. Whilst the intrinsic island centered around the equilibrium position remains basically at rest during the time evolution, the resonance island oscillates with the field.

intrinsic island remains basically unaffected by the field, the 1 : 1 resonance island oscillates around the intrinsic island with the same field frequency.

Coming to the general case, small deviations from the collinear configuration completely destroy the correlated configurations associated with the above regular islands [95]: in this case, due to the high dimension of phase space, a visualization of its structure becomes much more demanding. However, an extensive statistical analysis of the time evolution for a dense set of initial conditions close to the stable collinear configuration shows that, after a few driving field periods, the movement of the electrons loses its characteristic correlation, and one of the electrons leaves the atom, i.e., the system ionizes [19].

Though, an additional, weak electrostatic field (typically 10% of the driving field amplitude) directed along the polarization axis of the driving field can be used to stabilize the configurations anchored to the elliptic resonance islands of the collinear model: in some analogy to the resonantly driven hydrogen atom [18], where an electrostatic field tends to confine the electron to the vicinity of the polarization axis of the driving field, the electrostatic field preserves the correlation of the driven two-electron system.

6.2 Husimi distributions

As follows from the previous discussion, we are interested in the localization properties along the frozen planet configuration of driven 2D He states. For that purpose we use an appropriate projection of the Husimi distribution of driven states, based on the projection (5.15) of the coherent states along the x axis. However, for the driven case, the Husimi function (5.17) deduced from the time independent projector (2.52) discussed in section 5.2.2 is not valid. In this case, using a similar reasoning as the one presented in section 2.5.2 for the deduction of the electronic density of Floquet states (2.74) in configuration space, the time evolution operator (2.53), together with equation (5.15), yields the following expression for the projection of the Husimi function on the collinear subspace:

$$\begin{aligned} W_\psi(q,p,t) &= \left| \int d\boldsymbol{r} \phi_{q,p}(\boldsymbol{r}) \phi_p(\boldsymbol{r},t) \right|^2 \\ &= e^{2\mathrm{Im}\,(\varepsilon_{p,\theta} t)} \mathrm{Re} \sum_{k,k'} e^{-i(k-k')\omega t} \int d\boldsymbol{r} \phi^*_{q,p}(\boldsymbol{r}) \langle \boldsymbol{r}|R(-\theta)|\phi^k_{\varepsilon_p,\theta}\rangle \times \\ &\quad \times \int d\boldsymbol{r}' \phi_{q,p}(\boldsymbol{r}') \langle \boldsymbol{r}'|R(-\theta)|\phi^{k'}_{\varepsilon_p,\theta}\rangle, \end{aligned} \tag{6.1}$$

with $\phi_{q,p}(\boldsymbol{r})$ the projection (5.15) of the coherent states, and $|\phi^k_{\varepsilon_p,\theta}\rangle$ the Fourier components of the Floquet state $|\phi_{\varepsilon_p,\theta}(t)\rangle$.

6.3 Driven 2D frozen planet states

For our numerical investigation of the time evolution of frozen planet states under periodic driving we choose the field frequency $\omega = 0.2(N-0.5)^{-3}$ a.u., close to the intrinsic frequency (5.6), and the field amplitude $F = 0.005(N-0.5)^{-4}$ a.u. With these field parameters, as observed in figure 6.1, the 1 : 1 resonance island and the intrinsic island are very well pronounced. As discussed in section 5.3.1, the unperturbed frozen planet states show features of the semiclassical prediction starting at the $N = 6$ series. Therefore we concentrate on this series, for which $\omega = 0.0012$ a.u., and $F = 5.5 \times 10^{-5}$ a.u.

The number of photons to reach the double ionization threshold from the $N = 6$, $n_F = 1$ FPS is 61, which, however, is significantly reduced if we account for the finite shift of the effective ionization threshold to lower values – induced by the finite size of the basis used in any numerical calculation (see also our discussion of figure 4.3) [79]. For instance, with $n_{\mathrm{base}} = 200$ (for which

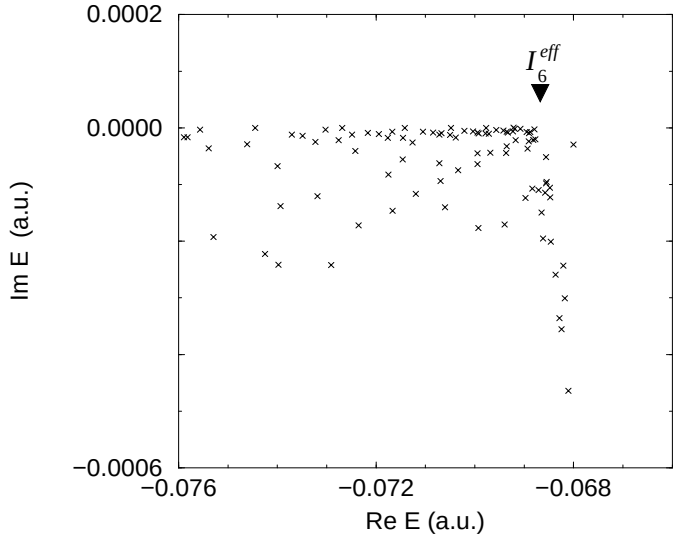

Figure 6.2: Complex Floquet spectrum of the field-free 2D helium atom for $n_{\text{base}} = 200$, close to $I_6 = -0.0661157\,\text{a.u.}$. Due to the truncation of the basis, highly doubly excited states are not reproduced by this basis set, and thus these states are indistinguishable from continuum states. Continuum states are rotated around the effective ionization threshold $I_6^{\text{eff}} \simeq -0.0686\,\text{a.u.}$

we obtain good convergence below the 6th ionization threshold in the field-free case) states above the 11th ionization threshold are no more converged, therefore the effective double ionization threshold $I_\infty^{\text{eff}} \simeq I_{11} = -0.018\,\text{a.u.}$, and thus the number of photons to reach I_∞^{eff} is approximately 42 – smaller than 61, though still beyond the capacity of computing facilities we have access to.

On the other hand, in this highly excited spectral range we already expect that semiclassical predictions are applicable. In particular, as described in section 6.1, the classical dynamics of the driven frozen planet suggest that the system decays via ionization of a single electron. Therefore, we can assume that single ionization process is the dominant decay process, and thus only need to reach the next single ionization threshold. Again, highly excited states close to the ionization threshold are not reproduced by a finite basis, and numerically we obtain an effective ionization threshold depending on the truncation parameter. In particular, for $n_{\text{base}} = 200$, $I_6^{\text{eff}} \simeq 0.0686\,\text{a.u.}$ (s. figure 6.2). Thus, the number of photons to reach I_6^{eff} from the fundamental FPS is 4.

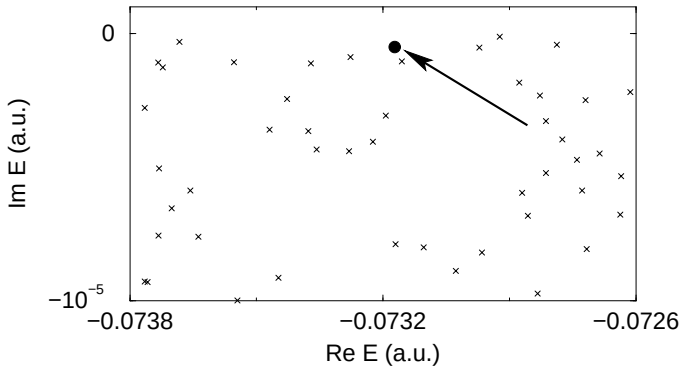

Figure 6.3: Complex Floquet spectrum obtained after diagonalization of (2.55) for triplet states, in the lower half of the complex plane. The real parts of the resonance poles (crosses) correspond to the energies, the imaginary parts to half the decay rates of the atomic resonance states in the field. The state highlighted by a black spot at $Re(E) = -0.0731723$ a.u. shows the largest overlap with the third excited FPS of the $N = 6$ series. $F = 5.5 \times 10^{-6}$ a.u., $\omega = 0.0012$ a.u., $n_{\text{base}} = 200$, 7 photon blocks, $l_{\max} = 3$, $n_{\text{tot}} = 521795$.

Even for small photon numbers, due to the periodicity of the Floquet spectrum, the local density of states enhances dramatically as compared to the field-free case. For instance, a typical Floquet spectrum obtained by diagonalization of (2.55) for $k_{\min} = -2$, $k_{\max} = 4$ and $l_{\max} = 3$ is shown in figure 6.3. There, the real and imaginary parts of the quasienergies with triplet symmetry are shown within one Floquet zone. In this plot the state marked with a black spot shows the largest overlap (83%) with the $N = 6$, $n_F = 3$ FPS of the unperturbed atom.

Fig. 6.4 shows the projection of the electronic density (6.1) of the outer electron of the Floquet state with largest overlap with the $N = 6$, $n = 3$ FPS on the classical phase space component spanned by x_1 and p_1 for different phases of the driving field. For comparison, also the classical phase space structure of the restricted collinear dynamics is shown. Clearly, this state is entirely associated with the chaotic phase space domain. Furthermore, it is localized on the unstable (hyperbolic) fix point of the 1:1 resonance. In addition, the electronic density in configuration space (Fig. 6.5) shows remarkably accentuated fingerprints of the original unperturbed FPS (s. figure 5.8 (c)). However, the influence of the external driving is particularly pronounced in the dynamics of the outer electron: the latter follows the oscillations of the

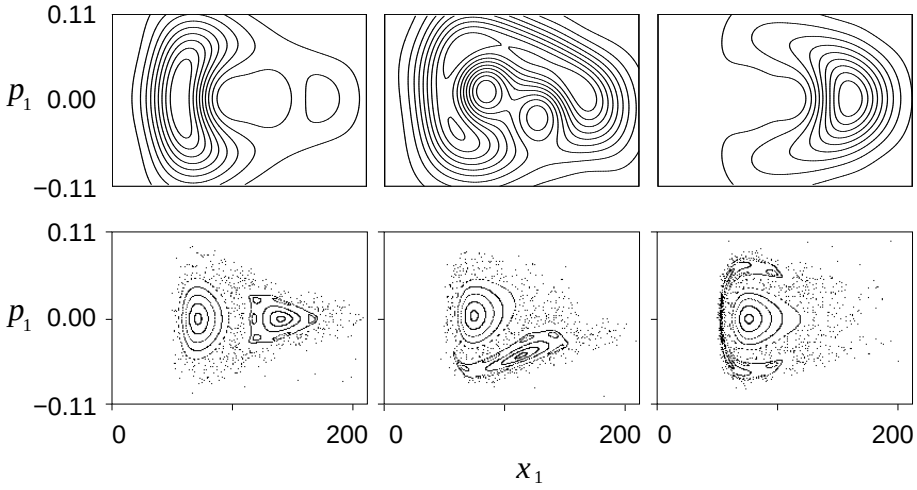

Figure 6.4: Contour plot of the Husimi distribution (6.1) of the wave packet triplet eigenstate (top) along a $N = 6$ frozen planet trajectory of 2D helium, under electromagnetic driving at frequency $\omega = 0.0012$ a.u. and amplitude $F = 5.5 \times 10^{-6}$ a.u., projected onto the phase space component spanned by x_1 and p_1 (the position and momentum of the outer electron). For comparison, also the classical phase space structure of the restricted collinear problem [19] is shown (bottom), for the same driving field parameter. Clearly, the electronic density is associated with the chaotic phase space region, and is localized around the hyperbolic fix point of the 1:1 resonance.

field (c1-3), while the inner electron remains unaffected (b1-3). Moreover, though the electronic density of the outer electron (c1-3) is slightly broadened in the transverse direction y, it does not show any dispersion in this direction.

For this specific calculation, the matrix $\mathcal{A}$ of (2.59) almost saturates the largest currently available supercomputer in Germany (IBM p690 at RZG Garching), and even then, with a rather small value of $l_{\max}$, we cannot expect that all eigenvalues are well converged. For a well converged eigenvalue, one expects that the contributions from large values of the angular momentum vanish, as well as the contributions from distant k-blocks. For the particular eigenstate we are considering here, we observe that the main contribution to the eigenvector comes from $|l| = 0$ and $k = 2$, what is consistent with the fact that the original $n_F = 3$ FPS is a zero angular momentum state, and that the energy difference with the Floquet wave packet quasienergy is approximately 2ω. However, what is more interesting is that the contributions from other angular momenta and from other k-blocks are smaller by few orders of

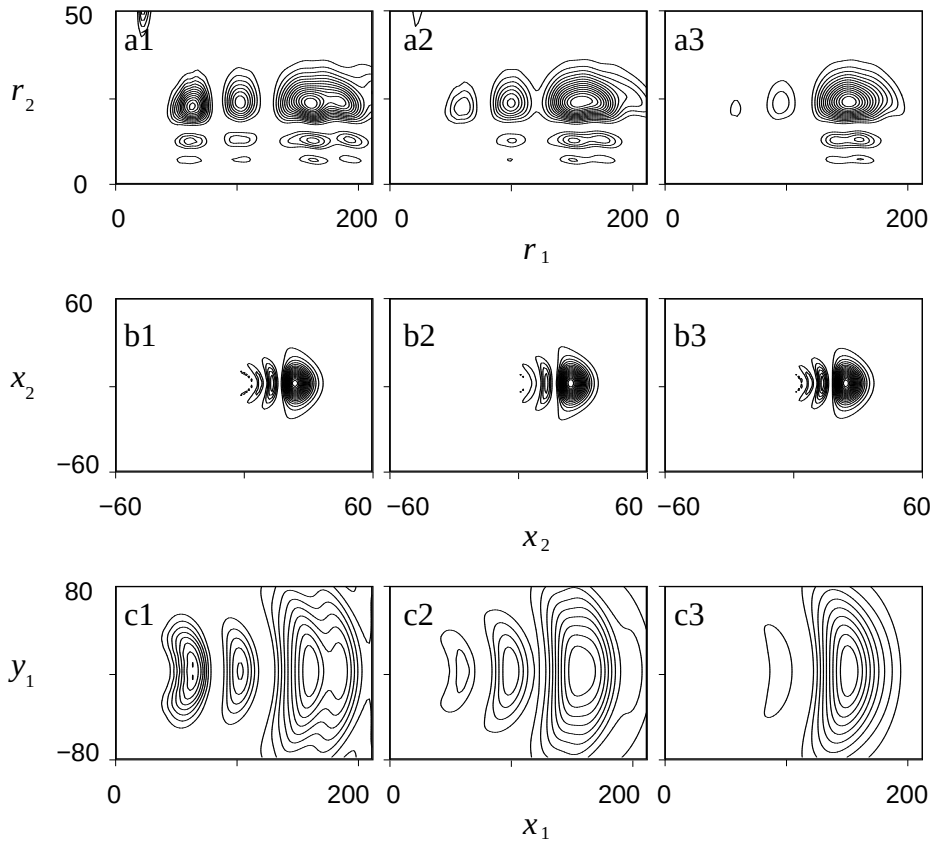

Figure 6.5: Electronic density of the $N = 6$ triplet wave packet in configuration space, for different phases of the driving field: $\omega t = 0$ (a1, b1, c1), $\omega t = \pi/2$ (a2, b2, c2), $\omega t = \pi$ (a3, b3, c3). (a1-3) show the electronic density as function of the distances r_1 and r_2 of the electrons from the nucleus, for $\theta_{12} = 0$. (b1-3) depict the electronic density of the inner electron, when the outer electron is fixed at $r_1 \simeq 165$ a.u., the maximum in (a1-3). In (c1-3) the probability density of the outer electron is depicted, for the inner electron fixed at $r_2 \simeq 23$ a.u.

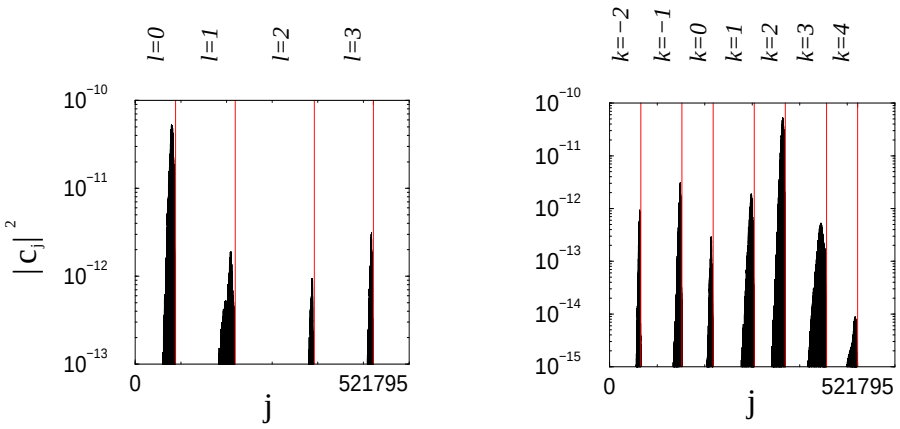

Figure 6.6: Square modulus of the vector components of the non-normalized Floquet eigenvector which shows the largest overlap with the $N = 6$, $n_F = 3$ triplet FPS. In the left plot, the truncated basis ($n_{\text{base}} = 200$, $l_{\max} = 3$ $k_{\min} = -2$, $k_{\max} = 4$) is ordered in angular momentum, from $|l| = 0$ (left) to $|l| = 3$ (right), whilst in the right plot the ordering is determined by the photon number k, from $k = -2$ (left) to $k = 4$ (right).

magnitude, as observed in figure 6.6, where the square modulus of the corresponding vector components are shown. In the right plot we see that the contribution from $k = 4$, i.e., from the continuum above the 6th ionization threshold is indeed negligible. On the other hand, from the left plot we observe that the contribution from large angular momenta is approximately two orders of magnitude smaller than for $l = 0$ though not yet completely negligible. Hence, our present results must be considered as preliminary as far as the detailed spectral properties of the driven system are concerned. However, it seems very unlikely that the close correspondence between classical and quantum dynamics in the reduced phase space (Fig. 6.4) is accidental. We are therefore confident that our present preliminary conclusions will be confirmed by more accurate calculations in the near future.

At present, we have determined the quasienergy of the resonance state of figure 6.5 at $E = -0.0731723$ a.u., and we can estimate its decay rate as $\Gamma/2 < 10^{-6}$, which, in the worst case, implies a life time of at least 100 field periods – already a quite satisfactory value for standard wave packets [114], though still far from the life times of nondispersive wave packets in one electron Rydberg systems [18, 20].

Furthermore, for the particular Rydberg series under study, we have evidence

for the existence of Floquet states localized in the intrinsic island, as well as on the resonance island. However, on the basis of our present numerical data we cannot come up with a definitively affirmative statement, since we still observe large weights of the $l_{\max} = 3$ and/or of the $k = 4$ components associated eigenvectors.

We have also investigated the $N = 3, 4$ and 5 Rydberg series, but so far only for $N = 3$ ($F = 1.28 \times 10^{-4}$ a.u., $w = 0.0128$ a.u.) we obtain converged Floquet states localized on the intrinsic island and on the phase space region anchored to the 1:1 resonance (Fig. 6.7). While the intrinsic state is almost unaffected by the field, the 1:1 resonance state reflects the periodic oscillations of the field. The complex quasienergies of these states in atomic units are

$$\begin{aligned} E_{\text{intrinsic}} &= -0.354888 - i\,3.73 \times 10^{-6}, \\ E_{\text{wavepacket}} &= -0.3425432 - i\,3.77 \times 10^{-6}, \end{aligned} \tag{6.2}$$

respectively. Thus, the life time of both states is approximately 300 field periods. However, as expected from semiclassical considerations [19], both, the intrinsic and the resonance island, are too small to fully support a well localized quantum state, as seen from figure 6.7.

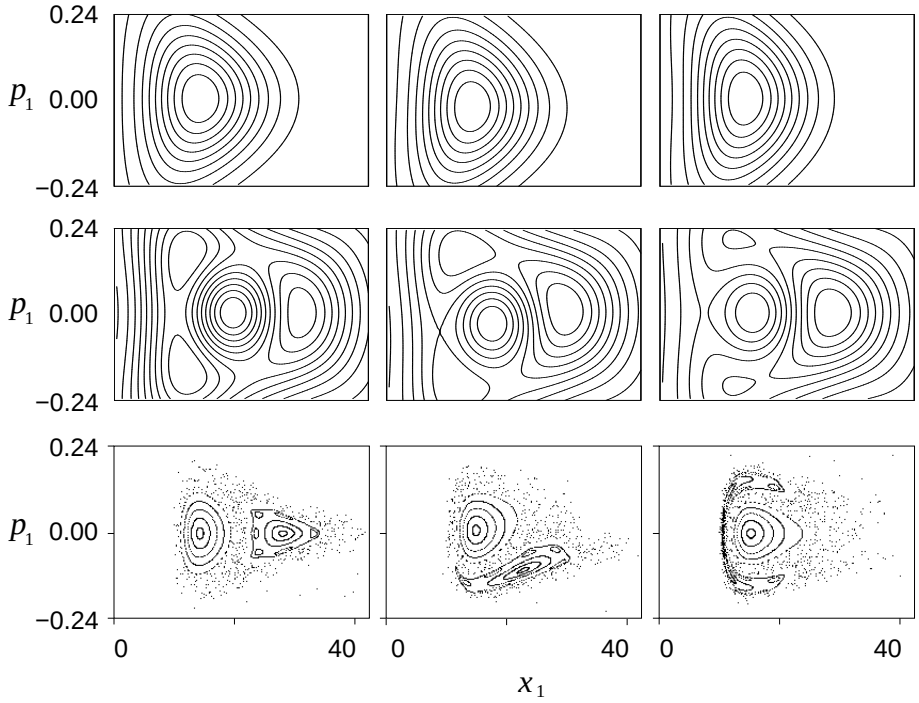

Figure 6.7: Projected Husimi distribution (6.1) onto the phase space component spanned by the position x_1 and momentum p_1 of the outer electron, for the Floquet state associated with the $N = 3$ intrinsic island (top) and the field-induced resonance (center) of the driven frozen planet configuration. Driving frequency $\omega = 0.0128\,\text{a.u.}$, amplitude $F = 1.28 \times 10^{-4}\,\text{a.u.}$ Phase $\omega t = 0, \pi/2, \pi$, from left to right. Whilst the intrinsic state is almost unaffected by the field, the wave packet reflects the periodic time dependence of the field. However, the resonance and the intrinsic islands (bottom) are too small to support a well-localized eigenstate.

Chapter 7

Summary and perspectives

7.1 Summary

In the present thesis, we provided a complete description of the spectra of 2D helium, and studied the quantum dynamics of the near resonantly driven frozen planet configuration. To achieve this purpose we developed an original method for the accurate quantum treatment of the planar three body problem under periodic diving. Our approach combines sophisticated theoretical methods, symbolic calculus, and advanced parallel computing techniques, and allows for an exact quantum description of both, highly doubly excited states of helium, and of the field-induced coupling of atomic bound and resonance states with the atomic continuum.

In our description of the spectrum of the 2D Coulomb problem the eigenstates of 2D helium are labeled by parity exchange symmetry, the symmetry Π_x with respect to the x axis, and the absolute value $|l|$ of the total angular momentum. As in the 3D atom, 2D helium states are organized in Rydberg series converging to well defined single ionization thresholds $I_N = -Z^2/(2(N-1/2)^2)$. The Rydberg series converging to the I_1 is bound, while series of doubly excited states are resonance states, with one exception: A hitherto unknown series of bound triplet and singlet states of $\Pi_x = -1$ symmetry, with $|l| = 0$ converges to the 2nd ionization threshold.

A study of the level and decay rate dynamics as a function of the strength of the electron-electron interaction allows to characterize moderately doubly excited states by quantum numbers N and n that individually label the excitation of each electron. On the other hand, this analysis shows that the complexity of the spectrum rapidly increases with the excitation: starting

from the 5th Rydberg series, all states mix, due to series overlap. Thus, the highly doubly excited regime is dominantly characterized by avoided crossings which significantly change the features of the original eigenstates of two non-interacting electrons.

In the doubly excited regime, we found quantum states that are localized along the frozen planet orbit of the classical dynamics. A comparison of 1D and 2D frozen planet states shows an important enhancement of the decay rates in the latter case, but surprisingly good quantitative agreement with 3D results. Though 2D frozen planet states are localized more faithfully along the collinear configuration than 3D states, as a consequence of the confinement to two dimensions. The enhancement of the decay rates confirms a hypothesis formulated by the authors of [19, 92] according to which the ionization of these states is dominantly due to the transverse degrees of freedom. This, in particular, implies that one has to be careful when simple one-dimensional models are used to explain ionization processes of real atoms.

For the driven atom, we studied the near resonantly driven frozen planet configuration: our numerical experiments suggest the existence of wave packed-like dressed states that trace the classical frozen planet trajectory, and thus provide strong evidence for the existence of nondispersive wave packets in driven 2D helium. Furthermore, contrary to the classical case, where an additional electrostatic field is necessary to stabilize chaotic trajectories of the driven frozen planet, the quantum wave packets appear to be localized in the transverse direction. The origin of this non-classical localization can have various causes [115], but remains to be elucidated. Finally, our present numerical data only allow for a preliminary estimate of the life times of these wave packets. The resulting values of a few hundred field cycles are long as compared to standard wave packets, though short as compared to the life times of nondispersive wave packets in one electron Rydberg systems [18].

7.2 Outlook

One of the main results of this thesis is the similarity of the decay rates of 2D and 3D frozen planet states. This suggests that a two dimensional approach can extract the most relevant qualitative features of realistic helium ionization processes (if not also reproduce quantitative observations). In particular, we expect that an exact quantum treatment of the double ionization process of planar helium from the ground state, induced by strong

laser fields, will explain the major part of the intricate, experimentaly observed manifestations of the interelectronic repulsion [7, 8], and in particular the involved geometry of the fragmentation process [13, 14]. Our approach is perfectly adapted for the treatment of this problem.

Furthermore, our approach is equally appropriate for the treatment of 2D trions in semiconductors [31], 2D two-electron quantum dots [37] or H_2^+ (with and without field): in the general planar three body Coulomb problem, with finite masses of all three particles, the particle exchange symmetry and the Π_x symmetry are broken, but, still, the representation of the corresponding eigenvalue problem will lead to banded matrices with analytic expressions for the matrix elements.

The principal practical obstacle that we do and will encounter here is the huge dimension of the eigenvalue problem, which comes from the slow decrease of our Fock state basis set, at large distances. For this reason, it might be worthwhile to explore the performance of alternative basis sets such as, for instance, perimetric coordinates, which have been successfully used in exact quantum calculations on unperturbed 3D helium. However, in the 2D case these coordinates show serious complications from the very beginning: due to the restriction to the plane, the transformation from perimetric to Cartesian coordinates is not continuous, and further investigations are necessary. Notwithstanding these specific problems, however, the machinery which we have developed in the present thesis is easily adaptable to such alternative representations.

Appendix A

Numerics

A.1 Parabolic transformations

In this section we derive some usefully expressions obtained by transformation from Cartesian (x_1, y_1, x_2, y_2) to parabolic coordinates (x_p, y_p, x_m, y_m), as defined in equations (2.7,2.8) and (2.9). Note that in these transformations two fundamental planar transformations are involved, that are used several times: a parabolic transformation and a rotation by $\pi/4$.

We start with a single generic parabolic transformation between the coordinates (x, y) and (μ, ν), defined by

$$\begin{array}{ll} x = \frac{1}{2}(\mu^2 - \nu^2), & \mu = \sqrt{r + x}, \\ y = \mu\nu, & \nu = \sqrt{r - x}, \\ \text{with} \quad r = \sqrt{x^2 + y^2} = \frac{1}{2}(\mu^2 + \nu^2). & \end{array} \tag{A.1}$$

In this case the partial derivatives are expressed as

$$\begin{aligned} \frac{\partial}{\partial x} &= \frac{1}{2r}\left(\mu\frac{\partial}{\partial \mu} - \nu\frac{\partial}{\partial \nu}\right), \\ \frac{\partial}{\partial y} &= \frac{1}{2r}\left(\nu\frac{\partial}{\partial \mu} + \mu\frac{\partial}{\partial \nu}\right), \end{aligned} \tag{A.2}$$

and the two dimensional Laplacian is given by

$$\frac{\partial^2}{\partial x^2} + \frac{\partial^2}{\partial y^2} = \frac{1}{\mu^2 + \nu^2}\left(\frac{\partial^2}{\partial \mu^2} + \frac{\partial^2}{\partial \nu^2}\right) = \frac{2}{r}\left(\frac{\partial^2}{\partial \mu^2} + \frac{\partial^2}{\partial \nu^2}\right). \tag{A.3}$$

The coordinate transformation (2.8) involves two rotations of the type

$$\begin{array}{rclcrcl} x &=& \frac{1}{\sqrt{2}}(u + v) & & u &=& \frac{1}{\sqrt{2}}(x + y) \\ y &=& \frac{1}{\sqrt{2}}(u - v) & & v &=& \frac{1}{\sqrt{2}}(x - y), \end{array} \tag{A.4}$$

thus the derivatives are given by

$$\begin{aligned}\frac{\partial}{\partial x} &= \frac{1}{\sqrt{2}}\left(\frac{\partial}{\partial u}+\frac{\partial}{\partial v}\right),\\ \frac{\partial}{\partial y} &= \frac{1}{\sqrt{2}}\left(\frac{\partial}{\partial u}-\frac{\partial}{\partial v}\right).\end{aligned} \tag{A.5}$$

Now let us consider the full transformation between (x_1, y_1, x_2, y_2) and (x_p, y_p, x_m, y_m). The Cartesian coordinates are given in terms of the parabolic ones by

$$\begin{aligned}x_1 &= \frac{1}{4}\left(-(x_m y_m + x_p y_p)^2 + \frac{1}{4}(x_m^2 + x_p^2 - y_m^2 - y_p^2)^2\right),\\ y_1 &= \frac{1}{4}(x_m y_m + x_p y_p)(x_m^2 + x_p^2 - y_m^2 - y_p^2),\\ x_2 &= \frac{1}{4}\left(-(x_m y_m - x_p y_p)^2 + \frac{1}{4}(x_m^2 - x_p^2 - y_m^2 + y_p^2)^2\right),\\ y_2 &= \frac{1}{4}(x_m y_m - x_p y_p)(x_m^2 - x_p^2 - y_m^2 + y_p^2).\end{aligned} \tag{A.6}$$

From here it follows immediately that

$$x_1 + x_2 = \frac{1}{8}(x_p^4 + y_p^4 + x_m^4 + y_m^4 - 6x_m^2 y_m^2 - 6x_p^2 y_p^2), \tag{A.7}$$

and the expressions of $r_1 = \sqrt{x_1^2 + y_1^2}$, $r_2 = \sqrt{x_2^2 + y_2^2}$ and $r_{12} = \sqrt{(x_1 - x_2)^2 + (y_1 - y_2)^2}$ in parabolic coordinates are

$$\begin{aligned}r_1 &= \frac{1}{16}\left((x_p - y_m)^2 + (x_m + y_p)^2)((x_p + y_m)^2 + (x_m - y_p)^2\right),\\ r_2 &= \frac{1}{16}\left((x_p - x_m)^2 + (y_p - y_m)^2)((x_p + x_m)^2 + (y_p + y_m)^2\right),\\ r_{12} &= \frac{1}{4}(x_p^2 + y_p^2)(x_m^2 + y_m^2).\end{aligned} \tag{A.8}$$

A.1.1 Kinetic operator $T = 16 r_1 r_2 r_{12}(\nabla_1^2 + \nabla_2^2)$

In this section we find the expression of the kinetic term T in (2.13) in terms of the parabolic coordinates (x_p, y_p, x_m, y_m).

The transformation (2.7) consists of two planar parabolic transformations. Therefore, after choosing the appropriate subindices in (A.3), the expression

for $T/16r_1r_2r_{12}$, in terms of the coordinates $(\mu_1, \nu_1, \mu_2, \nu_2)$ defined in (2.7), is given by

$$\nabla_1^2 + \nabla_2^2 = \frac{2}{r_1}\nabla^2_{\mu_1,\nu_1} + \frac{2}{r_2}\nabla^2_{\mu_2,\nu_2}, \tag{A.9}$$

where $\nabla^2_{\mu_i,\nu_i} = \partial^2/\partial{\mu_i}^2 + \partial^2/\partial{\nu_i}^2$ $(i = 1, 2)$.

The transformation (2.8) consists of two rotations by $\pi/2$ in the plane. Therefore, the derivatives of (μ_1, μ_2) and (ν_1, ν_2) are related to the derivatives of (μ_p, μ_m) and (ν_p, ν_m), respectively, by expressions similar to (A.5). After substitution of these expressions in $\nabla^2_{\mu_i,\nu_i}$ we obtain

$$\nabla^2_{\mu_i,\nu_i} = \frac{\partial^2}{\partial\mu_p^2} + \frac{\partial^2}{\partial\nu_p^2} + \frac{\partial^2}{\partial\mu_m^2} + \frac{\partial^2}{\partial\nu_m^2} + (-1)^i\left(\frac{2\partial^2}{\partial\mu_p\partial\mu_m} + \frac{2\partial^2}{\partial\nu_p\partial\nu_m}\right), \tag{A.10}$$

for $i = 1, 2$.

The final transformation (2.9) consists again of two planar parabolic transformations between (μ_α, ν_α) and (x_α, y_α), for $\alpha = p, m$. Therefore, $\partial/\partial\mu_\alpha$ and $\partial/\partial\nu_\alpha$ are related to $\partial/\partial x_\alpha$, $\partial/\partial y_\alpha$ by expressions similar to (A.2). Hence, the expression for $2\partial^2/\partial\mu_p\partial\mu_m + 2\partial^2/\partial\nu_p\partial\nu_m$ in (A.10) reads

$$\frac{1}{(x_p^2+y_p^2)(x_m^2+y_m^2)}\left\{(x_mx_p + y_my_p)\left(\frac{\partial^2}{\partial x_m\partial x_p} + \frac{\partial^2}{\partial y_m\partial y_p}\right) + (y_mx_p - x_my_p)\left(\frac{\partial^2}{\partial x_m\partial y_p} - \frac{\partial^2}{\partial y_m\partial x_p}\right)\right\}. \tag{A.11}$$

Finally, since the other terms of (A.10) are Laplacians which transform according to (A.3), then coming back to (A.9), we obtain

$$\begin{aligned} T \;=\; & (r_1+r_2)\left\{(x_p^2+y_p^2)\left(\frac{\partial^2}{\partial x_m^2} + \frac{\partial^2}{\partial y_m^2}\right) + (x_m^2+y_m^2)\left(\frac{\partial^2}{\partial x_p^2} + \frac{\partial^2}{\partial y_p^2}\right)\right\} + \\ & 2(r_2-r_1)\left\{(x_mx_p + y_my_p)\left(\frac{\partial^2}{\partial x_m\partial x_p} + \frac{\partial^2}{\partial y_m\partial y_p}\right) + \right. \\ & \left.(y_mx_p - x_my_p)\left(\frac{\partial^2}{\partial x_m\partial y_p} - \frac{\partial^2}{\partial y_m\partial x_p}\right)\right\}. \end{aligned} \tag{A.12}$$

A.1.2 The field term in the velocity gauge

In this section we find the expression of the field term in the velocity gauge, $16r_1r_2r_{12}(\partial_{x_1} + \partial_{x_2})$, in parabolic coordinates.

Along similar lines as in our above derivation of T in parabolic coordinates we obtain the corresponding expressions for $\partial/\partial x_1$ and $\partial/\partial x_2$:

$$\frac{\partial}{\partial x_i} = \frac{1}{4r_i}\left(\frac{1}{x_p^2+y_p^2}P_i + \epsilon_i \frac{1}{x_m^2+y_m^2}Q_i\right), \quad \text{for } i=1,2. \tag{A.13}$$

Here $\epsilon_i = (-1)^i$, and P_i and Q_i are polynomial expressions in the parabolic coordinates and in their derivatives:

$$\begin{aligned} P_i &= (\mu_p + \epsilon_i\mu_m)\left(x_p\frac{\partial}{\partial x_p} - y_p\frac{\partial}{\partial y_p}\right) - (\nu_p + \epsilon_i\nu_m)\left(y_p\frac{\partial}{\partial x_p} + x_p\frac{\partial}{\partial y_p}\right), \\ Q_i &= (\mu_p + \epsilon_i\mu_m)\left(x_m\frac{\partial}{\partial x_m} - y_m\frac{\partial}{\partial y_m}\right) - (\nu_p + \epsilon_i\nu_m)\left(y_m\frac{\partial}{\partial x_m} + x_m\frac{\partial}{\partial y_m}\right). \end{aligned} \tag{A.14}$$

From (A.8) it is clear that also $16r_1r_2r_{12}\partial_{x_i}$, for $i=1,2$, has a polynomial expression, hence also the field term $16r_1r_2r_{12}(\partial_{x_1}+\partial_{x_2})$ in (2.56). Furthermore, it can be shown that the polynomial expression for $r_1r_2(\partial_{x_1}+\partial_{x_2})$ is given by

$$r_1r_2\left(\frac{\partial}{\partial x_1}+\frac{\partial}{\partial x_2}\right) = P_{x_p}\frac{\partial}{\partial x_p} + P_{x_m}\frac{\partial}{\partial x_m} + P_{y_p}\frac{\partial}{\partial y_p} + P_{y_m}\frac{\partial}{\partial y_m}, \tag{A.15}$$

where

$$\begin{aligned} P_{x_p} &= -x_m^4x_p + x_p^5 + 6x_m^2x_py_m^2 - x_py_m^4 - 4x_m^3y_my_p + \\ &\quad 4x_my_m^3y_p - 2x_p^3y_p^2 - 3x_py_p^4, \\ P_{x_m} &= x_m^5 - x_mx_p^4 - 2x_m^3y_m^2 - 3x_my_m^4 - 4x_p^3y_my_p + \\ &\quad 6x_mx_p^2y_p^2 + 4x_py_my_p^3 - x_my_p^4, \\ P_{y_p} &= 4x_m^3x_py_m - 4x_mx_py_m^3 - x_m^4y_p - 3x_p^4y_p + 6x_m^2y_m^2y_p - \\ &\quad y_m^4y_p - 2x_p^2y_p^3 + y_p^5, \\ P_{y_m} &= -3x_m^4y_m - x_p^4y_m - 2x_m^2y_m^3 + y_m^5 + 4x_mx_p^3y_p + \\ &\quad 6x_p^2y_my_p^2 - 4x_mx_py_p^3 - y_my_p^4. \end{aligned} \tag{A.16}$$

A.2 Hamiltonian and selection rules

In this part of the appendix we explicitly show the Hamiltonian of the field free atom in terms of the circular operators. More precisely, the expression

we show on the next page is the the representation of $\mathcal{H}_0 = -1/2T + V$ (see eq. (2.12)) for $Z = 2$ and $\gamma = 1$. It contains 423 terms and 91 selection rules.

Including the Jacobian, $-1/2T + V - EB$ contains 1511 terms, which is already too large to be shown here (and even larger if we include the external driving). However, in table A.2 the 159 selection rules $\{\Delta n_1, \Delta n_2, \Delta n_3, \Delta n_4\}$ of the unperturbed case are shown.

Unperturbed Hamiltonian $\mathcal{H}_0 = -T/2 + V$

$$
\begin{aligned}
&-8 - 17\,a_1^\dagger a_2^\dagger - \frac{33}{8}a_1^{\dagger 2}a_2^{\dagger 2} + \frac{1}{16}a_1^{\dagger 4}a_2^{\dagger 4} - 17\,a_3^\dagger a_4^\dagger - \frac{75}{2}a_1^\dagger a_2^\dagger a_3^\dagger a_4^\dagger - \frac{19}{2}a_1^{\dagger 2}a_2^{\dagger 2}a_3^\dagger a_4^\dagger - \frac{9}{8}a_1^{\dagger 3}a_2^{\dagger 3}a_3^\dagger a_4^\dagger - \frac{33}{8}a_3^{\dagger 2}a_4^{\dagger 2} - \frac{19}{2}a_1^\dagger a_2^\dagger a_3^{\dagger 2}a_4^{\dagger 2} + \frac{1}{8}a_1^{\dagger 2}a_2^{\dagger 2}a_3^{\dagger 2}a_4^{\dagger 2} - \\
&\frac{9}{8}a_1^\dagger a_2^\dagger a_3^{\dagger 3}a_4^{\dagger 3} + \frac{1}{16}a_3^{\dagger 4}a_4^{\dagger 4} - 16\,a_1^\dagger a_1 - \frac{31}{4}a_1^{\dagger 2}a_2^\dagger a_1 + \frac{1}{8}a_1^{\dagger 3}a_2^{\dagger 2}a_1 + \frac{1}{4}a_1^{\dagger 4}a_2^{\dagger 3}a_1 - \frac{1}{8}a_2^{\dagger 3}a_3^{\dagger 4}a_1 - \frac{71}{2}a_1^\dagger a_3^\dagger a_4^\dagger a_1 - \frac{75}{4}a_1^{\dagger 2}a_2^\dagger a_3^\dagger a_4^\dagger a_1 - \frac{13}{4}a_1^{\dagger 3}a_2^{\dagger 2}a_3^\dagger a_4^\dagger a_1 - \\
&\frac{69}{8}a_1^\dagger a_3^{\dagger 2}a_4^{\dagger 2}a_1 + \frac{1}{8}a_1^{\dagger 2}a_2^\dagger a_3^{\dagger 2}a_4^{\dagger 2}a_1 - a_1^\dagger a_3^{\dagger 3}a_4^{\dagger 3}a_1 - \frac{29}{8}a_1^{\dagger 2}a_2^{\dagger 2} + \frac{1}{4}a_1^{\dagger 3}a_2^\dagger a_3^{\dagger 2} + \frac{3}{8}a_1^{\dagger 4}a_2^{\dagger 2}a_3^{\dagger 2} - \frac{3}{8}a_2^{\dagger 2}a_3^{\dagger 4}a_4^{\dagger 2} - \frac{37}{4}a_1^{\dagger 2}a_3^\dagger a_4^\dagger a_1^2 - \frac{25}{8}a_1^{\dagger 3}a_2^\dagger a_3^\dagger a_4^\dagger a_1^2 + \frac{1}{8}a_1^{\dagger 3}a_3^\dagger + \\
&\frac{1}{4}a_1^{\dagger 4}a_2^\dagger a_3^3 - \frac{3}{8}a_2^\dagger a_3^{\dagger 4}a_4^3 - a_1^{\dagger 3}a_3^\dagger a_4^\dagger a_3^3 + \frac{1}{16}a_1^{\dagger 4}a_4^4 - \frac{1}{8}a_3^{\dagger 4}a_4^4 - 16\,a_2^\dagger a_2 - \frac{31}{4}a_1^\dagger a_2^{\dagger 2}a_2 + \frac{1}{8}a_1^{\dagger 2}a_2^{\dagger 3}a_2 + \frac{1}{4}a_1^{\dagger 3}a_2^{\dagger 4}a_2 - \frac{71}{2}a_2^\dagger a_3^\dagger a_4^\dagger a_2 - \frac{75}{4}a_1^\dagger a_2^{\dagger 2}a_3^\dagger a_4^\dagger a_2 - \\
&\frac{13}{4}a_1^{\dagger 2}a_2^{\dagger 3}a_3^\dagger a_4^\dagger a_2 - \frac{69}{8}a_2^\dagger a_3^{\dagger 2}a_4^{\dagger 2}a_2 + \frac{1}{8}a_1^\dagger a_2^{\dagger 2}a_3^{\dagger 2}a_4^{\dagger 2}a_2 - a_2^\dagger a_3^{\dagger 3}a_4^{\dagger 3}a_2 - \frac{1}{8}a_1^{\dagger 3}a_4^{\dagger 4}a_2 - 17\,a_1a_2 - \frac{31}{2}a_1^\dagger a_2^\dagger a_1a_2 + \frac{1}{2}a_1^{\dagger 2}a_2^{\dagger 2}a_1a_2 + a_1^{\dagger 3}a_2^{\dagger 3}a_1a_2 - \\
&\frac{77}{2}a_3^\dagger a_4^\dagger a_1a_2 - 38\,a_1^\dagger a_2^\dagger a_3^\dagger a_4^\dagger a_1a_2 - \frac{77}{8}a_1^{\dagger 2}a_2^{\dagger 2}a_3^\dagger a_4^\dagger a_1a_2 - 10\,a_3^{\dagger 2}a_4^{\dagger 2}a_1a_2 - \frac{9}{8}a_3^{\dagger 3}a_4^{\dagger 3}a_1a_2 - \frac{31}{4}a_1^\dagger a_1^2a_2 + \frac{5}{8}a_1^{\dagger 2}a_2^\dagger a_1^2a_2 + \frac{3}{2}a_1^{\dagger 3}a_2^{\dagger 2}a_1^2a_2 - \frac{77}{4}a_1^\dagger a_3^\dagger a_4^\dagger a_1^2a_2 - \\
&\frac{19}{2}a_1^{\dagger 2}a_2^\dagger a_3^\dagger a_4^\dagger a_1^2a_2 - \frac{1}{8}a_1^\dagger a_3^{\dagger 2}a_4^{\dagger 2}a_1^2a_2 + \frac{1}{4}a_1^{\dagger 2}a_3^\dagger a_2 + a_1^{\dagger 3}a_2^\dagger a_3^\dagger a_2 - \frac{25}{8}a_1^{\dagger 2}a_3^\dagger a_4^\dagger a_1^3a_2 + \frac{1}{4}a_1^{\dagger 3}a_1^4a_2 - \frac{29}{8}a_2^{\dagger 2}a_2^2 + \frac{1}{4}a_1^\dagger a_2^{\dagger 3}a_2^2 + \frac{3}{8}a_1^{\dagger 2}a_2^{\dagger 4}a_2^2 - \frac{37}{4}a_2^{\dagger 2}a_3^\dagger a_4^\dagger a_2^2 - \\
&\frac{25}{8}a_1^\dagger a_2^{\dagger 3}a_3^\dagger a_4^\dagger a_2^2 - \frac{3}{8}a_1^{\dagger 2}a_4^{\dagger 4}a_2^2 - \frac{31}{4}a_2^\dagger a_1a_2 + \frac{5}{8}a_1^\dagger a_2^{\dagger 2}a_1a_2^2 + \frac{3}{2}a_1^{\dagger 2}a_2^{\dagger 3}a_1a_2^2 - \frac{77}{4}a_2^\dagger a_3^\dagger a_4^\dagger a_1a_2^2 - \frac{19}{2}a_1^\dagger a_2^{\dagger 2}a_3^\dagger a_4^\dagger a_1a_2^2 - \frac{1}{8}a_2^\dagger a_3^{\dagger 2}a_4^{\dagger 2}a_1a_2^2 - \frac{33}{8}a_1^{\dagger 2}a_2^2 + \\
&\frac{1}{2}a_1^\dagger a_2^{\dagger 2}a_3^{\dagger 2}a_2^2 + \frac{9}{4}a_1^{\dagger 2}a_2^{\dagger 2}a_3^{\dagger 2}a_2^2 - 10\,a_3^\dagger a_4^\dagger a_1^2a_2^2 - \frac{77}{8}a_1^\dagger a_2^\dagger a_3^\dagger a_4^\dagger a_1^2a_2^2 - \frac{1}{8}a_3^{\dagger 2}a_4^{\dagger 2}a_1^2a_2^2 + \frac{1}{8}a_1^\dagger a_1^3a_2^2 + \frac{3}{2}a_1^{\dagger 2}a_2^\dagger a_3^\dagger a_2^2 - \frac{13}{4}a_1^\dagger a_3^\dagger a_4^\dagger a_1^3a_2^2 + \frac{3}{8}a_1^{\dagger 2}a_1^4a_2^2 + \frac{1}{8}a_2^{\dagger 3}a_3^2 + \\
&\frac{1}{4}a_1^\dagger a_2^{\dagger 4}a_3^2 - a_2^{\dagger 3}a_3^\dagger a_4^\dagger a_3^2 - \frac{3}{8}a_1^\dagger a_4^{\dagger 4}a_3^2 + \frac{1}{4}a_2^{\dagger 2}a_1a_3^2 + a_1^\dagger a_2^{\dagger 3}a_1a_3^2 - \frac{25}{8}a_2^{\dagger 2}a_3^\dagger a_4^\dagger a_1a_3^2 + \frac{1}{8}a_2^\dagger a_1^2a_3^2 + \frac{3}{2}a_1^\dagger a_2^{\dagger 2}a_1^2a_3^2 - \frac{13}{4}a_2^\dagger a_3^\dagger a_4^\dagger a_1^2a_3^2 + a_1^\dagger a_2^\dagger a_3^2a_3^2 - \frac{9}{8}a_3^\dagger a_4^\dagger a_1^2a_3^2 + \\
&\frac{1}{4}a_1^\dagger a_4^\dagger a_3^3 + \frac{1}{16}a_2^{\dagger 4}a_4^2 - \frac{1}{8}a_4^{\dagger 4}a_2^2 + \frac{1}{4}a_2^{\dagger 3}a_1a_2^2 + \frac{3}{8}a_2^{\dagger 2}a_3^\dagger a_4^\dagger a_1a_2^2 + \frac{1}{4}a_2^\dagger a_3^\dagger a_4^\dagger a_1^2a_2^2 + \frac{1}{16}a_1^\dagger a_4^\dagger a_2^2 - 16\,a_3^\dagger a_3 - \frac{71}{2}a_1^\dagger a_2^\dagger a_3^\dagger a_3 - \frac{69}{8}a_1^{\dagger 2}a_2^{\dagger 2}a_3^\dagger a_3 - a_1^{\dagger 3}a_2^{\dagger 3}a_3^\dagger a_3 - \frac{31}{4}a_3^{\dagger 2}a_4^\dagger a_3 - \\
&\frac{75}{4}a_1^\dagger a_2^\dagger a_3^{\dagger 2}a_4^\dagger a_3 + \frac{1}{8}a_1^{\dagger 2}a_2^{\dagger 2}a_3^{\dagger 2}a_4^\dagger a_3 + \frac{1}{8}a_3^{\dagger 3}a_4^{\dagger 2}a_3 - \frac{13}{4}a_1^\dagger a_2^\dagger a_3^{\dagger 3}a_4^{\dagger 2}a_3 - \frac{1}{8}a_1^{\dagger 4}a_4^{\dagger 3}a_3 + \frac{1}{4}a_3^{\dagger 4}a_4^{\dagger 3}a_3 - \frac{67}{2}a_1^\dagger a_3^\dagger a_4^\dagger a_1a_3 - 17\,a_1^{\dagger 2}a_2^\dagger a_3^\dagger a_4^\dagger a_1a_3 - \frac{23}{8}a_1^{\dagger 3}a_2^{\dagger 2}a_3^\dagger a_4^\dagger a_1a_3 - \\
&17\,a_1^\dagger a_3^{\dagger 2}a_4^\dagger a_1a_3 - \frac{23}{8}a_1^\dagger a_3^{\dagger 3}a_4^{\dagger 2}a_1a_3 - \frac{67}{8}a_1^{\dagger 2}a_2^\dagger a_3^{\dagger 2}a_4^\dagger a_2a_3 - \frac{11}{4}a_1^{\dagger 3}a_2^\dagger a_3^\dagger a_4^\dagger a_2^2a_3 - \frac{1}{8}a_1^{\dagger 2}a_3^{\dagger 2}a_4^\dagger a_2^2a_3 - \frac{7}{8}a_1^{\dagger 3}a_3^\dagger a_4^\dagger a_2^2a_3 - \frac{65}{2}a_1^\dagger a_2^\dagger a_3^\dagger a_2a_3 - \frac{33}{8}a_1^\dagger a_2^{\dagger 2}a_3^\dagger a_2a_3 - \\
&\frac{23}{8}a_1^{\dagger 2}a_2^{\dagger 3}a_3^\dagger a_2a_3 - \frac{33}{2}a_2^\dagger a_3^{\dagger 2}a_4^\dagger a_2a_3 + \frac{1}{4}a_1^\dagger a_2^{\dagger 2}a_3^{\dagger 2}a_4^\dagger a_2a_3 - \frac{23}{8}a_2^\dagger a_3^{\dagger 3}a_4^{\dagger 2}a_2a_3 - \frac{3}{4}a_1^{\dagger 3}a_4^{\dagger 3}a_2a_3 - \frac{71}{2}a_3^\dagger a_1a_2a_3 - \frac{67}{2}a_1^\dagger a_2^\dagger a_3^\dagger a_4^\dagger a_2a_3 - \frac{17}{2}a_1^{\dagger 2}a_2^{\dagger 2}a_3^\dagger a_4^\dagger a_2a_3 - \\
&\frac{77}{4}a_3^{\dagger 2}a_4^\dagger a_1a_2a_3 - \frac{13}{4}a_3^{\dagger 3}a_4^{\dagger 2}a_1a_2a_3 - 17\,a_1^\dagger a_3^\dagger a_4^\dagger a_2a_3 - \frac{67}{8}a_1^{\dagger 2}a_2^\dagger a_3^\dagger a_4^\dagger a_2^2a_3 - \frac{1}{4}a_1^\dagger a_3^{\dagger 2}a_4^\dagger a_2^2a_3 - \frac{11}{4}a_1^{\dagger 2}a_3^\dagger a_4^\dagger a_2^2a_3 - \frac{63}{8}a_2^{\dagger 2}a_3^\dagger a_4^\dagger a_2^2a_3 - \frac{11}{4}a_1^\dagger a_2^{\dagger 3}a_3^\dagger a_4^\dagger a_2^2a_3 + \\
&\frac{1}{8}a_2^{\dagger 2}a_3^{\dagger 2}a_4^\dagger a_2^2a_3 - \frac{3}{2}a_1^{\dagger 2}a_4^{\dagger 3}a_2^2a_3 - \frac{33}{2}a_2^\dagger a_3^\dagger a_1a_2^2a_3 - \frac{67}{8}a_1^\dagger a_2^{\dagger 2}a_3^\dagger a_1a_2^2a_3 - \frac{69}{8}a_3^\dagger a_1a_2^2a_3 - \frac{17}{2}a_1^\dagger a_2^\dagger a_3^\dagger a_2^2a_3^2a_3 - \frac{1}{8}a_3^{\dagger 2}a_4^\dagger a_1^2a_2^2a_3 - \frac{23}{8}a_1^\dagger a_3^\dagger a_2^2a_3 - \\
&\frac{7}{8}a_2^{\dagger 3}a_3^\dagger a_2^2a_3 - \frac{5}{4}a_1^\dagger a_4^{\dagger 3}a_2^2a_3 - \frac{11}{4}a_2^{\dagger 2}a_3^\dagger a_1a_2^2a_3 - \frac{23}{8}a_2^\dagger a_3^\dagger a_2^2a_3^2a_3 - a_3^\dagger a_1^3a_2^2a_3 - \frac{3}{8}a_4^{\dagger 3}a_2^2a_3 - \frac{29}{8}a_3^{\dagger 2}a_3^2 - \frac{37}{4}a_1^\dagger a_2^\dagger a_3^{\dagger 2}a_3^2 + \frac{1}{4}a_3^{\dagger 3}a_4^\dagger a_3^2 - \frac{25}{8}a_1^\dagger a_2^{\dagger 2}a_3^{\dagger 2}a_4^\dagger a_3^2 - \\
&\frac{3}{8}a_1^{\dagger 4}a_4^{\dagger 2}a_3^2 + \frac{3}{8}a_3^{\dagger 4}a_4^{\dagger 2}a_3^2 - \frac{67}{8}a_1^\dagger a_3^{\dagger 2}a_1a_3^2 - \frac{1}{8}a_1^{\dagger 2}a_2^\dagger a_3^{\dagger 2}a_1a_3^2 - \frac{11}{4}a_1^\dagger a_3^{\dagger 3}a_4^\dagger a_1a_3^2 - \frac{1}{8}a_1^{\dagger 2}a_3^{\dagger 2}a_4^{\dagger 2}a_3^2 - \frac{63}{8}a_2^\dagger a_3^{\dagger 2}a_2a_3^2 + \frac{1}{8}a_1^\dagger a_2^{\dagger 2}a_3^{\dagger 2}a_2a_3^2 - \frac{11}{4}a_2^\dagger a_3^{\dagger 3}a_4^\dagger a_2a_3^2 - \\
&\frac{3}{8}a_1^{\dagger 3}a_4^{\dagger 2}a_2a_3^2 - \frac{37}{4}a_3^{\dagger 2}a_1a_2a_3^2 - \frac{25}{8}a_3^{\dagger 3}a_4^\dagger a_1a_2a_3^2 - \frac{1}{8}a_1^\dagger a_3^{\dagger 2}a_4^{\dagger 2}a_1a_2a_3^2 + \frac{1}{8}a_2^{\dagger 2}a_3^{\dagger 2}a_4^{\dagger 2}a_1a_2a_3^2 - \frac{9}{4}a_1^{\dagger 2}a_4^{\dagger 2}a_2a_3^2 + \frac{1}{8}a_2^\dagger a_3^{\dagger 2}a_1a_2^2a_3^2 - \frac{3}{2}a_1^\dagger a_4^{\dagger 2}a_2^2a_3^2 - \frac{3}{8}a_4^{\dagger 2}a_2^4a_3^2 + \\
&\frac{1}{8}a_3^{\dagger 3}a_3^3 - a_1^\dagger a_2^\dagger a_3^{\dagger 3}a_3^3 - \frac{3}{8}a_1^{\dagger 4}a_4^\dagger a_3^3 + \frac{1}{4}a_3^{\dagger 4}a_4^\dagger a_3^3 - \frac{7}{8}a_1^\dagger a_3^{\dagger 3}a_1a_3^3 - \frac{7}{8}a_2^\dagger a_3^{\dagger 3}a_2a_3^3 - \frac{5}{4}a_1^{\dagger 3}a_4^\dagger a_2a_3^3 - a_3^{\dagger 3}a_1a_2a_3^3 - \frac{3}{2}a_1^{\dagger 2}a_4^\dagger a_2^2a_3^3 - \frac{3}{8}a_1^\dagger a_4^{\dagger 2}a_2^2a_3^3 - \\
&\frac{1}{8}a_4^\dagger a_2^4a_3^3 - \frac{1}{8}a_1^{\dagger 4}a_3^\dagger + \frac{1}{16}a_3^{\dagger 4}a_3^\dagger - \frac{3}{8}a_1^{\dagger 3}a_2a_3^4 - \frac{3}{8}a_1^{\dagger 2}a_2^\dagger a_3^4 - \frac{1}{8}a_1^\dagger a_2^{\dagger 3}a_3^4 - \frac{1}{8}a_2^{\dagger 4}a_3^{\dagger 3}a_4 - 16\,a_1^\dagger a_4 - \frac{71}{2}a_1^\dagger a_2^\dagger a_4^\dagger a_4 - \frac{69}{8}a_1^{\dagger 2}a_2^{\dagger 2}a_4^\dagger a_4 - a_1^{\dagger 3}a_2^{\dagger 3}a_4^\dagger a_4 - \\
&\frac{31}{4}a_3^\dagger a_4^{\dagger 2}a_4 - \frac{75}{4}a_1^\dagger a_2^\dagger a_3^\dagger a_4^{\dagger 2}a_4 + \frac{1}{8}a_1^{\dagger 2}a_2^{\dagger 2}a_3^\dagger a_4^{\dagger 2}a_4 + \frac{1}{8}a_3^{\dagger 2}a_4^{\dagger 3}a_4 - \frac{13}{4}a_1^\dagger a_2^\dagger a_3^{\dagger 2}a_4^{\dagger 3}a_4 + \frac{1}{4}a_3^{\dagger 3}a_4^{\dagger 4}a_4 - \frac{3}{4}a_2^{\dagger 3}a_3^\dagger a_4^\dagger a_4 - \frac{65}{2}a_1^\dagger a_1^\dagger a_4 - \frac{33}{4}a_1^{\dagger 2}a_2^\dagger a_1^\dagger a_4 - \\
&\frac{23}{8}a_1^{\dagger 3}a_2^{\dagger 2}a_4^\dagger a_1a_4 - \frac{33}{2}a_1^\dagger a_3^\dagger a_4^{\dagger 2}a_1a_4 + \frac{1}{4}a_1^{\dagger 2}a_2^\dagger a_3^\dagger a_4^{\dagger 2}a_1a_4 - \frac{23}{8}a_1^\dagger a_3^{\dagger 2}a_4^{\dagger 3}a_1a_4 - \frac{3}{2}a_2^{\dagger 2}a_3^{\dagger 3}a_4^\dagger a_1a_4 - \frac{63}{8}a_1^{\dagger 2}a_4^\dagger a_1^2a_4 - \frac{11}{4}a_1^{\dagger 3}a_2^\dagger a_4^\dagger a_1^2a_4 + \frac{1}{8}a_1^{\dagger 2}a_3^\dagger a_4^{\dagger 2}a_1^2a_4 - \\
&\frac{5}{4}a_2^\dagger a_3^{\dagger 3}a_4^\dagger a_1^2a_4 - \frac{7}{8}a_1^{\dagger 3}a_4^\dagger a_2^3a_4 - \frac{3}{8}a_3^{\dagger 3}a_4^\dagger a_2^3a_4 - \frac{67}{2}a_2^\dagger a_4^\dagger a_2a_4 - 17\,a_1^\dagger a_2^{\dagger 2}a_4^\dagger a_2a_4 - \frac{23}{8}a_1^{\dagger 2}a_2^{\dagger 3}a_4^\dagger a_2a_4 - 17\,a_2^\dagger a_3^\dagger a_4^{\dagger 2}a_2a_4 - \frac{23}{8}a_2^\dagger a_3^{\dagger 3}a_4^\dagger a_2a_4 - \frac{71}{2}a_1^\dagger a_1a_2a_4 - \\
&\frac{67}{2}a_1^\dagger a_2^\dagger a_1^\dagger a_1a_2a_4 - \frac{17}{2}a_1^{\dagger 2}a_2^{\dagger 2}a_1^\dagger a_1a_2a_4 - \frac{77}{4}a_3^\dagger a_4^{\dagger 2}a_1a_2a_4 - \frac{13}{4}a_3^{\dagger 2}a_4^{\dagger 3}a_1a_2a_4 - \frac{33}{2}a_1^\dagger a_4^\dagger a_1^2a_2a_4 - \frac{67}{8}a_1^{\dagger 2}a_2^\dagger a_4^\dagger a_1^2a_2a_4 - \frac{11}{4}a_1^{\dagger 2}a_4^\dagger a_1^3a_2a_4 - \\
&\frac{67}{8}a_2^{\dagger 2}a_4^\dagger a_2^2a_4 - \frac{11}{4}a_1^\dagger a_2^{\dagger 3}a_4^\dagger a_2^2a_4 - \frac{1}{8}a_2^{\dagger 2}a_3^\dagger a_4^{\dagger 2}a_2^2a_4 - 17\,a_2^\dagger a_4^\dagger a_1a_2^2a_4 - \frac{67}{8}a_1^\dagger a_2^{\dagger 2}a_4^\dagger a_1a_2^2a_4 - \frac{1}{4}a_2^\dagger a_3^\dagger a_4^{\dagger 2}a_1a_2^2a_4 - \frac{69}{8}a_1^\dagger a_1^2a_2^2a_4 - \frac{17}{2}a_1^\dagger a_2^\dagger a_4^\dagger a_1^2a_2^2a_4 - \\
&\frac{1}{8}a_3^\dagger a_4^{\dagger 2}a_1^2a_2^2a_4 - \frac{23}{8}a_1^\dagger a_4^\dagger a_3^2a_2^2a_4 - \frac{7}{8}a_2^{\dagger 3}a_4^\dagger a_3^2a_2^2a_4 - \frac{11}{4}a_2^{\dagger 2}a_4^\dagger a_1a_3^2a_2^2a_4 - \frac{23}{8}a_2^\dagger a_4^\dagger a_1^2a_3^2a_2^2a_4 - a_4^\dagger a_1^3a_3^2a_2^2a_4 - 17\,a_3a_4 - \frac{77}{2}a_1^\dagger a_2^\dagger a_3a_4 - 10\,a_1^{\dagger 2}a_2^{\dagger 2}a_3a_4 - \\
&\frac{9}{8}a_1^{\dagger 3}a_2^{\dagger 3}a_3a_4 - \frac{31}{2}a_2^\dagger a_4^\dagger a_3a_4 - 38\,a_1^\dagger a_2^\dagger a_3^\dagger a_4^\dagger a_3a_4 + \frac{1}{2}a_2^{\dagger 2}a_4^{\dagger 2}a_3a_4 - \frac{77}{8}a_1^\dagger a_2^\dagger a_3^{\dagger 2}a_4^{\dagger 2}a_3a_4 + a_2^{\dagger 3}a_4^{\dagger 3}a_3a_4 - \frac{71}{2}a_1^\dagger a_1a_3a_4 - \frac{77}{4}a_1^{\dagger 2}a_2^\dagger a_1a_3a_4 - \\
&\frac{13}{4}a_1^{\dagger 3}a_2^{\dagger 2}a_1a_3a_4 - \frac{67}{2}a_1^\dagger a_3^\dagger a_4^\dagger a_1a_3a_4 - \frac{17}{2}a_1^\dagger a_3^{\dagger 2}a_4^{\dagger 2}a_1a_3a_4 - \frac{37}{4}a_1^{\dagger 2}a_1^2a_3a_4 - \frac{25}{8}a_1^{\dagger 3}a_2^\dagger a_1^2a_3a_4 - a_1^{\dagger 3}a_3^\dagger a_4^\dagger a_3a_4 - \frac{71}{2}a_2^\dagger a_2a_3a_4 - \frac{77}{4}a_1^\dagger a_2^{\dagger 2}a_2a_3a_4 - \\
&\frac{13}{4}a_1^{\dagger 2}a_2^{\dagger 3}a_2a_3a_4 - \frac{67}{2}a_2^\dagger a_3^\dagger a_4^\dagger a_2a_3a_4 - \frac{17}{2}a_2^\dagger a_3^{\dagger 2}a_4^{\dagger 2}a_2a_3a_4 - \frac{75}{2}a_1a_2a_3a_4 - 38\,a_1^\dagger a_2^\dagger a_1a_2a_3a_4 - \frac{77}{8}a_1^{\dagger 2}a_2^{\dagger 2}a_1a_2a_3a_4 - 38\,a_3^\dagger a_4^\dagger a_1a_2a_3a_4 - \\
&\frac{77}{8}a_3^{\dagger 2}a_4^{\dagger 2}a_1a_2a_3a_4 - \frac{75}{4}a_1^\dagger a_1^2a_2a_3a_4 - \frac{19}{2}a_1^{\dagger 2}a_2^\dagger a_1^2a_2a_3a_4 - \frac{25}{8}a_1^{\dagger 2}a_3^\dagger a_2a_3a_4 - \frac{37}{4}a_2^{\dagger 2}a_2^2a_3a_4 - \frac{25}{8}a_1^\dagger a_2^{\dagger 3}a_2^2a_3a_4 - \frac{75}{4}a_2^\dagger a_1^\dagger a_2^2a_3a_4 - \frac{19}{2}a_1^\dagger a_2^{\dagger 2}a_1^\dagger a_2^2a_3a_4 - \\
&\frac{19}{2}a_1^2a_2^2a_3a_4 - \frac{77}{8}a_1^\dagger a_2^\dagger a_1^2a_2^2a_3a_4 - \frac{13}{4}a_1^\dagger a_3^\dagger a_2^2a_3a_4 - a_2^{\dagger 3}a_3^2a_3a_4 - \frac{25}{8}a_2^{\dagger 2}a_1a_2^2a_3a_4 - \frac{13}{4}a_2^\dagger a_1^\dagger a_2^2a_3a_4 - \frac{9}{8}a_1^3a_2^2a_3a_4 - \frac{31}{4}a_2^\dagger a_3^\dagger a_4 - \frac{77}{4}a_1^\dagger a_2^\dagger a_3^\dagger a_4^2 - \\
&\frac{2}{8}a_1^{\dagger 2}a_2^{\dagger 2}a_3^\dagger a_3^2a_4 + \frac{5}{8}a_2^{\dagger 2}a_4^\dagger a_3^2a_4 - \frac{19}{2}a_1^\dagger a_2^\dagger a_3^{\dagger 2}a_4^\dagger a_3^2a_4 + \frac{3}{2}a_3^{\dagger 3}a_4^{\dagger 2}a_3^2a_4 - 17\,a_1^\dagger a_3^\dagger a_1a_2^2a_4 - \frac{1}{4}a_1^{\dagger 2}a_2^\dagger a_3^\dagger a_1a_2^2a_4 - \frac{67}{8}a_1^\dagger a_3^{\dagger 2}a_4^\dagger a_1a_2^2a_4 - \frac{1}{8}a_1^{\dagger 2}a_3^\dagger a_4^{\dagger 2}a_1a_2^2a_4 - \\
&\frac{33}{2}a_2^\dagger a_3^\dagger a_2a_3^2a_4 - \frac{67}{8}a_1^\dagger a_2^\dagger a_3^\dagger a_4^\dagger a_2a_3^2a_4 - \frac{75}{4}a_3^\dagger a_1a_2a_3^2a_4 - \frac{19}{2}a_3^{\dagger 2}a_4^\dagger a_1a_2a_3^2a_4 + \frac{1}{8}a_2^{\dagger 2}a_3^\dagger a_4^{\dagger 2}a_1a_2a_3^2a_4 + \frac{1}{4}a_2^\dagger a_3^\dagger a_1a_2^2a_3^2a_4 + \frac{1}{8}a_3^\dagger a_4^{\dagger 2}a_1a_2^2a_3^2a_4 + \frac{1}{4}a_3^{\dagger 2}a_3^3a_4 - \\
&\frac{25}{8}a_1^\dagger a_2^\dagger a_3^{\dagger 2}a_3^3a_4 + a_3^{\dagger 3}a_4^\dagger a_3^3a_4 - \frac{11}{4}a_1^\dagger a_3^{\dagger 2}a_1a_3^3a_4 - \frac{11}{4}a_2^\dagger a_3^{\dagger 2}a_2a_3^3a_4 - \frac{25}{8}a_3^{\dagger 2}a_1a_2a_3^3a_4 + \frac{1}{4}a_3^{\dagger 3}a_3^4a_4 - \frac{3}{8}a_2^{\dagger 4}a_3^\dagger a_4^\dagger a_4 - \frac{29}{8}a_4^{\dagger 2}a_4^2 - \frac{37}{4}a_1^\dagger a_2^\dagger a_4^{\dagger 2}a_4^2 + \frac{1}{4}a_3^\dagger a_4^{\dagger 3}a_4^2 - \\
&\frac{25}{8}a_1^\dagger a_2^\dagger a_3^\dagger a_4^{\dagger 3}a_4^2 + \frac{3}{8}a_3^{\dagger 2}a_4^{\dagger 4}a_4^2 - \frac{3}{2}a_2^{\dagger 3}a_3^{\dagger 2}a_1a_4^2 - \frac{63}{8}a_1^\dagger a_4^{\dagger 2}a_1a_4^2 + \frac{1}{8}a_1^{\dagger 2}a_2^\dagger a_4^{\dagger 2}a_1a_4^2 - \frac{1}{8}a_1^{\dagger 2}a_4^{\dagger 2}a_2^\dagger a_4^2 - \frac{3}{2}a_2^\dagger a_3^{\dagger 2}a_4^{\dagger 2}a_1a_4^2 - \\
&\frac{3}{8}a_3^{\dagger 2}a_4^\dagger a_1^2a_4^2 - \frac{67}{8}a_2^\dagger a_4^{\dagger 2}a_2a_4^2 - \frac{1}{8}a_1^\dagger a_2^{\dagger 2}a_4^{\dagger 2}a_2a_4^2 - \frac{11}{4}a_2^\dagger a_3^\dagger a_4^{\dagger 3}a_2a_4^2 - \frac{37}{4}a_1^{\dagger 2}a_1a_2a_4^2 - \frac{25}{8}a_1^\dagger a_4^{\dagger 3}a_1a_2a_4^2 + \frac{1}{8}a_1^\dagger a_4^\dagger a_1^2a_2a_4^2 - \frac{1}{8}a_2^{\dagger 2}a_4^{\dagger 2}a_2^2a_4^2 - \frac{1}{8}a_2^\dagger a_4^{\dagger 2}a_1a_2^2a_4^2 - \\
&\frac{31}{4}a_1^\dagger a_3a_4^2 - \frac{77}{4}a_1^\dagger a_2^\dagger a_4^\dagger a_3a_4^2 - \frac{1}{8}a_1^{\dagger 2}a_2^{\dagger 2}a_4^\dagger a_3a_4^2 + \frac{5}{8}a_3^\dagger a_4^{\dagger 2}a_3a_4^2 - \frac{19}{2}a_1^\dagger a_2^\dagger a_3^\dagger a_4^\dagger a_3a_4^2 + \frac{3}{2}a_3^{\dagger 2}a_4^{\dagger 3}a_3a_4^2 - \frac{33}{2}a_1^\dagger a_4^\dagger a_1a_3a_4^2 - \frac{67}{8}a_1^\dagger a_3^\dagger a_4^{\dagger 2}a_1a_3a_4^2 + \\
&\frac{1}{8}a_1^{\dagger 2}a_4^\dagger a_2^\dagger a_3a_4^2 - 17\,a_2^\dagger a_4^\dagger a_2a_3a_4^2 - \frac{1}{4}a_1^\dagger a_2^{\dagger 2}a_4^\dagger a_2a_3a_4^2 - \frac{67}{8}a_2^\dagger a_3^\dagger a_4^{\dagger 2}a_2a_3a_4^2 - \frac{75}{4}a_1^\dagger a_1a_2a_3a_4^2 - \frac{19}{2}a_3^\dagger a_4^{\dagger 2}a_1a_2a_3a_4^2 + \frac{1}{4}a_1^\dagger a_4^\dagger a_1^2a_2a_3a_4^2 - \frac{1}{8}a_2^{\dagger 2}a_4^\dagger a_1^2a_2a_3a_4^2 + \\
&\frac{1}{8}a_4^\dagger a_1^2a_2^2a_3a_4^2 - \frac{33}{8}a_2^\dagger a_4^2 - 10\,a_1^\dagger a_2^\dagger a_3^\dagger a_4^2 - \frac{1}{8}a_1^{\dagger 2}a_2^{\dagger 2}a_3^2a_4^2 + \frac{1}{2}a_3^\dagger a_4^\dagger a_3^2a_4^2 - \frac{77}{8}a_1^\dagger a_2^\dagger a_3^\dagger a_4^\dagger a_3^2a_4^2 + \frac{9}{4}a_3^{\dagger 2}a_4^{\dagger 2}a_3^2a_4^2 - \frac{69}{8}a_1^\dagger a_1a_3^2a_4^2 - \frac{1}{8}a_1^{\dagger 2}a_2^\dagger a_1a_3^2a_4^2 - \\
&\frac{17}{2}a_1^\dagger a_3^\dagger a_4^\dagger a_1a_2^2a_3^2a_4^2 - \frac{69}{8}a_2^\dagger a_2a_3^2a_4^2 - \frac{1}{8}a_1^\dagger a_2^{\dagger 2}a_2a_3^2a_4^2 - \frac{17}{2}a_2^\dagger a_3^\dagger a_4^\dagger a_2a_3^2a_4^2 - \frac{19}{2}a_1a_2a_3^2a_4^2 - \frac{77}{8}a_3^\dagger a_4^\dagger a_1a_2a_3^2a_4^2 + \frac{1}{8}a_1^\dagger a_2^\dagger a_2a_3^2a_4^2 + \frac{1}{8}a_2^\dagger a_1a_2a_3^2a_4^2 + \frac{1}{8}a_1^\dagger a_2^\dagger a_2a_3^2a_4^2 + \\
&\frac{1}{8}a_3^\dagger a_3^2a_4^2 - \frac{13}{4}a_1^\dagger a_2^\dagger a_3^\dagger a_3^2a_4^2 + \frac{3}{2}a_3^{\dagger 2}a_4^\dagger a_3^2a_4^2 - \frac{23}{8}a_1^\dagger a_3^\dagger a_1a_3^2a_4^2 - \frac{3}{8}a_2^{\dagger 2}a_3^\dagger a_1a_3^2a_4^2 - \frac{1}{8}a_3^{\dagger 4}a_3^2a_4^2 + \frac{1}{4}a_1^{\dagger 2}a_3a_3^2a_4^2 - \frac{3}{8}a_2^{\dagger 2}a_1^2a_3^2a_4^2 + \\
&\frac{1}{4}a_3^\dagger a_4^{\dagger 4}a_3^2a_4^2 - \frac{5}{4}a_2^{\dagger 3}a_3^\dagger a_1a_3^3a_4^2 - \frac{7}{8}a_1^\dagger a_3^{\dagger 3}a_1a_3^3a_4^2 - \frac{3}{2}a_2^{\dagger 2}a_3^\dagger a_1^2a_3^3a_4^2 - \frac{3}{4}a_2^\dagger a_3^\dagger a_1^3a_3^3a_4^2 - \frac{1}{8}a_3^\dagger a_4^{\dagger 2}a_3^3a_4^2 - \frac{7}{8}a_2^\dagger a_4^{\dagger 2}a_3^3a_4^2 - a_4^{\dagger 3}a_1a_2a_3^3a_4^2 + \frac{1}{4}a_4^{\dagger 2}a_3a_3^3a_4^2 - \frac{25}{8}a_1^\dagger a_2^\dagger a_4^{\dagger 2}a_3a_3^3a_4^2 + \\
&a_3^\dagger a_4^{\dagger

Table A.1: Selection rules of the unperturbed Hamiltonian

	Δn_1	Δn_2	Δn_3	Δn_4		Δn_1	Δn_2	Δn_3	Δn_4		Δn_1	Δn_2	Δn_3	Δn_4
1	−5	−5	−1	−1	54	−1	−1	−1	−1	107	1	1	2	2
2	−5	−5	0	0	55	−1	−1	0	0	108	1	1	3	3
3	−5	−5	1	1	56	−1	−1	1	1	109	1	1	4	4
4	−5	−1	−1	−5	57	−1	−1	2	2	110	1	1	5	5
5	−5	−1	0	−4	58	−1	−1	3	3	111	1	5	−1	−5
6	−5	−1	1	−3	59	−1	−1	4	4	112	1	5	0	−4
7	−5	−1	2	−2	60	−1	−1	5	5	113	1	5	1	−3
8	−5	−1	3	−1	61	−1	3	−1	−5	114	1	5	2	−2
9	−5	−1	4	0	62	−1	3	0	−4	115	1	5	3	−1
10	−5	−1	5	1	63	−1	3	1	−3	116	1	5	4	0
11	−4	−4	−1	−1	64	−1	3	2	−2	117	1	5	5	1
12	−4	−4	0	0	65	−1	3	3	−1	118	2	−2	−5	−1
13	−4	−4	1	1	66	−1	3	4	0	119	2	−2	−4	0
14	−4	0	−1	−5	67	−1	3	5	1	120	2	−2	−3	1
15	−4	0	0	−4	68	0	−4	−5	−1	121	2	−2	−2	2
16	−4	0	1	−3	69	0	−4	−4	0	122	2	−2	−1	3
17	−4	0	2	−2	70	0	−4	−3	1	123	2	−2	0	4
18	−4	0	3	−1	71	0	−4	−2	2	124	2	−2	1	5
19	−4	0	4	0	72	0	−4	−1	3	125	2	2	−2	−2
20	−4	0	5	1	73	0	−4	0	4	126	2	2	−1	−1
21	−3	−3	−1	−1	74	0	−4	1	5	127	2	2	0	0
22	−3	−3	0	0	75	0	0	−5	−5	128	2	2	1	1
23	−3	−3	1	1	76	0	0	−4	−4	129	2	2	2	2
24	−3	1	−1	−5	77	0	0	−3	−3	130	3	−1	−5	−1
25	−3	1	0	−4	78	0	0	−2	−2	131	3	−1	−4	0
26	−3	1	1	−3	79	0	0	−1	−1	132	3	−1	−3	1
27	−3	1	2	−2	80	0	0	0	0	133	3	−1	−2	2
28	−3	1	3	−1	81	0	0	1	1	134	3	−1	−1	3
29	−3	1	4	0	82	0	0	2	2	135	3	−1	0	4
30	−3	1	5	1	83	0	0	3	3	136	3	−1	1	5
31	−2	−2	−2	−2	84	0	0	4	4	137	3	3	−1	−1
32	−2	−2	−1	−1	85	0	0	5	5	138	3	3	0	0
33	−2	−2	0	0	86	0	4	−1	−5	139	3	3	1	1
34	−2	−2	1	1	87	0	4	0	−4	140	4	0	−5	−1
35	−2	−2	2	2	88	0	4	1	−3	141	4	0	−4	0
36	−2	2	−1	−5	89	0	4	2	−2	142	4	0	−3	1
37	−2	2	0	−4	90	0	4	3	−1	143	4	0	−2	2
38	−2	2	1	−3	91	0	4	4	0	144	4	0	−1	3
39	−2	2	2	−2	92	0	4	5	1	145	4	0	0	4
40	−2	2	3	−1	93	1	−3	−5	−1	146	4	0	1	5
41	−2	2	4	0	94	1	−3	−4	0	147	4	4	−1	−1
42	−2	2	5	1	95	1	−3	−3	1	148	4	4	0	0
43	−1	−5	−5	−1	96	1	−3	−2	2	149	4	4	1	1
44	−1	−5	−4	0	97	1	−3	−1	3	150	5	1	−5	−1
45	−1	−5	−3	1	98	1	−3	0	4	151	5	1	−4	0
46	−1	−5	−2	2	99	1	−3	1	5	152	5	1	−3	1
47	−1	−5	−1	3	100	1	1	−5	−5	153	5	1	−2	2
48	−1	−5	0	4	101	1	1	−4	−4	154	5	1	−1	3
49	−1	−5	1	5	102	1	1	−3	−3	155	5	1	0	4
50	−1	−1	−5	−5	103	1	1	−2	−2	156	5	1	1	5
51	−1	−1	−4	−4	104	1	1	−1	−1	157	5	5	−1	−1
52	−1	−1	−3	−3	105	1	1	0	0	158	5	5	0	0
53	−1	−1	−2	−2	106	1	1	1	1	159	5	5	1	1

Appendix B

Some simple integrable 2D systems

B.1 Eigenfunctions of the 2D harmonic oscillator

In this section we focus on the coordinate representation of the wave functions of the 2D harmonic oscillator. They are used in section (B.2), to find the representation of the tensorial product $|n_1 n_2\rangle$ of Fock states, and through this, to calculate the wave functions of driven 2D helium.

We start with the Hamiltonian of the 2D harmonic oscillator $H = -\frac{1}{2}\nabla^2 + \frac{1}{2}\omega^2 r^2$, where ∇^2 is the two dimensional Laplacian. Scaling the Cartesian coordinates by $r \to \sqrt{\omega} r$, the scaled Hamiltonian $H \to H/\omega$ reads

$$H = -\frac{1}{2}\nabla^2 + \frac{1}{2}r^2. \tag{B.1}$$

Now we proceed to solve the eigenvalue problem for this Hamiltonian. For that purpose we choose polar coordinates (ρ, ϕ). Thus the Schrödinger equation takes the form

$$\left(\frac{\partial^2}{\partial\rho^2} + \frac{1}{\rho}\frac{\partial}{\partial\rho} + \frac{1}{\rho^2}\frac{\partial^2}{\partial\phi^2} - \rho^2\right)\psi(\rho,\phi) = -2E\psi(\rho,\phi). \tag{B.2}$$

This equation is separable [116] and the angular part of the solutions is given by eigenfunctions $e^{im\phi}$ $(m \in \mathbb{Z})$ of the angular momentum $L_z = -i\partial/\partial\phi$. Therefore, writing the radial part of ψ as $g(\rho)/\sqrt{\rho}$, the function g satisfies

the following differential equation:

$$g''(\rho) + \left(\frac{\frac{1}{4} - m^2}{\rho^2} - \rho^2 + 2E \right) g(\rho) = 0. \tag{B.3}$$

The solutions of this equation in terms of the Laguerre polynomials $L_n^{(|m|)}(\rho^2)$ are [71]

$$\left\{ \begin{array}{rcll} g(\rho) & = & e^{\rho^2/2}\, \rho^{|m|+1/2}\, L_n^{((|m|))}(\rho^2), & \\ E & = & 2n + |m| + 1, & \text{with } n = 0, 1, 2, \ldots . \end{array} \right. \tag{B.4}$$

Consequently, the normalized eigenfunctions of the 2D harmonic oscillator of frequency ω are given by

$$\left\{ \begin{array}{rcll} \psi(\rho, \phi) & = & \sqrt{\frac{\omega}{\pi}} \sqrt{\frac{n!}{(n+|m|)!}}\, e^{im\phi}\, (\sqrt{\omega}\rho)^{|m|}\, e^{-\omega\rho^2/2}\, L_n^{(|m|)}(\omega\rho^2), & \\ E & = & 2n + |m| + 1, & \text{with } m \in \mathbb{Z} \text{ and } n = 0, 1, 2, ... \end{array} \right. \tag{B.5}$$

B.2 2D hydrogen atom

In this part of the appendix, we discuss the most important features of the two dimensional hydrogen atom represented in parabolic coordinates, in particular its symmetries. The essential ideas which we outline here are crucial for our treatment of the 2D helium atom in chapter 2.

The Hamiltonian of the two dimensional hydrogen atom in atomic units reads

$$H = \frac{1}{2}(p_x^2 + p_y^2) - \frac{Z}{r}. \tag{B.6}$$

In parabolic coordinates, defined in (A.1), the Laplacian and the radius take the form $\nabla^2 = \partial_x^2 + \partial_y^2 = (\partial_\mu^2 + \partial_\nu^2)/(\mu^2 + \nu^2)$ and $r = (\mu^2 + \nu^2)/2$, respectively, and the Schrödinger equation $H|\psi\rangle = E|\psi\rangle$ can be regularized by multiplication with the Jacobian $2r$:

$$\left(-\frac{1}{2} \left(\frac{\partial^2}{\partial\mu^2} + \frac{\partial^2}{\partial\nu^2} \right) - 2Z \right) \psi(\mu, \nu) = E(\mu^2 + \nu^2)\psi(\mu, \nu). \tag{B.7}$$

This can be rewritten as

$$(H_\mu(\omega_E) + H_\nu(\omega_E))\psi(\mu,\nu) = 2Z\psi(\mu,\nu), \tag{B.8}$$

where $H_\mu(\omega_E) = \frac{1}{2}p_\mu^2 + \omega_E^2\mu^2/2$ and $H_\nu(\omega_E) = \frac{1}{2}p_\nu^2 + \omega_E^2\nu^2/2$ are two harmonic oscillators with frequency

$$\omega_E = \sqrt{-2E}. \tag{B.9}$$

Therefore, an eigenfunction of (B.6) can be written as a product of harmonic oscillator eigenfunctions

$$\psi(\mu,\nu) = \phi_{n_\mu}(\mu)\phi_{n_\nu}(\nu), \tag{B.10}$$

where $n_\mu, n_\nu = 0, 1, 2, \ldots$, and the harmonic oscillator frequency ω_E is determined by the eigenenergy E.

Substituting (B.10) in (B.8), and evaluating the harmonic oscillator eigenvalue equation yields $\omega_E(n_\mu + n_\nu + 1) = 2Z$, and this implies for the eigenvalues of (B.7), with (B.9):

$$E_{n_\mu,n_\nu} = -\frac{2Z^2}{(n_\mu + n_\nu + 1)^2}. \tag{B.11}$$

But not all of these are actually eigenvalues of (B.6) since the double representation in parabolic coordinates (s. fig. (2.3)) introduces unphysical symmetries. Each physical solution must be uniquely defined in the Cartesian plane and, therefore, must satisfy $\psi(\mu,\nu) = \psi(-\mu,-\nu)$. Thus, since the parity of a harmonic oscillator wave function $\phi_n(x)$ is $(-1)^n$ (i.e., $\phi_n(-x) = (-1)^n\phi_n(x)$) [39], then $\psi(-\mu,-\nu) = (-1)^{n_\mu+n_\nu}\psi(\mu,\nu)$. It follows that for the physical solutions of (B.6) $n_\mu + n_\nu$ is an even integer. Consequently, we can label the eigenstates of 2D hydrogen by the integer number

$$N = \frac{1}{2}(n_\mu + n_\nu). \tag{B.12}$$

Finally, from (B.11), the eigenvalues of the 2D hydrogen atom become

$$E_N = -\frac{Z^2}{2(N+\frac{1}{2})^2}, \qquad \text{with } N = 0, 1, 2, \ldots. \tag{B.13}$$

Representation in creation and annihilation operators

For $\omega > 0$, let us consider the operators

$$\begin{aligned} a_u^\dagger(\omega) &= \frac{1}{\sqrt{2}}\left(\sqrt{\omega}u - i\frac{p_u}{\sqrt{\omega}}\right) \\ a_u(\omega) &= \frac{1}{\sqrt{2}}\left(\sqrt{\omega}u + i\frac{p_u}{\sqrt{\omega}}\right). \end{aligned} \tag{B.14}$$

They are the creation and annihilation operators of a harmonic oscillator with frequency ω. Hence, the number operator $N_u(\omega) = a_u^\dagger(\omega)a_u(\omega)$ is related to the corresponding Hamiltonian $H_u(\omega) = p_u^2/2 + \omega^2 u^2/2$ by the relation

$$H_u(\omega) = \omega\left(N_u(\omega) + \frac{1}{2}\right). \tag{B.15}$$

Coming back to the 2D hydrogen atom in parabolic coordinates, we consider the creation and annihilation operators $a_\mu^\dagger$, a_μ, $a_\nu^\dagger$ and a_ν for $H_\mu(\omega)$ and $H_\nu(\omega)$ (ω is not necessarily equal to ω_E here), and we define the circular operators

$$\begin{aligned} a_1 &= (a_\mu - ia_\nu)/\sqrt{2}, \\ a_2 &= (a_\mu + ia_\nu)/\sqrt{2}, \end{aligned} \tag{B.16}$$

which satisfy the usual commutation relations for creation and annihilation operators [39]:

$$[a_i, a_j] = 0, \qquad [a_i^\dagger, a_j^\dagger] = 0, \qquad [a_i, a_j^\dagger] = \delta_{ij}, \quad \text{for } i = 1, 2. \tag{B.17}$$

The number operators $N_1 = a_1^\dagger a_1$ and $N_2 = a_2^\dagger a_2$ expressed as functions of the creation and annihilation operators $a_\mu^\dagger$, a_μ, $a_\nu^\dagger$ and a_ν are given by

$$\begin{aligned} N_1 &= \frac{1}{2}(a_\mu^\dagger a_\mu + a_\nu^\dagger a_\nu) + \frac{i}{2}(a_\nu^\dagger a_\mu - a_\mu^\dagger a_\nu) \\ N_2 &= \frac{1}{2}(a_\mu^\dagger a_\mu + a_\nu^\dagger a_\nu) - \frac{i}{2}(a_\nu^\dagger a_\mu - a_\mu^\dagger a_\nu), \end{aligned} \tag{B.18}$$

and the expression for $N_1 + N_2$ in terms of the number operators of the harmonic oscillators $H_\mu(\omega)$ and $H_\nu(\omega)$ reads

$$\begin{aligned} N_1 + N_2 &= N_\mu + N_\nu, \\ N_1 - N_2 &= i(a_\nu^\dagger a_\mu - a_\mu^\dagger a_\nu). \end{aligned} \tag{B.19}$$

Hence, in the coordinates (μ, ν),

$$N_1 + N_2 = \frac{1}{\omega}\big(H_\mu(\omega) + H_\nu(\omega)\big) - 1, \tag{B.20}$$

$$N_1 - N_2 = \mu p_\nu - \nu p_\mu. \tag{B.21}$$

In particular, we see that $N_1 - N_2$ is independent of the frequency ω, and

$$L_z = \frac{1}{2}(N_1 - N_2), \tag{B.22}$$

where $L_z = xp_y - yp_x$ is the angular momentum of the 2D hydrogen atom.

The eigenvalue problem (B.8) also can be written in terms of the circular operators:

$$\left(-\frac{1}{2\omega}(-1 + a_1a_2 + a_1^\dagger a_2^\dagger - a_1^\dagger a_1 - a_2^\dagger a_2) - 2Z\right)|\psi\rangle = E\omega(1 + a_1a_2 + a_1^\dagger a_2^\dagger + a_1^\dagger a_1 + a_2^\dagger a_2)|\psi\rangle. \quad \text{(B.23)}$$

For the particular choice $\omega = \omega_E$, as expected from (B.20), this equation reduces to

$$\frac{1}{\omega_E}(N_1 + N_2 + 1)|\psi\rangle = 2Z|\psi\rangle, \quad \text{(B.24)}$$

and thus the eigenvectors are given by $|\psi\rangle = |n_1n_2\rangle^{(\omega_E)} = |n_1\rangle^{(\omega_E)} \otimes |n_2\rangle^{(\omega_E)}$, where $|n_i\rangle^{(\omega_E)}$ are the eigenstates of N_i, $i = 1, 2$. The energy E of the 2D hydrogen atom is again given by (B.13), but in this case $N = (n_1 + n_2)/2$. Thus the eigenfunctions of the 2D hydrogen atom are $|n_1n_2\rangle^{(\omega_E)}$, with $n_1 + n_2 = 2N$. Since there are $2N + 1$ ordered pairs of non-negative integer numbers (n_1, n_2) such that $n_1 + n_2 = 2N$, the degeneracy of the eigenvalues (B.13) is $2N + 1$.

Alternatively, we can use the quantum numbers N and L to label the quantum eigenstates of the 2D hydrogen atom: $H|\psi_{NL}\rangle = E_N|\psi_{NL}\rangle$ and $L_z|\psi_{NL}\rangle = L|\psi_{NL}\rangle$. From (B.12), (B.19) and (B.22) it follows that $-N \leq L \leq N$ (again this leads to the degeneracy $2N + 1$ of the energy levels).

If ω is any positive real number, $|\psi_{NL}\rangle$ takes the form

$$|\psi_{NL}\rangle = \sum_{n_1,n_2 \in \mathcal{B}_{NL}} c(n_1, n_2)|n_1n_2\rangle^{(\omega)}, \quad \text{(B.25)}$$

where $\mathcal{B}_{NL} = \{n_1, n_2 | n_1 + n_2 = 2N \text{ and } n_1 - n_2 = 2L\}$.

B.2.1 Coordinate representation of tensorial products of Fock states

To find the coordinate representation of a product state $|n_1n_2\rangle^{(\omega)}$, we notice that these are eigenstates of $N_1 + N_2$ and $L_z = \frac{1}{2}(N_1 - N_2)$, with eigenvalues $n_1 + n_2$ and $(n_1 - n_2)/2$. Therefore, since, in (B.20), $H_\mu(\omega) + H_\nu(\omega)$ is an isotropic two dimensional harmonic oscillator (in the space (μ, ν)), the eigenstates and the eigenvalues of $\omega(N_1 + N_2 + 1)$ have the form given in (B.5) (here, instead of (ρ, ϕ) we use (R, Φ), to distinguish polar coordinates

and parabolic coordinates (μ, ν), i.e., $R = \sqrt{\mu^2 + \nu^2}$, and $\Phi = \arctan(\nu/\mu)$). In addition, the quantum number m is the eigenvalue of the operator $-i\partial_\Phi = -i(\mu\partial_\nu - \nu\partial_\mu) = N_1 - N_2$. Thus, by direct comparison with (B.5), we have that

$$\begin{cases} n_1 + n_2 = 2n + |m| + 1 \\ n_1 - n_2 = m. \end{cases} \tag{B.26}$$

Hence, the coordinate representation of $|n_1 n_2\rangle^{(\omega)}$, i.e.,

$$\psi_{n_1 n_2}(R, \Phi) = \langle R\,\Phi | n_1 n_2 \rangle^{(\omega)},$$

is given by

$$\begin{cases} \psi_{n_1 n_2}(R, \Phi) = \sqrt{\dfrac{\omega}{\pi}} \sqrt{\dfrac{n!}{(n+|m|)!}}\, e^{im\Phi}\, (\sqrt{\omega} R)^{|m|}\, e^{-\omega R^2/2}\, L_n^{(|m|)}(\omega R^2), \\ \qquad\qquad n = \min\{n_1, n_2\} \\ \qquad\qquad m = n_1 - n_2. \end{cases} \tag{B.27}$$

B.2.2 Eigenfunctions of the 2D hydrogen atom

The eigenfunctions of the 2D hydrogen atom are given by (B.5), when $\omega = \omega_E = \sqrt{-2E_{n_1 n_2}}$, with (see (B.11))

$$E_{n_1 n_2} = -\frac{2Z^2}{(n_1 + n_2 + 1)^2}. \tag{B.28}$$

Notice also that these wave functions are normalized as eigenfunctions of the 2D harmonic oscillator of *fixed* frequency ω. However, here the frequency changes, and therefore the normalization constant is not the same for distinct energies. Additionally, if (ρ, ϕ) are the polar coordinates of the Cartesian coordinates (x, y), then $\Phi = \phi/2$ and $R = \sqrt{\mu^2 + \nu^2} = \sqrt{2\rho}$. Finally, since the angular momentum $L = (n_1 - n_2)/2$, then $L = m/2$. With these considerations, the expression for the normalized eigenfunctions of the 2D hydrogen atom reads

$$\begin{aligned} \psi_{NL}(r, \phi) &= \frac{Z}{N + \frac{1}{2}} \sqrt{\frac{(N - |L|)!}{\pi (N + |L|)! (N + \frac{1}{2})}}\, e^{iL\phi}\, u^{|L|}\, e^{-u/2}\, L_{N-|L|}^{(2|L|)}(u), \\ \text{where} \qquad u &= \frac{2Z}{N + \frac{1}{2}} \rho. \end{aligned} \tag{B.29}$$

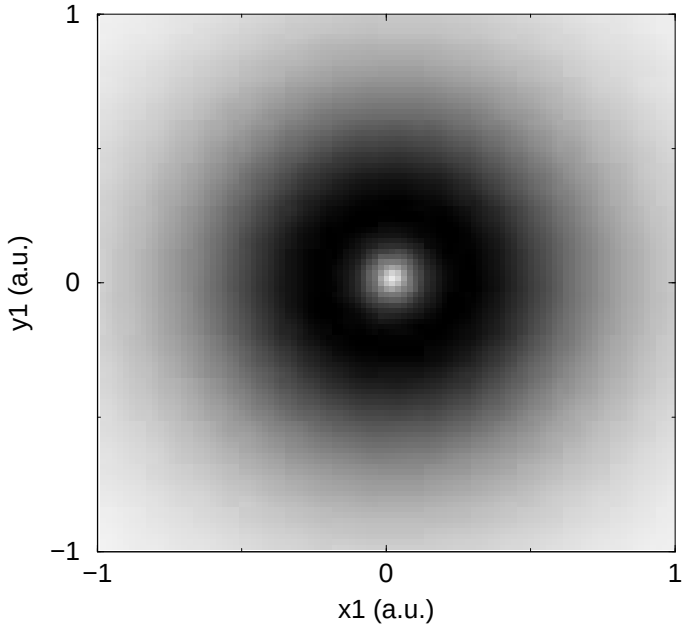

Figure B.1: Probability density of the ground state of the 2d hydrogen atom (the darker regions indicate larger densities).

In particular, the ground state of 2D hydrogen is given by

$$\psi_0(\rho,\phi) = \psi_{00}(\rho,\phi) = 2Z\sqrt{\frac{2}{\pi}}e^{-2Z\rho}, \tag{B.30}$$

and the corresponding probability density $r|\psi_0(r,\phi)|^2$ is shown in figure B.1, for $Z = 1$.

B.3 2D helium atom without electron-electron interaction

If the electron-electron interaction term $1/r_{12}$ is removed from the Hamiltonian (2.2) of the unperturbed 2D helium, the three body problem corresponds to two independent hydrogen atoms. Thus, from (B.13), the spectrum of 2D helium atom without electron-electron interaction is given by

$$E_{N_1,N_2,L_1,L_2} = -\frac{2}{(N_1-1/2)^2} - \frac{2}{(N_2-1/2)^2}, \tag{B.31}$$

as illustrated in figure B.2. Here, N_1 and N_2 are the principal quantum numbers of the two electrons, and L_1 and L_2 their angular momenta. The total angular momentum is given by $L = L_1 + L_2$, and the total degeneracy is $2(2N_1 - 1)(2N_2 - 1)$, if $N_1 \neq N_2$, or $(2N_1 - 1)^2$, if $N_1 = N_2$. The factor 2 in the $N_1 \neq N_2$ case comes from the particle exchange symmetry.

The single ionization thresholds (defined by the ionization of one electron) are given by the energies of the hydrogenic quantum states of the resulting He^+ ion:

$$I_N = -\frac{2}{(N - 1/2)^2}. \tag{B.32}$$

Consequently, the energy levels of 2D helium without electron-electron interaction are organized in series S_N of energies $E_{N,n} = E_{N,n,L_1,L_2}$, for a fixed value of the principal quantum number N of the inner electron, and variable $n = N, N+1, \ldots$. The threshold energies I_N of the series S_N converge to the double ionization threshold I_∞. Starting from the second series, i.e. doubly excited states, the discrete energy levels are immerged in the continuum of lower lying series.

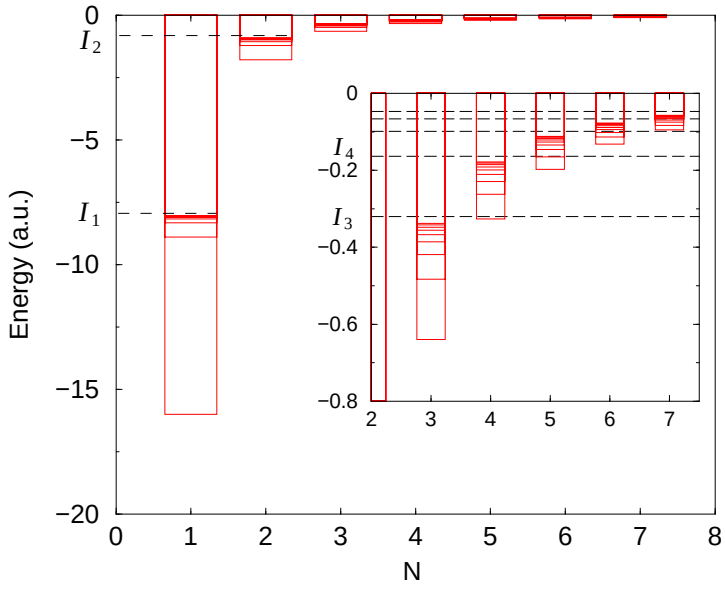

Figure B.2: Spectrum of 2D helium without electron-electron interaction. The energy levels (horizontal bars) are organized in series labeled by the principal quantum number N of the inner electron. The dashed lines are the single ionization thresholds of the respective series.

The ground state of 2D helium with neglected electron-electron interaction is simply the tensorial product of the ground states of the two independent 2D hydrogen atoms. Therefore, from (B.30) we have

$$\psi_0(r_1, r_2) = \frac{8}{\pi} Z^2 e^{-2Z(r_1+r_2)}. \tag{B.33}$$

Appendix C

On some useful identities in Floquet theory

In the extended space $\mathcal{L}^2(\mathbb{R}^d)\otimes\mathcal{L}^2(T)$,[1] time has to be treated as an additional coordinate – therefore the validity of the identities (2.43), for a given time t, is not obvious. The purpose of this appendix is to give a formal proof of these identities. To achieve this aim, we first prove the orthogonality relation (2.42) for the Fourier components of the Floquet states.

We start with the Schrödinger equation for the Floquet operator $\mathcal{H}_{\mathcal{F}} = H - i\partial/\partial t$ of a periodically time dependent Hamiltonian $H(\boldsymbol{r}, t)$ (with period T)

$$\mathcal{H}_F(\boldsymbol{r}, t)\phi_{\varepsilon_j}(\boldsymbol{r}, t) = \varepsilon_j\phi_{\varepsilon_j}(\boldsymbol{r}, t). \tag{C.1}$$

Now, for any integer number Δk and for any Floquet state $\phi_{\varepsilon_j}(\boldsymbol{r}, t)$

$$\mathcal{H}_F\,\left(e^{i\Delta k\,\omega t}\phi_{\varepsilon_j}(\boldsymbol{r}, t)\right) = (\varepsilon_j + \Delta k\,\omega)e^{i\Delta k\,\omega}\phi_{\varepsilon_j}(\boldsymbol{r}, t), \tag{C.2}$$

where $\omega = 2\pi/T$. Hence, $e^{i\Delta k\,\omega t}\phi_{\varepsilon_j}(\boldsymbol{r}, t)$ is also an eigenfuction of the Floquet operator, with quasienergy $\varepsilon_j + \Delta k\,\omega$, i.e.,

$$e^{i\Delta k\,\omega t}\phi_{\varepsilon_j}(\boldsymbol{r}, t) = \phi_{\varepsilon_j+\Delta k\,\omega}(\boldsymbol{r}, t). \tag{C.3}$$

On the other hand, $\phi_{\varepsilon_j}(\boldsymbol{r}, t)$ and $\phi_{\varepsilon_j+\Delta k\,\omega}(\boldsymbol{r}, t)$ are periodically time dependent, therefore they can be expanded in Fourier series

$$\phi_{\varepsilon_j}(\boldsymbol{r}, t) = \sum_k e^{-ik\omega t}\phi^k_{\varepsilon_j}(\boldsymbol{r}), \tag{C.4}$$

$$\phi_{\varepsilon_j+\Delta k\,\omega}(\boldsymbol{r}, t) = \sum_{k'} e^{-ik'\omega t}\phi^{k'}_{\varepsilon_j+\Delta k\,\omega}(\boldsymbol{r}). \tag{C.5}$$

[1] d is the dimension of the configuration space of the periodically time dependent Hamiltonian $H(\boldsymbol{r}, t)$.

Comparing the last two expansions and using the equation (C.3), we obtain

$$\phi^{k+\Delta k}_{\varepsilon_j}(\boldsymbol{r}) = \phi^{k}_{\varepsilon_j+\Delta k\,\omega}(\boldsymbol{r}). \tag{C.6}$$

Since the Floquet operator is a hermitian operator acting on the extended Hilbert space, its eigenfuctions are orthogonal. Therefore, for any pair of normalized eigenstates $\phi_{\varepsilon_i}(\boldsymbol{r},t)$ and $\phi_{\varepsilon_j}(\boldsymbol{r},t)$, we have

$$\frac{1}{T}\int dt\, d\boldsymbol{r}\, \phi^{*}_{\varepsilon_i}(\boldsymbol{r},t)\phi_{\varepsilon_j}(\boldsymbol{r},t) = \delta_{ij}, \tag{C.7}$$

where the integration over t has to be extended over one period T. Hence, after substituting the respective Fourier expansions of $\phi_{\varepsilon_i}(\boldsymbol{r},t)$ and $\phi_{\varepsilon_j}(\boldsymbol{r},t)$, we obtain

$$\sum_{k\,k'}\frac{1}{T}\int dt\, e^{-i(k-k')\omega t}\int d\boldsymbol{r}\, \phi^{k'}_{\varepsilon_i}(\boldsymbol{r})^{*}\phi^{k}_{\varepsilon_j}(\boldsymbol{r}) = \delta_{ij}. \tag{C.8}$$

The integration over t give us $\delta_{kk'}$, thus one of the sums in the equation (C.8) cancels and we obtain

$$\sum_{k}\int d\boldsymbol{r}\, \phi^{k}_{\varepsilon_i}(\boldsymbol{r})^{*}\phi^{k}_{\varepsilon_j}(\boldsymbol{r}) = \delta_{ij}, \tag{C.9}$$

which can be written, in Dirac notation, as

$$\sum_{k}\langle\phi^{k}_{\varepsilon_i}|\phi^{k}_{\varepsilon_j}\rangle = \delta_{ij}. \tag{C.10}$$

Let us now restrict to a single Floquet zone $\mathcal{F}_z$ (i.e. an interval of width ω on the energy axis). For any two quasienergies ε_i and ε_j in this Floquet zone, let us consider the left side of the identity (2.42):

$$\sum_{k}\langle\phi^{k+\Delta k}_{\varepsilon_i}|\phi^{k}_{\varepsilon_j}\rangle \tag{C.11}$$

If $\Delta k = 0$, the latter reduces to the left hand side of (C.10), and thus is equal to δ_{ij}. If $\Delta k \neq 0$, then from (C.6)

$$\sum_{k}\langle\phi^{k+\Delta k}_{\varepsilon_i}|\phi^{k}_{\varepsilon_j}\rangle = \sum_{k}\langle\phi^{k}_{\varepsilon_i+\Delta k\,\omega}|\phi^{k}_{\varepsilon_j}\rangle. \tag{C.12}$$

Since $\varepsilon_i+\Delta k\,\omega$ lies outside of the considered Floquet zone $\mathcal{F}_z$, whilst $\varepsilon_j \in \mathcal{F}_z$, it follows that $\varepsilon_i + \Delta k\,\omega \neq \varepsilon_j$, and thus, from (C.10), the expression (C.11) vanishes. Summarizing, we obtain (2.42):

$$\sum_{k}\langle\phi^{k+\Delta k}_{\varepsilon_i}|\phi^{k}_{\varepsilon_j}\rangle = \delta_{ij}\delta_{\Delta k,0}. \tag{C.13}$$

Finally let us consider the scalar product $\langle\phi_{\varepsilon_i}(t)|\phi_{\varepsilon_j}(t)\rangle$ of the two Floquet states with $\varepsilon_i, \varepsilon_j \in \mathcal{F}_z$. Using (C.13) it follows

$$\begin{aligned}\langle\phi_{\varepsilon_i}(t)|\phi_{\varepsilon_j}(t)\rangle &= \int d\boldsymbol{r}\phi^*_{\varepsilon_i}(\boldsymbol{r},t)\phi_{\varepsilon_j}(\boldsymbol{r},t) \\ &= \sum_{k\,k'} e^{-i\omega(k-k')t}\langle\phi^{k'}_{\varepsilon_i}|\phi^{k}_{\varepsilon_j}\rangle \\ &= \sum_{\Delta k} e^{-i\omega\Delta k\,t}\sum_{k'}\langle\phi^{k'}_{\varepsilon_i}|\phi^{k'+\Delta k}_{\varepsilon_j}\rangle \\ &= \delta_{ji} \qquad\qquad (C.14)\end{aligned}$$

Thus, at any given time t, the Floquet states within a given Floquet zone are orthogonal.

Bibliography

[1] Einstein, A. *Verh. Dtsch. Phys. Ges.* **19**, 82 (1917).

[2] Gutzwiller, M. C. *J. Math. Phys.* **8**, 1979 (1967).

[3] Gutzwiller, M. C. *J. Math. Phys.* **12**, 343 (1971).

[4] Ezra, G. S., Richter, K., Tanner, G., and Wintgen, D. *J. Phys. B* **24**, L413 (1991).

[5] Wintgen, D., Richter, K., and Tanner, G. *Chaos* **2**, 19 (1992).

[6] Tanner, G., Richter, K., and Rost, J. M. *Rev. Mod. Phys.* **72**, 497 (2000).

[7] Fittinghoff, D. N., Bolton, P. R., Chang, B., and Kulander, K. C. *Phys. Rev. Lett.* **69**, 2642 (1992).

[8] Walker, B., Sheehy, B., DiMauro, L., Agostini, P., Schafer, K., and Kulander, K. *Phys. Rev. Lett.* **73**, 1227 (1994).

[9] Schafer, K. J., Yang, B., DiMauro, L. F., and Kulander, K. C. *Phys. Rev. Lett.* **70**, 1599 (1993).

[10] Yang, B., Schafer, K. J., Walker, B., Kulander, K. C., Agostini, P., and DiMauro, L. F. *Phys. Rev. Lett.* **71**, 3770 (1993).

[11] Corkum, P. B. *Phys. Rev. Lett.* **71**, 1994 (1993).

[12] Becker, A. and Faisal, F. H. M. *Phys. Rev. Lett.* **84**, 3546 (2000).

[13] Weber, T., Giessen, H., Weckenbrock, M., Urbash, G., Staudte, A., Spielberger, L., Jagutzki, O., Mergel, V., Vollmer, M., and Döner, R. *Nature* **405**, 658 (2000).

[14] Moshammer, R., Feuerstein, B., López-Urrutia, J. C., Deipenwisch, J., Dorn, A., Fischer, D., Höhr, C., Neumayer, P., Schröter, C. D., Ullrich, J., Rottke, H., Trump, C., Wittmann, M., Korn, G., and Sandner, W. *Phys. Rev A* **65**, 035401 (2002).

[15] de Jesus, V. L. B., Feuerstein, B., Zrost, K., Fischer, D., Rudenko, A., Afaneh, F., Schröter, C. D., Moshammer, R., and Ullrich, J. *J. Phys. B: Atom. Mol. Opt. Phys. in press* (2004).

[16] Richter, K. and Wintgen, D. *Phys Rev Lett* **65**, 1965 (1990).

[17] Richter, K., Briggs, J. S., Wintgen, D., and Solovev, E. A. *J. Phys. B* **25**, 3929 (1992).

[18] Buchleitner, A., Delande, D., and Zakrzewski, J. *Phys. Rep.* **368**, 409 (2002).

[19] Schlagheck, P. and Buchleitner, A. *Eur. Phys. J. D* **22**, 401 (2003).

[20] Maeda, H. and Gallagher, T. F. *Phys. Rev. Lett.* **92**, 133004 (2004).

[21] Bürgers, A., Wintgen, D., and Rost, J. M. *J. Phys. B: Atom. Mol. Opt. Phys.* **28**, 3163 (1995).

[22] Grémaud, B. and Delande, D. *Europhys. Lett.* **40**, 363 (1997).

[23] Grosges, T., Piraux, B., and Shakeshaft, R. *Phys. Rev. A* **59**, 3088 (1999).

[24] Korobov, V. I. *Phys. Rev. A* **61**, 064503 (2000).

[25] Goldman, S. P. *Phys. Rev. A* **57**, R677 (1998).

[26] Taylor, K., Parker, J., Meharg, K., and Dundas, D. *Eur. Phys. J. D* **26**, 67 (2003).

[27] Lambropoulos, P., Maragakis, P., and Zhang, J. *Phys. Rep.* **203**, 305 (1998).

[28] Scrinzi, A. and Piraux, B. *Phys. Rev. Lett.* **71**, 3943 (1993).

[29] Purvis, J., Dörr, M., Terao-Dunseth, M., Joachain, C. J., Burke, P. G., and Noble, C. J. *Phys. Rev. Lett.* **71**, 3943 (1993).

[30] Sacha, K. and Eckhardt, B. *Phys. Rev. A* **63**, 043414 (2001).

[31] Stébé, B. and Ainane, A. *Superlattices and Microstruct.* **5**, 545 (1989).

[32] Kheng, K., Cox, R. T., d'Aubigné, M. Y., Bassani, F., Saminadayar, K., and Tatarenko, S. *Phys. Rev. Lett.* **71**, 1752 (1993).

[33] Finkelstein, G., Shtrikman, H., and Bar-Joseph, I. *Phys. Rev. Lett.* **74**, 976 (1995).

[34] Buhmann, H., Mansouri, L., Wang, J., Beton, P. H., Mori, N., Eaves, L., Henini, M., and Potemski, M. *Phys. Rev. B* **51**, 7969 (1995).

[35] Shields, A., Pepper, M., Ritchie, D., Simmons, M., and Jones, G. *Phys. Rev. B* **51**, 18049 (1995).

[36] Paganotto, N., Siviniant, J., Coquillat, D., Scalbert, D., Lascaray, J.-P., and Kavokin, A. V. *Phys. Rev. B* **58**, 4082 (1998).

[37] Nazmitdinov, R. G., Simonovi, N. S., and Rost, J. M. *Phys. Rev. B* **65**, 155307 (2002).

[38] Hilico, L., Grémaud, B., Jonckheere, T., Billy, N., and Delande, D. *Phys Rev A* **66**, 022101 (2002).

[39] Cohen-Tanoudji, C., Diu, B., and Laloë, F. *Quantum Mechanics.* Ed. John Wiley & Sons, Inc., Paris, (1977).

[40] Leopold, J. G. and Percival, L. C. *Phys Rev Lett* **41**, 944 (1978).

[41] Percival, I. C. *Proc. R. Soc. Lond. A* **353**, 289 (1977).

[42] Loudon, R. *The quantum theory of light.* Clarendon Press, Oxford, (1984).

[43] Altmann, S. L. and Herzig, P. *Point group theory tables.* Oxford University Press, Oxford, (1994).

[44] Cornwell, J. F. *Selected topics in solid state physics, Vol. X: Group theory and electronic energy bands in solids.* North-Holland publishing Co., Amsterdam, (1969).

[45] Landau, L. and Lifchitz, E. *Quantum Mechanics.* Ed. Mir, Moscow, (1966).

[46] Englefield, M. J. *Group theory and the Coulomb problem.* Wiley, New York, (1962).

[47] Barut, A. O. and Raczka, R. *Theory of group representations and aplications*. World Scientific Publishing Co., Singapure, (1986).

[48] Floquet, M. G. *Annales de l'École Normale Supérieure* **12**, 47 (1883).

[49] Shirley, J. H. *Phys. Rev.* **138**, B979 (1965).

[50] Zeldovich, Y. B. *JETP (Soviet Physics)* **24**, 1006 (1967).

[51] Breuer, H. P. and Holthaus, M. *Phys. Lett. A* **140**, 507 (1989).

[52] Breuer, H. P., Dietz, K., and Holthaus, M. *Phys. Rev. A* **45**, 550 (1992).

[53] Ibach, H. and Lüth, H. *Solid state physics: an introduction to principles of material science*. Springer, Berlin, (1996).

[54] Delande, D. and Zakrzewski, J. *Phys. Rev. A* **58**, 466 (1998).

[55] Graffi, S., Grecchi, V., and Silverstone, H. J. *Ann. Inst. Henry Poincaré* **42**, 205 (1985).

[56] Yajima, K. *Commun. Math. Phys.* **87**, 331 (1982).

[57] Aguilar, J. and Combes, J. M. *Commun. Math. Phys.* **22**, 269 (1971).

[58] Balslev, E. and Combes, J. M. *Commun. Math. Phys.* **22**, 280 (1971).

[59] Ho, Y. K. *Phys. Rep.* **99**, 1 (1983).

[60] Cohen-Tannoudji, C., Dupont-Roc, J., and Grynberg, G. *Atom-photon interactions: basic processes and applications*. Ed. John Wiley & Sons, Inc., New York, (1998).

[61] Reed, M. and Simon, B. *Methods of modern mathematical physics VI. Analysis of operators*. Acad. Pr., New York, (1978).

[62] Moiseyev, N. *Phys. Rep.* **302**, 211 (1998).

[63] Buchleitner, A., Grémaud, B., and Delande, D. *J. Phys. B: At. Mol. Opt. Phys.* **27**, 2663 (1994).

[64] Grémaud, B. *Problème Coulombien à trois corps en mécanique quantique,*. PhD thesis, Université Pierre et Marie Curie (Paris 6), (1997).

[65] Buchleitner, A., Delande, D., and Gay, J. *J. Opt. Soc. Am. B* **12**, 505 (1994).

[66] Buchleitner, A. *Atomes de Rydberg en champ micro-onde: régularité et chaos*. PhD thesis, Université Pierre et Marie Curie (Paris 6), (1993).

[67] Delande, D. *Atomes de Rydberg en champ statiques intenses*. PhD thesis, Université Pierre et Marie Curie (Paris 6), (1988).

[68] Delande, D., Bommier, A., and Gay, J. C. *Phys. Rev. Lett.* **66**, 141 (1991).

[69] Grémaud, B. and Delande, D. *Europhys Lett* **40**, 363 (1997).

[70] Krug, A. and Buchleitner, A. *Phys Rev Lett* **86**, 3538 (2001).

[71] Abramowitz, M. and Stegun, I. *Handbook of mathematical functions*. Dover Publications, Inc., New York, (1972).

[72] Karypis, G. and Kumar, V. *J. Parall. Distrib. Comp.* **48**, 96 (1998).

[73] Gilbert, J. R., Moler, C., and Schreiber, R. *SIAM J. Math. Analys. Applic.* **13**, 333 (1992).

[74] George, A. and Liu, J. *SIAM Rev.* **31**, 1 (1989).

[75] Grémaud, B. *private communication*.

[76] Lanczos, C. *J. Res. Nat. Bur. Standards, Sect. B* **45**, 225 (1950).

[77] Parlett, B. N. and Scott, D. S. *Math. Comput.* **33**, 217 (1979).

[78] Ericsson, T. and Ruhe, A. *Math. Comput.* **35**, 1251 (1980).

[79] Krug, A. *Alkali Rydberg states in electromagnetic fields: computational physics meets experiment.* PhD thesis, Ludwig-Maximilians-Universität München, (2001).

[80] Golub, G. H. and Loan, C. F. *Matrix Computations*. The John Hopkins University Press, Baltimore, Maryland, (1996).

[81] *http://www.lrz-muenchen.de/services/compute/hlrb/hardware-en/*.

[82] *http://www.rzg.mpg.de/computing/IBM_P/*.

[83] *http://www.mpi-forum.org/docs/docs.html*.

[84] Snir, M., Otto, S., Huss-Lederman, S., Walker, D. W., and Dongarra, J. J. *MPI: The complete reference*. MIT Press, Cambridge, (1995).

[85] Hempel, R. and Walker, D. W. *Computer Standards and Interfaces* **21**, 51 (1999).

[86] *http://www.lrz-muenchen.de/services/compute/hlrb/compiler/.*

[87] von Neumann, J. and Wigner, E. P. *Phys. Z* **30**, 467 (1929).

[88] Landau, L. D. *Phys. Z Soviet* **2**, 46 (1932).

[89] Zener, C. *Proc. R. Soc. London A* **137**, 696 (1932).

[90] Friedrich, H. and Wintgen, D. *Phys. Rev. A* **32**, 3231 (1985).

[91] Richter, K. *Semiklassik von Zwei-Elektronen-Atomen.* PhD thesis, Albert-Ludwigs-Universität Freiburg, (1991).

[92] Schlagheck, P. *Das Drei-Körper-Coulombproblem unter periodischem Antrieb.* PhD thesis, Technische Universität München, (1999).

[93] Lichtenberg, A. and Lieberman, M. A. *Regular and Chaotic Dynamics.* Springer-Verlag, New York, (1992).

[94] Ostrovsky, V. N. and Prudov, N. V. *J. Phys. B* **28**, 4435 (1995).

[95] Schlagheck, P. and Buchleitner, A. *Physica D* **131**, 110 (1999).

[96] Eichmann, U., Lange, V., and Sandner, W. *Phys. Rev. Lett.* **64**, 274 (1990).

[97] Heber, K. D., Seng, M., Halka, M., Eichmann, U., and Sandner, W. *Phys. Rev. A* **56**, 1255 (1997).

[98] Camus, P., Gallagher, T. F., Lecompte, J. M., Pillet, P., and Pruvost, L. *Phys. Rev. Lett.* **62**, 2365 (1989).

[99] Leopold, J. G. and Percival, I. C. *J. Phys. B* **13**, 1037 (1980).

[100] Mandel, L. and Wolf, E. *Optical coherence and quantum optics.* Cambridge University Press, New York, (1995).

[101] Davies, M. J. and Heller, E. J. *J. Chem. Phys.* **75**, 246 (1981).

[102] Bohigas, O., Tomsovic, S., and Ullmo, D. *Phys. Rev. Lett.* **64**, 1479 (1990).

[103] Lappas, D. G., Sanpera, A., Watson, J. B., Burnett, K., Knight, P. L., Grobe, R., and Eberly, J. H. *J. Phys. B* **29**, L619 (1996).

[104] Lein, M., Gross, E. K. U., and Engel, V. *Phys. Rev. Lett.* **85**, 4707 (2000).

[105] Richter, K. and Wintgen, D. *J Phys B* **23**, L197 (1990).

[106] Assion, A., Naumert, T., Bergt, M., Brixner, T., Kiefer, B., Seyfried, V., Strehleand, M., and Gerber, G. *Science* **282**, 919 (1998).

[107] Weinacht, T. C., Ahn, J., and Bucksbaum, P. H. *Nature* **397**, 233 (1999).

[108] Arbo, D. G., Reinhold, C. O., and Burgdörfer, J. *Phys. Rev. Lett.* **69**, 23409 (2004).

[109] Hanson, L. G. and Lambropoulos, P. *Phys. Rev. Lett.* **77**, 2186 (1996).

[110] Białynicki-Birula, I., Kalinski, M., and Eberly, J. H. *Phys. Rev. Lett.* **73**, 1777 (1994).

[111] Brunello, A. F., Uzer, T., and Farelly, D. *Phys. Rev. Lett.* **76**, 2874 (1996).

[112] Delande, D. and Buchleitner, A. *Adv. At. Mol. Opt. Phys.* **34**, 85 (1994).

[113] Lazutkin, V. F. *Theory and Semiclassical Approximation to Eigenfunctions.* Springer-Verlag, Berlin, (1993).

[114] Raman, C., Weinacht, T. C., and Bucksbaum, P. H. *Phys. Rev. A* **55**, R3995 (1997).

[115] Graham, R. *Comm. At. Mol. Phys.* **25**, 219 (1991).

[116] Morse, P. M. and Feshbach, H. *Methods of theoretical physics, V. I.* Mc Graw Hill, Inc., New York, (1953).

Curriculum Vitae

Last names:	MADROÑERO PABÓN
First names:	GUILLERMO JAVIER
Place of birth:	Pasto, Colombia
Date of birth:	11 December 1972
Marital status:	Married
Profession:	Physicist
Nationality:	Colombian
e-mail:	jma@mpipks-dresden.mpg.de
Address:	Sebnitzer Str. 36, 01099, Dresden, Germany
Home Phone:	(++49+351)+8108462
Institution:	Max Planck Institute for the Physics of Complex Systems
Address:	Nöthnitzer Str. 38, 01187, Dresden, Germany
Phone:	(++49+351)+8711123
Phax:	(++49+351)+8711999

Educational Career:

Aug. 1992 - Dec. 1997	Physics faculty of the "Universidad Nacional de Colombia". *Tesis meritoria* (with distinction). **Degree: Physicist.**
Jan. 1998 - Mar. 2001	Physics Faculty of the "Universidad Nacional de Colombia". *Tesis meritoria* (with distinction). **Degree: Magister in Physics.**
Since June 2001	PhD student at Max Planck Institute for the Physics of Complex Systems, Dresden, Germany.

Recent Workshops:

October 18-23, 2002	"ICOMP IX" - Elounda, Crete, Greece Poster Presentation: *2D helium in electromagnetic fields.*
January 29 - February 2, 2003	"Semiclassics, quantum chaos, and mesoscopics"- Dresden, Germany. Oral presentation: *Planar helium under periodic driving.*
January 26-30, 2004	"Resonances - from Physics to Mathematics and back"- Dresden, Germany. Invited talk: *Driven frozen planet configuration in 2D helium.*

Publications:

D. Campos, C. Spinel and J. Madroñero,
Ionization of one-dimensional alkali atoms by microwave fields.
J. Phys. A **34**, 8101(2001).

J. Madroñero and A. Buchleitner,
Planar helium under electromagnetic driving;
to be published in the proceedings of the "Second Joint HLRB and KONWIHR Result and Reviewing Workshop", Munich, 2-3 March 2004.